



Cite this: *Lab Chip*, 2025, **25**, 1169

## Micro- and milli-fluidic sample environments for *in situ* X-ray analysis in the chemical and materials sciences

Mark A. Levenstein, \* Corinne Chevallard, Florent Malloggi, Fabienne Testard and Olivier Taché

X-ray-based methods are powerful tools for structural and chemical studies of materials and processes, particularly for performing time-resolved measurements. In this critical review, we highlight progress in the development of X-ray compatible microfluidic and millifluidic platforms that enable high temporal and spatial resolution X-ray analysis across the chemical and materials sciences. With a focus on liquid samples and suspensions, we first present the origins of microfluidic sample environments for X-ray analysis by discussing some alternative liquid sample holder and manipulator technologies. The bulk of the review is then dedicated to micro- and milli-fluidic devices designed for use in the three main areas of X-ray analysis: (1) scattering/diffraction, (2) spectroscopy, and (3) imaging. While most research to date has been performed at synchrotron radiation facilities, the recent progress made using commercial and laboratory-based X-ray instruments is then reviewed here for the first time. This final section presents the exciting possibility of performing *in situ* and *operando* X-ray analysis in the 'home' laboratory and transforming microfluidic and millifluidic X-ray analysis into a routine method in physical chemistry and materials research.

Received 30th July 2024,  
Accepted 4th November 2024

DOI: 10.1039/d4lc00637b

rsc.li/loc

Université Paris-Saclay, CEA, CNRS, NIMBE, LIONS, 91191, Gif-sur-Yvette, France.  
E-mail: mark.levenstein@cea.fr



**Mark A. Levenstein**

*ecosystem restoration, Mark joined the Interdisciplinary Laboratory on Supramolecular and Nanometric Organization (LIONS). His current research is focused on developing automated synthesis and characterization platforms for the discovery of sustainable materials with applications in energy, electronics, and construction.*

### 1 Introduction

There remain many fundamental questions in the chemical and materials sciences relating to natural phenomena and industrial processes including the nucleation and growth



**Corinne Chevallard**

*Corinne Chevallard is a research director at CEA (France). She holds a PhD in physics from the University of Nice-Sophia-Antipolis (France). Her early research focused on instabilities in complex systems, whether liquid crystals (PhD) or polymers (postdoc at the Weizmann Institute of Science, Israel). Since joining the CEA, her research has focused on inorganic crystallization, particularly in relation to biomineratization. In order to characterize the transient structures formed prior to crystallization, she is developing microfluidic devices specifically designed for synchrotron-based techniques, which enable *in situ* structural and chemical characterization in liquid media at the nanoscale.*



pathways of materials,<sup>1,2</sup> the function and deactivation of catalysts,<sup>3,4</sup> and the operation and failure modes of batteries.<sup>5–7</sup> X-rays seem ideally suited to provide insight into these areas since they facilitate a suite of structural, chemical, and imaging techniques, offer high spatial and temporal resolution, and have the penetrating ability required to make *in situ* or *operando* observations within thick three-dimensional (3D) samples. These strengths have only increased in recent years due to the widespread availability of third generation synchrotron light sources,<sup>8</sup> the arrival of X-ray free electron lasers (XFELs) and fourth generation synchrotrons,<sup>9,10</sup> and large improvements in commercial X-ray instruments.<sup>11</sup> However, for many types of samples, one bottleneck is introducing the analyte into the X-ray beam in a way that fully exploits these attributes: for example, rapidly and uniformly mixing liquid reagents to initiate a reaction within the short timescales required to make a single measurement.



**Florent Malloggi**

and biology.

*Dr. Florent Malloggi received his PhD from Paris Cité University (formerly Paris VII) in 2006, specializing in the physics of liquids. He now serves as a research director in the Nanoscience and Innovation for Materials, Biomedicine and Energy (NIMBE) department of CEA within Paris-Saclay University. His research interests are focused on instrumental microfluidic development for applications in energy, chemistry*

*Dr. Fabienne Testard is a research director at CEA, working in the LIONS Laboratory of NIMBE. She has expertise in soft-matter, self-assembling systems and nanomaterials with a strong background in synthesis, characterization and the study of the formation mechanisms of nanomaterials (mainly gold and organic self-assembled particles). She is particularly interested by the behavior of nanomaterials in complex systems and *in situ* SAXS and SANS approaches (with extensive experience at synchrotrons and neutron sources).*



**Fabienne Testard**

*SAXS and SANS approaches (with extensive experience at synchrotrons and neutron sources).*

Microfluidic devices have been proposed as one solution to this sample preparation and manipulation problem. In an excellent earlier review in this journal, Ghazal *et al.* covered the benefit of microfluidics for X-ray analysis in the life sciences and soft matter research.<sup>12</sup> Their review was primarily focused on the ways microfluidic devices could be used to produce and manipulate large numbers of samples and make better use of experimental time at synchrotron facilities. They also highlighted the ways that microfluidic devices could be utilized to perform time-resolved measurements of processes not accessible by conventional macroscale methods. Here, we seek to build upon their work by covering applications in physical chemistry and materials science and focusing primarily on the role of microfluidic devices as “sample environments”. We define these as specialized devices and reactors that enable *in situ* or *operando* measurements of samples and processes in their native states or under non-equilibrium conditions. For the purposes of this review, *in situ* means that a measurement is performed where the reaction or process takes place without moving the sample into a second holder or vessel, and *operando* means that a measurement is performed both *in situ* and while the reaction or process is occurring. By this definition, all *operando* measurements are *in situ*, but not all *in situ* measurements are *operando*. This is not necessarily the same definition as used in catalysis literature.<sup>13</sup> The opposite would then be *ex situ* or post-mortem analysis, where a sample must be moved out of its native environment and prepared for measurement, often requiring quenching, washing, and drying steps, among others.<sup>14</sup>

A growing interest across the chemical, physical, and natural sciences is the study of processes in real-time. For processes that are difficult to observe in nature (e.g., high-pressure phenomena in the Earth's interior) or in industrial environments (e.g., within large chemical reactors), these conditions need to be re-created in the laboratory.



**Olivier Taché**

*measurements.*

*Olivier Taché is a researcher at CEA/NIMBE/LIONS and an expert on the characterization and metrology of nanomaterials. His work includes the development of advanced SAXS methodologies and software to enhance the precision and reliability of nanoparticle size and concentration measurements. He is actively involved in various collaborative projects aimed at enhancing nanosafety and the traceability of nanomaterial*



Microfluidic and other miniaturized devices present a promising way to achieve these goals owing to their ability to control heat and mass transport phenomena quickly and precisely and due to their increased safety over macroscale methods when working under extreme temperatures, pressures, and chemical conditions. Here, our analysis is not restricted to microfluidic devices with channel dimensions  $\ll 1$  mm, because as many have correctly highlighted,<sup>12,15</sup> a longer X-ray beam pathlength through samples results in an optimized signal-to-noise ratio ( $\approx 1$  mm with aqueous solutions and Cu K $\alpha$  radiation). Therefore, for some applications, millifluidic sample environments may even be preferred over their microfluidic counterparts.

Despite a handful of earlier papers, such as on the microfluidic preparation of crystals for subsequent off-chip X-ray diffraction,<sup>16,17</sup> it may have been Greaves and Manz (2005) who first recognized the potential of microfluidic devices for on-chip chemical X-ray analysis.<sup>18</sup> They highlighted, in particular, the power of X-ray fluorescence and X-ray diffraction for elemental analysis and particle identification in flow, respectively, and anticipated that performing real-time measurements on-chip could reduce the time required to optimize crystallization and synthesis conditions. While they did investigate on-chip X-ray generation to make a true “lab-on-a-chip”, they also realized that microfluidic devices could serve as powerful complements to full-scale laboratory equipment, and this is precisely the direction in which the field of microfluidic X-ray analysis has gone over the past 20 years. In fact, in this context, microfluidic devices have been coupled to some of the largest scientific instruments in existence: synchrotron particle accelerators and free-electron lasers. This striking combination of the very big and the very small, already inherent in such facilities, offers the possibility of combining the precise manipulation of subatomic particles with that of molecules and nano- and micro-objects in flow. In addition to this, the control of flow can also solve practical problems like mitigating radiation-induced sample damage and heating, which is becoming more and more important as X-ray sources grow stronger.<sup>19</sup>

Our goal with this review is to provide as comprehensive of an account as possible into the use of micro- and millifluidic sample environments for *in situ* X-ray analysis in the physical and chemical sciences. Therefore, we will cover applications across the three main types of X-ray techniques: scattering/diffraction (section 3), spectroscopy (section 4), and imaging/tomography (section 5). There are many commonalities in the design considerations and technical challenges of sample environments for these different techniques, and we believe that the communities around each technique could benefit from the sharing of knowledge. Preceding this central part of the review, we will also provide some background on predecessor and alternative sample environments for *in situ* X-ray studies in liquids and a brief discussion of some important parameters to consider in relation to microfluidic sample environments (section 2).

As already mentioned, due to the need for fast measurements of dynamic and often dilute samples, microfluidic X-ray experiments are typically performed at synchrotron light sources and sometimes XFELs. These facilities are operated on a competitive, proposal-based, user access model where individual beamlines or end-stations dedicated to scattering, spectroscopy, imaging, or a combination of techniques must be solicited for experimental time. Further, these facilities are seldom located near a researcher's home institution. Therefore, experimental “beamtime” is not guaranteed, not limitless, and often not easy in terms of the transport and set-up of complex equipment. Near the end of the review, we will thus cover progress in utilizing micro- and milli-fluidic sample environments with laboratory X-ray instruments (section 6), where techniques such as X-ray diffraction (XRD), X-ray fluorescence (XRF), and micro-computed tomography ( $\mu$ CT) are already readily available at most universities and research institutes. The increasing feasibility of laboratory-based analysis should facilitate much easier and more practical *in situ* X-ray experiments. It should also allow many more researchers to benefit from fluidic X-ray sample environments in their own research, when the high brilliance or coherence provided by large-scale X-ray facilities is not strictly required. Finally, we will present our perspective on the current state of the field and some practical tips regarding device fabrication and best practices (section 7). This will conclude with a look towards the future focused on promising trends and developments that we think will guide the field over the coming years.

This review will be limited to micro- and milli-fluidic X-ray sample environments where measurements are performed *in situ*, on-chip, and on inorganic and/or hard condensed matter samples. Articles pertaining to only biological or soft condensed matter samples, such as those already reviewed by Ghazal *et al.*,<sup>12</sup> will be referenced only where they have made an important technical contribution later implemented for physical chemistry or materials research. An exception will be made in section 6 on laboratory-based analysis, where studies of all sample types will be covered, since these have not been reviewed previously. Similarly, articles where analysis is performed on a droplet, jet, or spray exiting a microfluidic device will also be excluded, although some will be introduced briefly in the background section. Such jet-based devices have been covered previously in the context of serial crystallography, and the reader is directed to these reviews for further information.<sup>20–22</sup> To the best of our ability, this review is comprehensive up through the year 2023 unless otherwise noted.

## 2 Background

This background section is not intended to be exhaustive, rather its goal is to provide some general context for the review. It will focus on two important pre-microfluidic technologies and two important microfluidics-parallel



technologies, all of which remain in use today and have weaknesses—and also some strengths—compared to microfluidics. This will provide the reader with the setting in which micro- and milli-fluidic sample environments operate and a general knowledge of the types of liquid sample manipulation tools currently available at large-scale X-ray facilities. We will finally present some design considerations and definitions for describing micro- and milli-fluidic flow reactors and their utility for *in situ* X-ray analysis, which will aid in evaluating and comparing the devices presented in the following review.

## 2.1 Precursors to microfluidic devices

**2.1.1 Stopped-flow devices.** Perhaps the most common device for performing *operando* studies of chemical and biochemical reactions and precipitation processes is the stopped-flow device. It is popular not only for X-ray analysis, but also for neutron scattering,<sup>23</sup> FTIR spectroscopy,<sup>24</sup> and a

range of UV-vis based spectrophotometric and fluorimetric methods,<sup>25</sup> to name a few. In a basic stopped-flow configuration, two reactant solutions contained in separate syringes are quickly combined in a turbulent mixing unit and introduced into a thin capillary for observation as a function of reaction time (Fig. 1a).<sup>26</sup> The observation should coincide with the rapid stoppage of the flow by, for example, the closure of an electromechanical valve (“hard-stop”) to prevent back-flow into the capillary and to ensure reproducibility in the analysis of reaction kinetics. This method has been widely adopted at synchrotron sources for different techniques (e.g., SAXS, XRD, XAS) to study processes including micellar transformations,<sup>27</sup> catalysis,<sup>28</sup> the nucleation and growth of nanoparticles,<sup>29,30</sup> the early stages of mineral formation,<sup>31–33</sup> and the crystallization of metal-organic frameworks (MOFs)<sup>34,35</sup> and biochemicals.<sup>36</sup>

The popularity and longevity of the stopped-flow method likely stem from its accessible operation yet powerful performance. Originally developed in the 1940s, stopped-flow

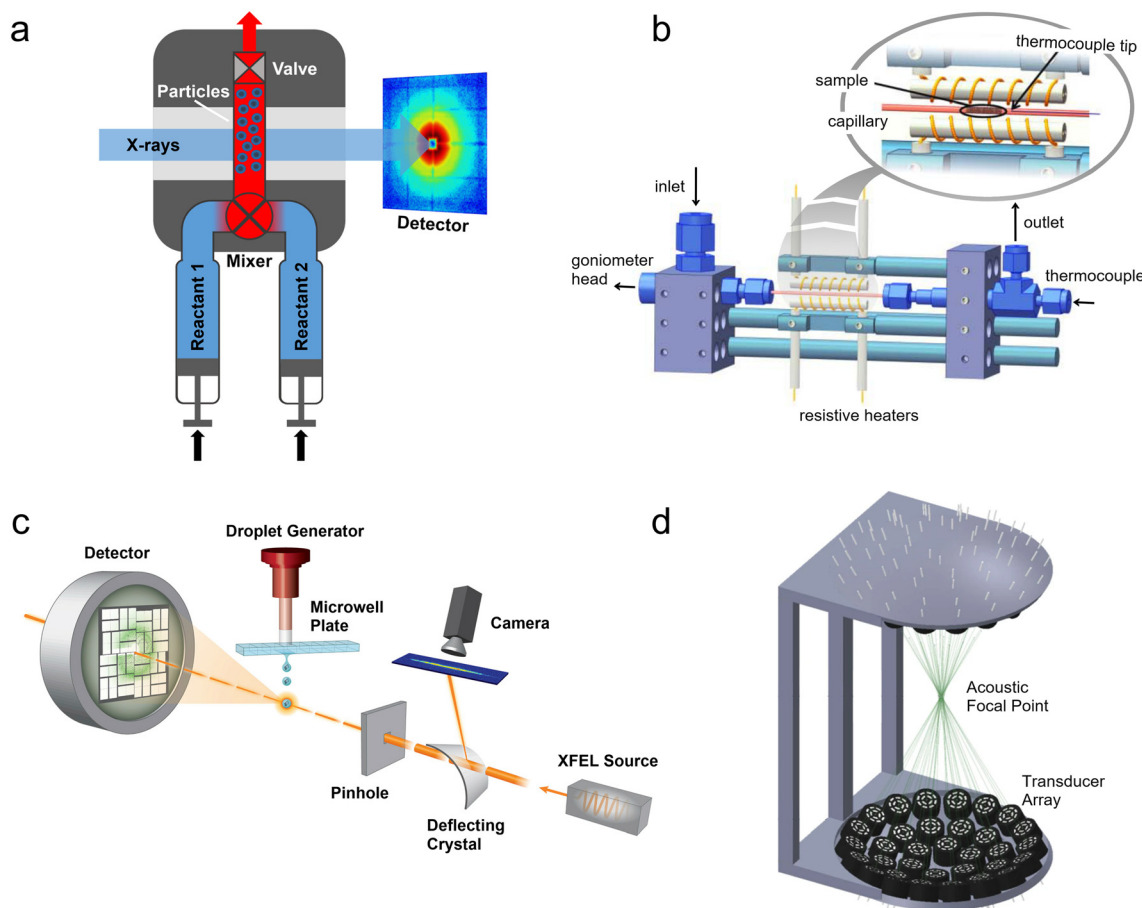


**Fig. 1** Predecessors and alternatives to micro- and milli-fluidic devices for X-ray analysis. (a) Illustration of a stopped-flow device mounted at an X-ray scattering facility. Two reactants are injected through a mixing element into a capillary where the flow is stopped by a fast valve (adapted with permission from Virtanen *et al.*, 2019; Copyright 2019 American Chemical Society).<sup>26</sup> (b) Design of a capillary gas cell with flow and heating capabilities. The inset shows a detailed view of the capillary where the powder sample is placed (adapted with permission from Chupas *et al.*, 2008; International Union of Crystallography).<sup>37</sup> (c) A droplet injector for use with XFELs. Each droplet is hit by a single femtosecond X-ray laser pulse (adapted from Roessler *et al.*, 2016; with permission from Elsevier).<sup>38</sup> (d) Design of a droplet levitator comprising acoustic transducer arrays to position a liquid sample at a focal point within an X-ray beam (adapted with permission from Morris *et al.*, 2019; CC BY).<sup>39</sup>



devices required a much smaller volume of solution than their large continuous flow predecessors.<sup>25,40</sup> Utilizing passive turbulent mixers, such as the Ball-Berger design,<sup>41</sup> stopped-flow devices can also achieve mixing times in the 1 ms to 0.01 ms range (with dead times before observation from ~10 ms down to 0.1 ms).<sup>42</sup> From a practical standpoint, many off-the-shelf commercial devices exist, which are often available at synchrotron beamlines and already integrated with beamline hardware and acquisition software. While they are not always simple to use, they may be easier to work with than many home-made devices.

Despite these numerous strengths, stopped-flow devices have some weaknesses that are especially pronounced in the case of X-ray analysis. One is that the time-resolution of the measurements is limited by the duration of X-ray exposure required to achieve a good signal-to-noise ratio. Taking X-ray scattering as an example, the small number of photons elastically scattered compared to the number of photons in the incident beam often requires the use of high-brilliance synchrotron radiation. However, even at many current beamlines, it is difficult to obtain a good quality small angle X-ray scattering (SAXS) pattern from exposures much shorter than 0.02–1 s (*i.e.*, frame rates of 1–50 Hz) depending on the sample contrast. This is especially true at early reaction times of less than a few seconds, when weakly scattering and/or dilute reaction intermediates—requiring even longer exposures to be detected—are present. Moreover, longer exposure times are also required for performing wide-angle X-ray scattering (WAXS).

One solution to this first weakness of stopped-flow devices is to average the results of several experiments. However, combining individual time-resolved frames from different experiments requires very high reproducibility in the mixing conditions, the cleaning procedure, and the timing between the data acquisition workflow and the operation of the device. This is not always the case due to, for example, the formation of bubbles during mixing and inconsistencies in the mixing ratio.<sup>43</sup> Another solution, such as increasing the photon flux, only highlights another weakness of stopped-flow devices. This is that the sample is retained in the capillary and continually exposed to high energy ionizing radiation. Depending on the sensitivity of the sample, it is possible that radiation-induced heating or beam damage could alter the process under study and introduce significant uncertainty into data interpretation. Indeed, this problem can even affect inorganic materials,<sup>44,45</sup> and it has only increased at fourth generation synchrotrons.<sup>19</sup>

**2.1.2 Capillary gas (Norby) cells.** The second precursor sample environment that we will discuss is the capillary gas cell, also known as the Norby cell. Named after its inventor P. Norby, the original Norby cell is a simple device comprising a glass capillary and a modified T-piece tube fitting (*e.g.*, Swagelok) designed for studying hydrothermal and gas–solid reactions by XRD.<sup>46</sup> One end of the metal T-piece is connected to the capillary, and the other two ends are reserved for a connection to a pressurized gas line and for

mounting onto a standard goniometer head, respectively. In this way, a sample inside the capillary (typically a powder) can be placed under pressure and easily manipulated within a diffractometer. The capillary can also be externally heated using a hot air blower<sup>46</sup> or cooled using a cryogenic gas flow.<sup>47</sup> More complex versions of the device that permit continuous gas flows over the powder and that integrate heating elements are now routinely used at X-ray powder diffraction, X-ray absorption spectroscopy, and high energy synchrotron beamlines (Fig. 1b),<sup>37</sup> where they are also sometimes known as Clausen cells.<sup>48</sup>

Capillary gas cells are powerful sample environments that enable a range of *in situ* and *operando* studies under extreme conditions. These include investigations of hydrothermal synthesis,<sup>49,50</sup> catalysis,<sup>48,51</sup> gas capture and storage,<sup>52</sup> solid phase transformations,<sup>53</sup> and other gas–solid interactions.<sup>54</sup> As already stated, their simplicity, ubiquity, and utilization of commercial components make them attractive to many researchers, however, they do have some weaknesses. They are primarily designed to interact with a pre-loaded powder, slurry, or sample bed that is fixed in place. Outside of a few exceptions, *in situ* generation of the sample (*e.g.*, synthesis from solution) or subsequent manipulation or interaction (*e.g.*, fluid injection) with the sample is not supported. There are versions of the capillary cell that enable high pressure liquid flows, but these are essentially large millifluidic systems<sup>55,56</sup>—although they will not be treated further here. Even considering these exceptions, reaction products are still not recycled under the beam, presenting the same potential for radiation damage as stopped-flow devices. Additionally, the high temperature and pressure of the gas cells and the fragility of the glass capillaries present a safety risk that must be considered during the experiment.<sup>52,55</sup>

## 2.2 Parallel technologies

**2.2.1 Liquid sample injectors.** The need for high-throughput sample introduction for macromolecular serial crystallography (SX), X-ray photon correlation spectroscopy (XPCS) and other coherent scattering, spectroscopy, and imaging techniques at XFELs has led to the development of a range of liquid sample injectors over the past two decades (Fig. 1c). Although these devices are often considered “microfluidic”, for the purpose of this review, they will be treated separately since analysis is performed off-chip in a free jet or droplet. The high fluence of an XFEL pulse would damage the window of a microfluidic device, rendering it inoperable or degrading the signal quality. Conversely, there are indeed microfluidic devices designed for “fixed-target” serial synchrotron crystallography (SSX), where analysis is performed on-chip. However, these are generally restricted for use in structural biology and are, therefore, out of the scope of this review. Interested readers can find information about devices for fixed-target serial crystallography from other sources.<sup>12,21</sup>



Injector-based serial femtosecond crystallography (SFX) was first demonstrated by Chapman *et al.*<sup>57</sup> using a gas dynamic virtual nozzle (GDVN),<sup>58</sup> which can be tuned to produce jets or monodisperse droplets with the use of a piezoelectric actuator. A very fast ( $\sim 10\text{--}100\text{ m s}^{-1}$ ) and thin ( $\sim 1\text{--}25\text{ }\mu\text{m}$  diameter) fluid jet is created by a high flow rate of sample (typically protein crystals in their mother liquor) surrounded by a sheath flow of a low density gas (*e.g.*, He) in order to rapidly replenish the sample stream after each X-ray pulse (up to MHz frequency).<sup>59</sup> However, for rare or expensive samples the amount of liquid consumed to maintain this jet is too high, and utilizing crystals grown and injected in viscous lipidic cubic phases (LCPs) was later shown to enable jet formation at lower flow rates, reducing sample consumption by a factor of 20.<sup>60</sup> Other groups have developed drop-on-demand systems, such as acoustic injectors that can dose nanoliter to picoliter droplets directly from a microwell plate (Fig. 1c).<sup>38</sup> While many of the uses of these XFEL injector systems have focused on structural biology, they have also facilitated fundamental physics and chemistry experiments including investigating the ionization<sup>61</sup> and supercooling of water,<sup>62</sup> ice nucleation,<sup>63</sup> the structure of semiconducting microcrystals,<sup>64</sup> and the diffusion dynamics of nanoparticles.<sup>65</sup>

In addition to studying static pre-grown crystals and pure liquids, experimental methods have been developed for *operando* studies of dynamic reactions and processes. The first is the well-known “pump-probe” method, in which a sample is hit mid-flight with an optical laser pulse and subsequently probed by an X-ray laser pulse after a carefully timed delay.<sup>66,67</sup> Of greater interest here, is the so-called “mix-and-inject” method, in which liquid reactants are rapidly mixed and introduced into the XFEL beam.<sup>68</sup> The delay time between the mixing point and the point of interaction with the beam determines the time point of the reaction that is probed.<sup>69</sup> This technique has primarily been performed at XFEL sources to study the conformational changes of proteins and nucleic acids upon ligand binding.<sup>70–72</sup> However, it has also been demonstrated at synchrotron sources,<sup>73</sup> where storage ring upgrades<sup>74</sup> and the possibility of using high-flux, polychromatic, ‘pink’ beams<sup>75</sup> make these experiments more and more feasible.

Injector-based serial crystallography, which has been performed largely at XFELs, and microfluidic X-ray scattering (discussed in section 3), which has been performed primarily at synchrotrons, developed quite independently. However, in recent years there has been more overlap between the two communities as serial crystallography has been increasingly performed at synchrotrons – sometimes even at the same beamlines as on-chip microfluidics experiments.<sup>76,77</sup> This seems natural considering the two fields use much of the same equipment, face many of the same technical challenges, and have similar goals, albeit often studying different sample types. A strength of both techniques is that samples are constantly replenished in the beam to minimize the effects of radiation damage on data collection. This is

especially true of SFX at XFELs, where femtosecond data collection physically outruns degradation processes (so-called ‘diffraction before destruction’).<sup>57</sup> An additional advantage of injector-based techniques compared to on-chip microfluidic analysis is that no device materials are in the beam path to attenuate the signal or produce background noise. Yet, while both types of experiments are complex, currently injector-based XFEL experiments are difficult and require a team of scientists and engineers to perform. Likewise, the requirements for device fabrication and interfacing with XFEL hardware are much stricter than with synchrotron-based microfluidics experiments. Finally, owing to the experimental design and geometry, only a single time-point can be collected per injector-based XFEL experiment. This requires several separate experiments to probe different intermediate states in a reaction, which takes a great deal of time and requires high reproducibility.

**2.2.2 Droplet levitators.** A less common, but still very useful liquid sample environment is the acoustic droplet levitator (Fig. 1d). Using either a piezoelectric sonotrode (*i.e.*, a Langevin horn)<sup>78</sup> or arrays of ultrasonic transducers,<sup>39</sup> these devices create standing acoustic waves containing pressure nodes where a liquid droplet of  $\sim 5\text{ nL}$  to  $5\text{ }\mu\text{L}$  ( $\sim 0.2$  to  $2\text{ mm}$  diameter) can be levitated.<sup>78</sup> In contrast to most other sample introduction techniques, the free-floating droplet is not in contact with any liquid or solid surface, making droplet levitation a powerful technique for the study of bulk phenomena away from surfaces, such as homogenous nucleation.<sup>78</sup> This also means that there are no reactor walls or windows for the X-ray beam to pass through, reducing the background noise. The acoustic trapping also imparts some motion to the droplet, which helps to rotate crystals for single-crystal X-ray diffraction (SCXRD) experiments<sup>39</sup> and to circulate fluid to avoid radiation damage.<sup>79</sup> Compared to most flow-based devices like droplet injectors—and even microfluidic devices—total sample consumption is very low, requiring just a few drops to be deposited with a microliter syringe.<sup>80</sup>

Despite the many strengths of droplet levitators, there are also some drawbacks, particularly related to performing *in situ* experiments. After the initial deposition of the sample, controlled mixing and/or subsequent operations on the droplet(s) are difficult. Sample evaporation is also a major problem, unless evaporation is used to initiate the process under study<sup>78</sup> or to map a parameter space.<sup>79</sup> Evaporation of the solvent concentrates reactants in the droplets, introducing an additional uncontrolled variable into *in situ* chemistry experiments. There are ways to avoid or minimize sample evaporation, but these each have tradeoffs that compromise other advantages of droplet levitators. For example, aqueous droplets can be covered in an immiscible oil layer that inhibits water transport,<sup>39</sup> however this introduces a liquid–liquid interface. Alternatively, large droplets in which evaporative losses are negligible to the total volume can be utilized, but these will be difficult to uniformly mix and may have large inhomogeneities in



composition and temperature. Finally, droplets can be levitated in an environment with controlled temperature and humidity to prevent evaporation,<sup>80,81</sup> but this normally requires a sample chamber with walls through which the X-ray beam must pass. Therefore, in many cases, droplet levitation may be better for the introduction and manipulation of static samples rather than as an *operando* X-ray sample environment.

### 2.3 Micro- and milli-fluidic X-ray sample environments

**2.3.1 Advantages.** Microfluidic devices and their millifluidic counterparts offer varying advantages compared to the other liquid manipulation approaches discussed above. The general strengths of microfluidic devices have been well documented;<sup>82–84</sup> these include low sample volume utilization, minimal risk and severity of sample leakage, precise control of mixing and diffusion, and a high surface area-to-volume ratio that leads to efficient heat transfer, faster reaction kinetics, and other beneficial properties. Micro- and milli-fluidic devices also have several specific advantages as sample environments for *in situ* X-ray analysis, especially continuous flow devices. The first is simply their small footprint, which makes them easier to mount in a beamline experimental hutch or to fit within a laboratory X-ray instrument that has considerable space restrictions. The second advantage is the rapid replenishment of the sample in the X-ray beam by the flow, which minimizes radiation damage and heating.<sup>85</sup> This is a particular advantage micro- and milli-fluidic devices have over stopped-flow devices, Norby cells, and droplet levitators, in which a static sample is held within the beam (*N.B.*, there are also fluidic sample environments with fixed sample materials, but there is usually still a flow that facilitates sample cooling). The third advantage is their small channel size, which allows high transmission of the beam. Except for very “hard” X-rays (>20 keV) used for X-ray radiography and tomography, beam path lengths of more than a few millimeters through liquids result in significant attenuation. Moreover, for “soft” X-rays (<2 keV) frequently used for spectroscopy and spectromicroscopy, it is difficult to measure samples of more than a few microns in thickness. Conversely, as stated earlier, depending on the energy of the incident X-rays, the thicker channel of a millifluidic device may optimize the produced signal relative to the amount of attenuation, at least in the case of X-ray scattering in a transmission geometry. Finally, the fourth advantage is the position-to-time conversion made possible along a flow channel.<sup>86</sup> As will be discussed in greater detail below, this conversion enables the collection of data with high time resolution independent of instrumental hardware limitations.

**2.3.2 Device material considerations.** One of the first and most important considerations in designing a micro- or milli-fluidic device for X-ray analysis is selecting the device material(s). The previous review of Ghazal *et al.* covered these aspects well—and we encourage the reader to go there for

more information<sup>12</sup>—but we will provide a brief overview here. As a general rule, any device material in the beam path should be as thin as possible and made from light elements. This minimizes the attenuation of the beam as well as whatever contribution the material might have to the overall X-ray signal, whether absorption, scattering, or fluorescence. Due to fabrication, chemical, thermal, and other practical constraints, this is not always possible. Thus, care must be taken to find a material that at least does not overly absorb, scatter, or fluoresce in a region of interest for your sample (*N.B.*, at very hard X-ray energies, these restrictions are often relaxed). When a desired device material is not ideal for the X-ray technique of choice, it is also possible to design so called “windows” in your device made from a material with suitable X-ray characteristics. However, the integration of windows can present its own design challenges and provide additional locations for device failure (*e.g.*, leakage, fracture, or hydrodynamic instabilities/eddies).

Many different device materials and fabrication approaches have been reported, as will be seen in the following review sections. Here, we will only introduce some of the most common families of device materials. The first are silicon and glass-based devices. These traditional microfluidic materials have the advantage of being highly chemically and thermally stable, and they can be patterned with high resolution features. However, they usually require expensive cleanroom fabrication methods and can present issues with high X-ray absorption and scattering—especially glass—unless using a very thin device or very hard X-rays.<sup>85</sup> Silicon nitride ( $Si_xN_y$ ) is also commonly used as a window material since  $Si$  chips containing ultrathin low-absorption  $Si_xN_y$  membranes ( $\leq 1 \mu m$ ) can be readily purchased.<sup>87,88</sup> However, these membranes are fragile, can bow/bend under fluid or vacuum pressure,<sup>89</sup> and can be expensive if non-standard or low tolerance membrane sizes are required. Conversely, simple millifluidic devices often utilize a thin-walled glass capillary ( $\sim 10$ – $100 \mu m$ ) as the main analysis section. This is a cheap option with a very good signal-to-noise ratio owing to the relative thinness of the capillary wall with respect to its inner diameter.

The second group are curable polymers, such as polydimethylsiloxane (PDMS). While cheaper and easier to fabricate than microfluidic silicon/glass options, PDMS has a significant X-ray absorption and scattering profile,<sup>90</sup> and many groups have demonstrated alternatives with better performance including Norland Optical Adhesive (NOA81)<sup>91</sup> and off-stoichiometry thiol-ene (OSTE).<sup>92</sup> Thirdly, another common option is using a commercial polymer film, the most popular of which is the polyimide, Kapton®. This polymer can be bought cheaply in thin sheets ( $\sim 25$ – $100 \mu m$ ), and it has excellent thermal and mechanical stability, moderate chemical resistance, and excellent resistance to X-ray radiation.<sup>93</sup> It is a very good all-around material for microfluidic X-ray analysis; however, it does present some X-ray scattering features at small angles, which can introduce noise in SAXS data.<sup>92</sup>



Fourthly, high pressure/temperature flow cells are often made from metals or metal alloys due to their high thermal stability and mechanical strength. These are usually integrated with windows made from  $\text{Si}_x\text{N}_y$  or diamond for use at lower X-ray energies but may be used without windows for hard X-ray tomography. Finally, some newer device materials, *e.g.*, graphene<sup>94</sup> and monocrystalline quartz,<sup>95</sup> have been utilized for microfluidic fixed-target serial crystallography, and may find use for X-ray devices in the physical sciences. The X-ray absorption, transmission, and scattering properties of common device materials are found in many of the papers cited above and throughout the review and are widely available in previous microfluidic X-ray literature. Additionally, several helpful online calculators exist for estimating these parameters, such as from the Advanced Photon Source (<https://11bm.xray.aps.anl.gov/absorb/absorb.php>), Lawrence Berkeley National Laboratory ([https://henke.lbl.gov/optical\\_constants/atten2.html](https://henke.lbl.gov/optical_constants/atten2.html)), and the National Institute for Standards & Technology (<https://physics.nist.gov/PhysRefData/FFast/html/form.html>). The material information for all papers reviewed below can be found in Tables 1–4.

**2.3.3 Important temporal definitions.** While the numerous micro- and milli-fluidic devices intended for X-ray scattering, spectroscopy, and imaging applications have a variety of different design considerations and fabrication methods, there are many attributes and important parameters common to all platforms. Crucially, any sample environment should be well characterized to determine the conditions experienced by the sample and to enable accurate comparison with other experiments. A full treatment of the physical parameters and descriptors of microfluidic devices is outside the scope of this review, and the reader is directed to other sources for further information.<sup>82,83,96,97</sup> Here, as this review is focused on the utility of microfluidic devices as sample environments for *in situ* and *operando* analysis, we will concentrate primarily on device operational parameters related to time.

One of the most important parameters to determine for a sample environment is the experimental or reaction time ( $t$ ) associated with each measurement. This entails having high control over and low uncertainty in assigning  $t = 0$  and understanding how the reaction or process develops in space across the device, *e.g.*, by fluid flow or heating. Microfluidic devices are advantageous in this context, because as mentioned above, for a flow device operated under steady-state conditions, the position along a flow channel can be converted into an effective time. However, even for microfluidic devices, the task is not so straightforward, and there are several parameters and other characteristic times that must be considered before the true reaction time and time resolution of an experiment can be determined. Further, there are varying definitions for these terms in use throughout the literature. We seek to provide some clarity and standardization to these terms below.

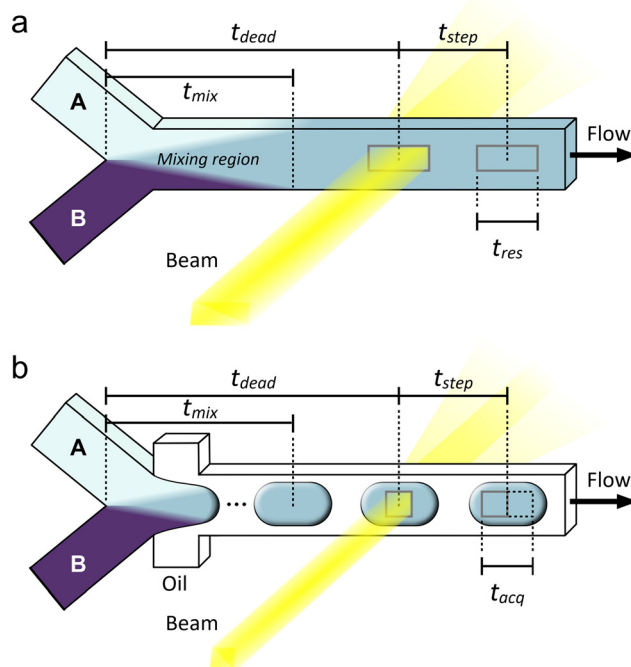


**Fig. 2** Examples of (a) continuous and (b) droplet microfluidic flow reactors illustrating some important definitions of time related to sample environments for *operando* X-ray analysis. Reactants A and B are mixed at a Y-junction. Based on a given steady flow rate, the characteristic lengths shown correspond to characteristic times,  $t$ . A simple diffusive mixer is shown in (a), but various other designs could be used in the mixing region to accelerate the mixing process, *i.e.*, by exploiting inertial effects for chaotic mixing.<sup>98</sup> Mixing lengths are not to scale.

For this discussion, we will use the example of the micro/millifluidic flow reactor, as it is a common sample environment used for a range of techniques and applications (Fig. 2). The most fundamental time parameter to consider for such a device is the mixing time ( $t_{\text{mix}}$ ) between the molecules or reagents that initiate the reaction. This time is critical because if reactants begin mixing at  $t = 0$ , but for example, it takes five seconds for them to mix, then any measurement made before 5 s of reaction time will contain some unreacted species and any measurement made afterwards will contain a mixture of reaction times: those starting closer to  $t = 0$  and those starting closer to  $t = 5$  s. Here, we define  $t_{\text{mix}}$  as the time it takes to fully mix reactants, *i.e.*, the time required from the initial contact of reactants to achieve uniform composition across the flow (Fig. 2a). Others may utilize a specific mixing index for defining  $t_{\text{mix}}$ , for example, 90% mixed.<sup>98</sup> Clearly, many reactions may begin before full mixing is achieved,<sup>69</sup> thus experiments should ideally have  $t_{\text{mix}} \ll$  reaction time to decouple the mixing and the reaction. Failing this, the mixing should be at least faster than the reaction kinetics of interest to minimize uncertainty and prevent some kinetics from being masked. Although this is less important for thermally- or photo-induced reactions,



for example, where species can be mixed slowly before the reaction is initiated further downstream.

Mixing times are generally determined through numerical simulations and/or flow experiments using a colorimetric or fluorimetric tracer in the place of chemical reactants.<sup>99</sup> Due to small measurement uncertainties or uncertainties in the diffusion coefficients of reactant molecules, often the mixing time is reported as a conservative upper limit or even presented simply as the observation dead time ( $t_{\text{dead}}$ , Fig. 2a). This term is inherited from the stopped-flow community and simply means the time between the initiation of a reaction ( $t = 0$ ) and the first possible measurement time. This distinction between  $t_{\text{mix}}$  and  $t_{\text{dead}}$  stems from the physical separation between the mixing element and the analysis capillary. Depending on the design of a microfluidic device, it may also not be possible to observe the flow right at the point of full mixing, or conversely, a time point after  $t_{\text{mix}}$  may be targeted intentionally to allow for a factor of safety in the mixing time.

The next important time parameter is the time resolution ( $t_{\text{res}}$ , Fig. 2a). This term is also defined in different ways in the literature, where it is sometimes taken to be equivalent to the mixing time,  $t_{\text{mix}}$ . The logic for this definition is that it would be impossible to achieve higher time resolution than the distribution of fluid age resulting from mixing. To some extent this is accurate, however, if mixing is fast, often the limiting factor to resolution is the time it takes for fluid to pass through the beam, *i.e.*, the age distribution of fluid within the beam neglecting mixing time. This is determined by the beam size in the direction of the flow and the fluid velocity, and it is one of several reasons why microfocused X-ray beams are typically utilized for microfluidics experiments. Improving temporal resolution can be a real advantage for the analysis of rapid kinetics, which are not able to be followed with the achievable acquisition times of most current X-ray instrumentation alone. For example, in the case of a microfocused beam (typically  $\sim 20 \mu\text{m}$  in size) and an average linear velocity of  $0.1 \text{ m s}^{-1}$  (corresponding to a flow rate of  $1 \mu\text{L s}^{-1}$  in a channel with a cross-section of  $100 \mu\text{m} \times 100 \mu\text{m}$ ), one can obtain a temporal resolution of around  $0.2 \text{ ms}$ —much shorter than usual acquisition times.

Related to  $t_{\text{res}}$  is the average time interval between each measurement position, or the time step ( $t_{\text{step}}$ , Fig. 2a). Depending on the device design and operation and the position of the X-ray windows, the distance between each measurement position can vary, with the smallest  $t_{\text{step}}$  without overlap being the effective length of the beam along the flow channel. This is often considered to be the full-width at half maximum (FWHM) of the beam intensity. If measurement positions are only a beam length apart, then  $t_{\text{step}}$  is equal to  $t_{\text{res}}$ . Such an arrangement provides the highest possible resolution of the reaction taking place along the flow channel, but depending on the reaction kinetics, having many positions so close together may not be useful

and will add unnecessary time and complication to an experiment. Importantly, like for  $t_{\text{res}}$ ,  $t_{\text{step}}$  is related to only the beam size and the fluid velocity with respect to the beam and is completely independent of the X-ray exposure time and detector frame rate unlike for stopped-flow experiments. There is some uncertainty in the time step arising from the precision of the sample stage motors and Taylor dispersion, *i.e.*, the fact that fluid at the center of the channel will travel faster than fluid near the walls,<sup>100</sup> although these effects are not often explicitly considered in *operando* X-ray experiments.

Alternatively, it is possible to eliminate Taylor dispersion by using a segmented flow of droplets in an immiscible continuous phase, where liquid and solids contained within a droplet stay together along a channel, forming an independent microreactor (Fig. 2b).<sup>100</sup> In this case,  $t_{\text{res}}$  is not defined by the beam size, but rather by the spread of reaction times in the fluid composing a droplet (*i.e.*,  $t_{\text{mix}}$ ), assuming all droplets to be uniformly and continuously mixed. However, when utilizing droplets, an additional sampling consideration must be made to ensure that the signal of interest from the droplets is not masked by noise from the continuous phase.<sup>101</sup> In droplet microfluidics, high density fluorinated oils are often utilized in this role, and these scatter significant numbers of photons. Thus, to minimize or eliminate noise from the continuous phase, the data acquisition strategy must adopt a droplet size, droplet velocity, beam size, and frame rate combination such that the effective acquisition length (or acquisition time,  $t_{\text{acq}}$ ) is contained within a single droplet (Fig. 2b).<sup>92</sup> This consideration is analogous to the Nyquist rate in analog-to-digital signal conversion.<sup>102</sup> For this reason, it is even more important to use a microfocused X-ray beam when performing an experiment with a droplet microfluidic device. Taylor dispersion can also be minimized using hydrodynamic flow focusing to concentrate reactants into a narrow fluid jet. However, this is only effective at short reaction times when diffusion can be neglected<sup>103</sup> and also requires a microfocused X-ray beam to isolate data from the concentrated jet.

Now that we have learned about some alternatives to micro- and milli-fluidics and briefly discussed some characteristics and definitions for fluidic sample environments, the following three sections will cover the use of these devices in X-ray scattering & diffraction, spectroscopy, and imaging, respectively. The goal of these sections is to present as comprehensive of a view as possible into the work done in these areas in order to serve as a reference and to present the varied ways researchers have addressed the challenges of performing *in situ* X-ray measurements. These sections will also contain a greater focus on applications by discussing the science enabled by each device. Thus, to present as clear of a record as possible, the majority of our analysis and perspectives on the field will be included at the end of the review.



### 3 Devices for X-ray scattering and diffraction

#### 3.1 Brief theory and overview

In microfluidic and millifluidic synchrotron X-ray analysis to date, scattering- and diffraction-based methods have received the most attention. The phenomenon of X-ray scattering results from elastic and inelastic interactions between incoming X-ray photons and the electrons within a sample.<sup>104</sup> Focusing on the more common methods that utilize elastic X-ray scattering (of which diffraction is a special case), these provide the user with information on the length-based properties of a sample, such as its structure, size, and shape, depending on the scattering angle at which photons are analyzed.<sup>104,105</sup> This dependence is well described by the relation formulated by W. L. Bragg in 1912:

$$\lambda = 2d \sin \theta \quad (1)$$

where  $\lambda$  is the wavelength of the incident X-rays,  $\theta$  is the scattering angle, and  $d$  is the associated distance within the sample.<sup>104</sup> Consequently, for so-called “hard” X-rays with energies  $>5$  keV (or wavelengths  $<2.5$  Å) used in most scattering and diffraction experiments, wide angles above  $\sim 5\text{--}10^\circ$  provide atomic-scale structural information and smaller angles provide information on nanoscale features.

This distinction has led to the development of two groups of techniques: those based on X-ray diffraction (XRD) and those based on small-angle X-ray scattering (SAXS). The term “wide-angle X-ray scattering” (WAXS) also appears in the literature and is equivalent to X-ray diffraction. “XRD” is a term used by crystallographers and engineers, especially with crystalline samples that produce sharp Bragg peaks, whereas “WAXS” is preferred by SAXS practitioners, especially with poorly crystalline or amorphous samples. While there are a variety of different experimental setups for performing SAXS and XRD/WAXS analysis, the most obvious difference between the two groups is the position of the detector. Wide angles are analyzed when the detector is close to the sample (normally within  $\sim 5\text{--}50$  cm), whereas small angles are more easily accessed when the detector is a meter to several meters away or more. By convention, XRD data are typically plotted as a function of  $2\theta$  and scattering data as a function of the scattering vector,  $q = (4\pi/\lambda)\sin(\theta)$ . Micro- and milli-fluidic devices for performing both SAXS and XRD/WAXS analysis are discussed below (Table 1).

#### 3.2 SAXS

**3.2.1 Early work.** Microfluidic SAXS analysis began around the year 2000, when it was utilized to study protein folding in response to chemical stimuli.<sup>134,135</sup> To our knowledge, the first microfluidic SAXS experiments on inorganic samples did not take place until close to a decade later. Merlin *et al.* used a polydimethylsiloxane (PDMS) device to study the concentration of a suspension of silica nanoparticles (NPs) by

Table 1 Micro- and milli-fluidic devices for X-ray scattering & diffraction

X-ray technique(s)	Device material(s)	Fabrication and/or assembly method	Window material, thickness	Geometry, beam pathlength	Sample(s) investigated	Beamline, source, X-ray energy	Acquisition mode, exposure time	Mixing time, $t_{\text{mix}}$	Minimum time step, $t_{\text{step}}$	Total residence time	Ref.
SAXS	PDMS	Photolithography, soft lithography, cured and plasma-bonded	PDMS, 2 × 19 μm	Transmission, 52 μm	SiO <sub>2</sub> NPs	ID13, ESRF, 12.47 keV	1.5 μm × 1.5 μm	Single-shot, 1 s	N/A	N/A	Merlin <i>et al.</i> (2011) <sup>106</sup>
SAXS	Kel-F, stainless steel, mica	Machining, threaded	Mica, unknown	Transmission, 750 μm	Au NPs with various ligands	BL 11.3.1, ALS, 11 keV	100 μm spot	Single-shot, 2–5 min	N/A	N/A	McKenzie <i>et al.</i> (2010) <sup>107</sup>
SAXS	PMMA, Kapton	Unknown	Kapton, unknown	Transmission, 1 nm	Ag NPs	BL 7.3.3, ALS, 10 keV	0.24 mm × 1 mm	Single-shot, 100 s	Unknown	0.18 ms	Takesue <i>et al.</i> (2011) <sup>108</sup>
SAXS	Device 1: PDMS/glass	Device 1: Photolithography, cured and plasma-bonded	Device 1: glass, 10 μm	Device 1: transmission, 0.3–4 mm	Au NPs	SPRING-8, 12.4 keV	370 μm	Single-shot, 900 s	Device 1: N/A	Device 1: unknown	Stehle <i>et al.</i> (2013) <sup>109</sup>
	Device 2: glass capillaries and slide	Device 2: pipette pulling, epoxy	Device 2: glass, unknown	Device 2: transmission, unknown		71-MPW-SAXS, BESSY II, 7.5–8 keV	50 μm × 300 μm ellipse		Device 2: <0.1 s	Device 2: ~3–5 s	



Table 1 (continued)

X-ray technique(s)	Device material(s)	Fabrication and/or assembly method	Window material, thickness	Geometry, beam pathlength	Sample(s) investigated	Beamline, source, x-ray energy	Beam size	Acquisition mode, exposure time	Mixing time, $t_{\text{mix}}$	Minimum time step, $t_{\text{step}}$	Total residence time	Ref.
SAXS	OSTEMER 322, Kapton	Photolithography, soft lithography, cured, cure-bonded	Kapton, 2 × 25 µm	Transmission, 300 µm	Cerium oxalate	SWING, SOLEIL, 12 keV	80 µm × 150 µm	200 ms	Unknown	33.5 ms	~6–7 s	Rodríguez-Ruiz <i>et al.</i> (2018) <sup>110</sup>
SAXS	Unknown	Compression fittings	Capillary of unknown material and wall thickness	Transmission, 2 mm outer diameter capillary	Pd NPs	1–5, SSRL, 15.5 keV	500 µm × 500 µm	Unknown	Unknown	N/A	Unknown	Fong <i>et al.</i> (2021) <sup>111</sup>
SAXS	Titanium, diamond, unknown	Machined, clamped	Diamond, 2 × unknown	Transmission, unknown	Supercritical $\text{CO}_2$	4–2, SSRL, 15 keV	Unknown	Multiframe, 50–60 × 5 s	N/A	N/A	N/A	Younes <i>et al.</i> (2023) <sup>112</sup>
GISAXS	O-ring material COC (TOPAS), glass slide	Machined, thermally bonded, clamped	COC, 2 × 500 µm	Reflection, 1 mm channel width, 7.45 mm beam footprint	Au NPs	BW4, DORIS III, 8.98 keV	65 µm × 35 µm	Single-shot, 60 min	Unknown	N/A	N/A	Moulin <i>et al.</i> (2008) <sup>113</sup>
GISAXS	COC (TOPAS), polymer-coated glass slide	Machined, thermally bonded, clamped	COC, 2 × 500 µm	Reflection, 1 mm channel width, beam footprint	Au NPs	BW4, DORIS III, 8.98 keV	30 µm × 60 µm	Single-shot, 200 s	N/A	N/A	N/A	Metwalli <i>et al.</i> (2009) <sup>114</sup>
GISAXS/GIWAXS	Silicon, glass (Pyrex)	Photolithography, reactive ion etching, anodic bonding	Silicon, 10 µm	Reflection, unknown channel width, 2.9 mm beam footprint	CO oxidation on RuO <sub>2</sub> NPs	cSAXS, SLS, 11.2 keV	10 µm × 100 µm	Unknown	Unknown	N/A	23 s	Kehres <i>et al.</i> (2016) <sup>115</sup>
SAXS/WAXS	Glass capillaries, aluminum tube	Pipette pulling, compression fittings	PET (Melinex), 2 × 250 µm	Transmission, 3 mm	2,6-Dibromo-4-nitroaniline	16.1, SRS Daresbury, 8.8 keV	Unknown	Single-shot, 30–60 s	90 ms	20 ms	~1–2 s	Alison <i>et al.</i> (2003) <sup>116</sup>
XRD	Silicon tube, hastelloy	Machined, clamped	Silicon tube, unknown	Transmission, 1 mm	CaCO <sub>3</sub> on silicon	X17B1, NSLS, 67 keV	Unknown	Single-shot, 120 s	Unknown	N/A	Unknown	Chen <i>et al.</i> (2007) <sup>117</sup>
XRD	Silicon tube, hastelloy	Machined, clamped	Silicon tube, unknown	Transmission, 1 mm	CaCO <sub>3</sub> with polymer additive	X17B1, NSLS, 67 keV	Unknown	Single-shot, 120 s	Unknown	N/A	Unknown	Chen <i>et al.</i> (2009) <sup>118</sup>
XRD	Stainless steel, hastelloy	Machined, clamped	Stainless steel tube, unknown	Transmission, 2 mm	BaSO <sub>4</sub> with polymer additives on stainless steel	X17B1, NSLS, 70 keV	Unknown	Single-shot, 120 s	Unknown	N/A	0.75 s	Mavredaki <i>et al.</i> (2011) <sup>119</sup>



Table 1 (continued)

X-ray technique(s)	Device material(s)	Fabrication and/or assembly method	Window material, thickness	Geometry, beam pathlength	Sample(s) investigated	Beamline, source, X-ray energy	Beam size	Acquisition mode, exposure time	Mixing time, $t_{\text{mix}}$	Minimum time step, $t_{\text{step}}$	Total residence time	Ref.
GIWAXS	Acetal plastic, Kapton	Machined, clamped	Kapton, 2 × 125 $\mu\text{m}$	Reflection, 15 mm channel width, 717 $\mu\text{m}$ beam footprint, 55 $\mu\text{m}$ penetration depth	FeCO <sub>3</sub> on X65 stainless steel	115, diamond, 40 keV	100 $\mu\text{m}$ diameter	Multiframe, 5 × 60 s	Unknown	Unknown	Unknown	Burkle <i>et al.</i> (2016) <sup>120</sup>
SAXS/WAXS	Silicon, glass (Pyrex)	Photolithography, wet etching, anodic bonding	Glass, 250 $\mu\text{m}$ , silicon, 280 $\mu\text{m}$	Transmission, 220 $\mu\text{m}$	CaCO <sub>3</sub>	ID02, ESRF, 12.49 keV	50 $\mu\text{m}$ × 50 $\mu\text{m}$	Single-shot, 200 ms	Unknown	N/A	Unknown	Buvier <i>et al.</i> (2015) <sup>121</sup>
Powder XRD	PMMA, PTFE, Kapton, silicone	UV laser cutting, clamped	Kapton, 2 × 75 $\mu\text{m}$	Transmission, 300 $\mu\text{m}$	CaCO <sub>3</sub> with nucleating agents	ID13, ESRF, 13 keV	12 $\mu\text{m}$ × 15 $\mu\text{m}$	Multiframe, 1000 × 20 ms	~1 s	4 s	140 s	Levenstein <i>et al.</i> (2020) <sup>102</sup>
Powder XRD	PMMA, PTFE, Kapton, silicone	UV laser cutting, clamped	Kapton, 2 × 75 $\mu\text{m}$	Transmission, 300 $\mu\text{m}$	CaCO <sub>3</sub> with nucleating agents, Au NPs, iron	ID13, ESRF, 15 keV	200 $\mu\text{m}$ × 200 $\mu\text{m}$	Single-shot, 60–120 s	~10 s	9 s	325 s	Levenstein <i>et al.</i> (2019) <sup>122</sup>
Powder XRD	FEP, PTFE, Kapton tubes	Custom machined fittings, silicone sealant, tubing	Kapton tube, 95 $\mu\text{m}$ wall	Transmission, 3.19 mm	Urea: barbituric acid, carbamazepine	111, diamond, 15 keV	1 mm × 1 mm	Multiframe, 200 $\mu\text{m}$ × 200 $\mu\text{m}$	~1 s	4 s	140 s	Levenstein, Wayment <i>et al.</i> (2020) <sup>123</sup>
SAXS and WAXS	OSTEMER 322	Photolithography, soft lithography, cured and laminated	OSTEMER 322, 2 × 200 $\mu\text{m}$	Transmission, 150 $\mu\text{m}$	Au NPs, cerium oxalate	SWING, SOLEIL, 12 and 16 keV	50 $\mu\text{m}$ × 125 $\mu\text{m}$	Multiframe, 100 × 50 ms	~0.5 s	6 ms	30 s	Lange <i>et al.</i> (2020) <sup>92</sup>
SAXS/WAXS	PDMS/glass	Photolithography, soft lithography, cured and laminated	Fused silica/Kapton tube, 250 $\mu\text{m}$	Transmission, Iron oxide NPs	122, diamond, 12.4 keV	40 $\mu\text{m}$ × 40 $\mu\text{m}$	Multiframe, 1000 × 20 ms	~1 s	20 s	130 s	Radajewski <i>et al.</i> (2021) <sup>124</sup>	
Single-crystal XRD	Custom formulated RLV-1 resin	3D printing (DLP)	50 $\mu\text{m}$ wall 3D-printed resin, 1.3 mm	Transmission, ~100–250 $\mu\text{m}$	CaSO <sub>4</sub> ·2H <sub>2</sub> O, protein crystals	ID30-A3, ESRF, 12.82 keV	30 $\mu\text{m}$ × 50 $\mu\text{m}$	Unknown	~1.5 s	N/A	N/A	van der Linden <i>et al.</i> (2020) <sup>125</sup>
SAXS and WAXS	Glass capillary, PTFE tubing, polymer fittings	Tube crimping, compression fittings, heat-shrink tubing	Borosilicate capillary, 2 mm	Transmission, 2 mm	YVO <sub>4</sub> :Eu NPs	ID30-B, ESRF, 12.41 keV	10 $\mu\text{m}$ × 10 $\mu\text{m}$	Unknown	~250 ms	N/A	400 ms (longer using stopped flow and peristaltic pump)	Fleury <i>et al.</i> (2014) <sup>126</sup>

Table 1 (continued)

X-ray technique(s)	Device material(s)	Fabrication and/or assembly method	Window material, thickness	Geometry, beam pathlength	Sample(s) investigated	Beamline, source, x-ray energy	Mixing time, $t_{mix}$	Minimum time step, $t_{step}$	Total residence time	Ref.
Powder XRD	Glass capillary, PTFE tubing, polymer fittings	Compression fittings, tubing coiling	Quartz capillary, 200 $\mu\text{m}$ wall	Transmission, 1 mm	Iron oxide NPs	XRD1, Elettra, 12.4 keV	Unknown	Single-shot, 10 min	~50 ms	N/A
SAXS and WAXS	Glass capillary, PTFE tubing, polymer fittings	Tube crimping, compression fittings, heat-shrink tubing	Borosilicate capillary, 50 $\mu\text{m}$ wall	Transmission, 1.5 mm	Cerium oxalate	SWING, SOLEIL, 16 keV	375 $\mu\text{m}$ $\times$ 75 $\mu\text{m}$	Multiframe, 20 $\times$ 1 s for SAXS and 20 $\times$ 4 s for WAXS	~250 ms	N/A
Total scattering/PDF	Glass capillary, Kapton tube, metal fittings	Compression fittings	Kapton tube, unknown	Transmission, ZIF-8 2 mm	ZIF-8	28-ID-2, NSLS-II, 67.86 keV	Unknown	“Rapid acquisition mode”, ~1–10 s	250 ms (longer using stopped flow)	Durelle <i>et al.</i> (2023) <sup>128</sup>
Total scattering/PDF	Glass capillary, Kapton tube, stainless steel fittings	Compression fittings, 3D-printed adapters	Glass capillary, 100 $\mu\text{m}$ wall	Transmission, 1.3 mm or 0.9 mm	$\text{Al}^{3+}$ , FeS	11-ID-B, APS, 58.62 keV	0.5 mm $\times$ 0.5 mm	Single-shot, 1, 10, and 100 s	$\leq$ 0.1 s	0.05–2 s
Total scattering/PDF	Carbon fiber capillary, polyethylene, rubber tubing	Compression fittings	Epoxy-aligned carbon fiber capillary, 0.67 mm	Transmission, 1.83 mm	Pt NP-coated graphene, Fe–Ni layered double hydroxide NPs, LiCoO <sub>2</sub>	11-ID-B, APS, 58.65 keV	Unknown	Unknown	0.01–0.1 s	0.1–10 s
Total scattering/PDF and GIWAXS	Kapton, VeroClear-RGD810 resin, porous glass array, electrode materials	Epoxy, atomic layer deposition of electrodes, compression fittings	Kapton, 2 $\times$ 25 $\mu\text{m}$	Transmission, 2.4 mm	Amorphous cobalt oxide thin films	11-ID-B, APS, 58.7 keV	300 $\mu\text{m}$ $\times$ 500 $\mu\text{m}$	Single-shot, 2–5 min	N/A	N/A
						6-ID-D, APS, 100.3 keV	300 $\mu\text{m}$ $\times$ 500 $\mu\text{m}$			Kwon <i>et al.</i> (2019) <sup>133</sup>
						11-ID-D, APS, 15 keV	15 $\mu\text{m}$ vertical			

solvent evaporation.<sup>106</sup> The main channel of the device was made within a thin PDMS membrane ( $\sim 20\ \mu\text{m}$  wall thickness) to enable the transmission of X-rays. The gas permeability of this thin PDMS layer was also exploited to create a steady-state evaporation-driven flow of water, which slowly concentrated the NPs from the end of the microchannel inwards, until they were converted into a solid-state colloidal crystal at a NP volume fraction of 30–40%. By using a high flux, microfocused beam, the researchers were able to perform the study with high spatial and temporal resolution, scanning the beam along the channel in a grid with  $50\ \mu\text{m}$  steps and 1 s X-ray exposure time per step.

Around the same period, several millifluidic studies were also performed. McKenzie *et al.* designed a custom flow-cell to enable simultaneous *in situ* SAXS and ultraviolet-visible (UV-vis) spectroscopy and validated it by determining the size distribution of pre-made suspensions of reference Au NPs (Fig. 3a).<sup>107</sup> The ability to perform both *in situ* and *ex*

*situ* UV-vis allowed for quality control and the comparison of *in situ* SAXS data to subsequent *ex situ* transmission electron microscopy (TEM) of the different Au NP standards after surface-deposition, which would be especially important when characterizing experimental samples. Takesue *et al.* performed *operando* SAXS analysis of Ag NP synthesis using a poly(methyl methacrylate) (PMMA) device with Kapton X-ray windows (Fig. 3b).<sup>108</sup> By utilizing a very high flow rate ( $120\ \text{mL min}^{-1}$ ), the authors obtained a turbulent flow, which facilitated rapid mixing of reactants and also sub-ms time resolution through the vertical movement of the device in the beam. In this case, the continuous flow of solution permitted long X-ray exposures ( $>1\ \text{min}$ ) at each channel position to obtain good scattering statistics of dilute intermediate species without sacrificing time resolution.

**3.2.2 Mitigation of device fouling.** In many precipitation and synthesis scenarios, the continuous flow of solution can

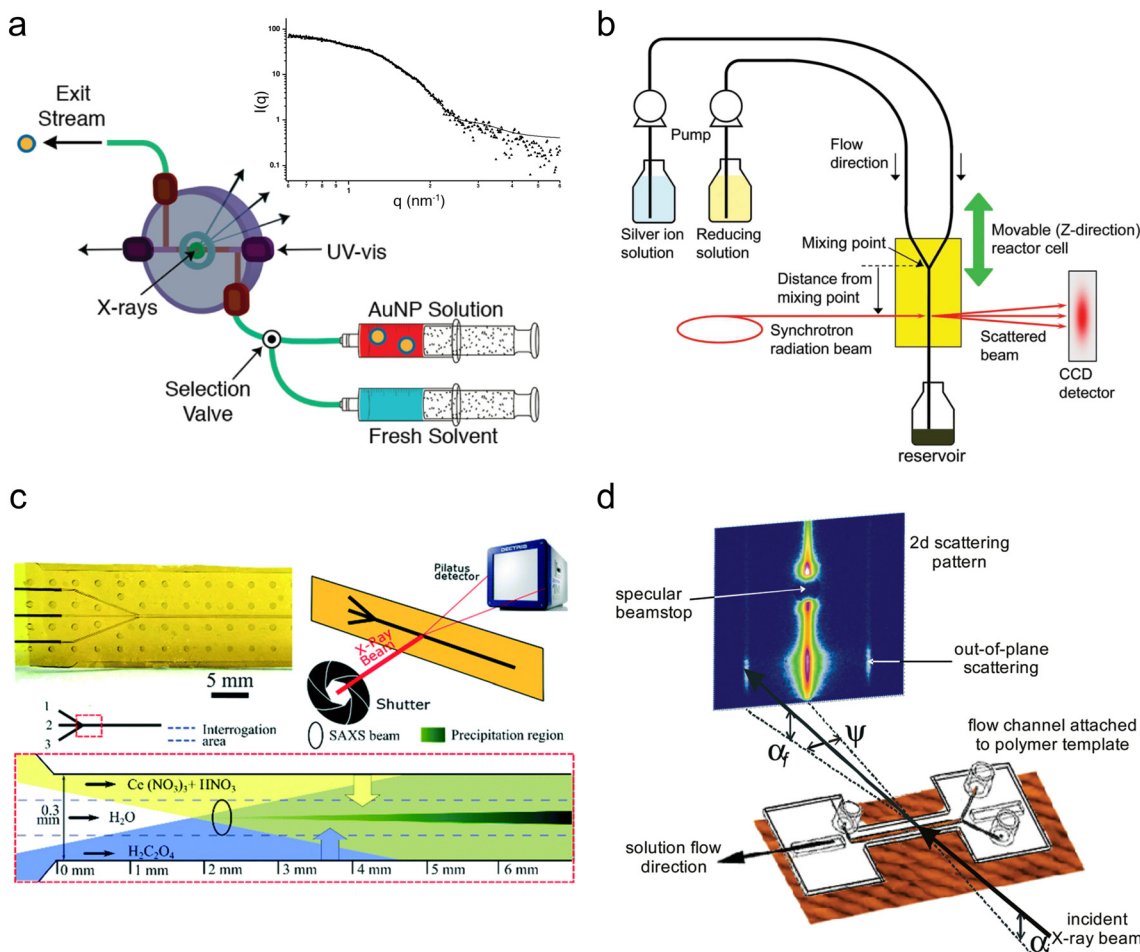


**Fig. 3** Devices for SAXS analysis. (a) Millifluidic flow-cell for simultaneous SAXS and UV-vis of nanoparticle solutions. Inset: Example 1D scattering pattern of AuNP suspension (adapted with permission from McKenzie *et al.*, 2010; Copyright 2010 American Chemical Society)<sup>107</sup> (b) Experimental setup for sub-ms synchrotron SAXS measurements of the early stages of AgNP synthesis (reprinted with permission from Takesue *et al.*, 2011; Copyright 2011 American Chemical Society).<sup>108</sup> (c) Continuous flow microfluidic device for the study of cerium oxalate precipitation (top left: photo of the device; top right: measurement geometry; bottom: illustration of the mixing configuration with the water buffer flow; adapted with permission from Rodríguez-Ruiz *et al.* 2018; Royal Society of Chemistry).<sup>110</sup> (d) Example of a microfluidic GISAXS experiment (reprinted with permission from Metwalli *et al.*, 2009; Copyright 2009 American Chemical Society).<sup>114</sup>



result in the build-up of products on channel walls.<sup>136,137</sup> This can convolute or degrade the X-ray signal, change the chemical environment and modify reaction products, and potentially lead to device failure.<sup>102,138</sup> For this reason, Stehle *et al.* performed the first SAXS analysis of nanoparticle synthesis using droplet microfluidics.<sup>109</sup> They utilized two devices: one in which a pre-made solution of Au NPs was emulsified in a PDMS chip and injected into a glass capillary for analysis and another device made from nested glass capillaries where the synthesis and analysis were both performed *in situ*. They were able to obtain a SAXS signal from the Au NPs synthesized *in situ*, however, the long exposure times employed (900 s) meant that the acquired scattering curves contained a mixture of scattering from many droplets and the surrounding continuous oil phase. We will see in the next subsection different routes for isolating droplet scattering from that of the rest of the flow to obtain a higher signal-to-noise ratio.

Another method for limiting precipitation on channel walls without producing droplets is by introducing a strong 'buffer' flow of water between reactant streams. This delays their contact and slows down their mixing to prevent a sudden precipitation event that could instantly clog a device. Such a method was employed by Rodríguez-Ruiz *et al.* in an OSTEMER-Kapton microfluidic device to study the precipitation of the highly insoluble, rare earth mineral, cerium oxalate (Fig. 3c).<sup>110</sup> Using a flow of water  $>10$  times faster than their reactant flows (also resulting in a  $>10$  times reactant dilution), they were able to successfully acquire scattering curves from within the first second of the reaction. However, the slowed mixing resulting from the water flow meant that it was not possible to analyze reaction times  $<0.2$  s due to inconsistent background signal.

**3.2.3 Machine learning.** An exciting recent application of *in situ* SAXS comes from Fong *et al.*, who used a millifluidic continuous flow reactor and machine learning to optimize the synthesis of Pd nanoparticles in real-time.<sup>111</sup> Their setup consisted of pumps containing the reactants, surfactants, and solvents coupled to a mixing manifold and heated capillary tube. SAXS data acquired at the outlet of the tube were automatically processed by a control computer, which could then adjust the flow rates and reactor temperature in a closed feedback loop. After performing a short grid search to roughly map a reaction parameter space, the system was able to rapidly converge on conditions to synthesize nanoparticles with targeted size, concentration, and yield using Bayesian optimization (BO). Similarly, Younes *et al.* used BO to efficiently determine the phase diagram of supercritical CO<sub>2</sub> using SAXS and a high-pressure microfluidic cell.<sup>112</sup> Correlation lengths were extracted from SAXS curves obtained at different temperature and pressure combinations, and the BO algorithm was shown to accurately predict the correlation length maximum for each temperature after measuring at only 5–10 different pressures. This required 3–6 fewer measurements with the microfluidic device than

when using a more traditional statistical approach (the bisection method) and could be used in the future to eliminate unnecessary data collection.

**3.2.4 GISAXS.** Standard SAXS measurements made using a transmission geometry are good for obtaining information from bulk samples and liquids, but they are less sensitive to surface features.<sup>139</sup> Therefore, there has also been interest in performing grazing incidence SAXS (GISAXS) in a reflection geometry to study interfacial phenomena occurring within microfluidic devices. Moulin *et al.* developed a device for this purpose made from cyclic olefin copolymer (COC, TOPAS®) that could be reversibly clamped to various substrates of interest (Fig. 3d).<sup>113</sup> They confirmed its suitability for GISAXS by studying the interaction between a flow of Au NPs and a glass surface. Later, the team followed up this study by using the same device to monitor the templated growth of Au nanowires on a polymer substrate.<sup>114</sup> Similarly, Kehres *et al.* designed a silicon-based device for studying gas–solid interactions in catalysis.<sup>115</sup> Prior to device bonding, a catalyst layer is deposited, and then catalytic reactions at the interface can be monitored using different gas mixtures, temperatures, and pressures. Their device was also configured to work with inline mass spectrometry while simultaneously collecting grazing incidence WAXS (GIWAXS) data.

### 3.3 XRD/WAXS

**3.3.1 Millifluidics.** While *in situ* microfluidic XRD/WAXS analysis is a more recent trend than microfluidic SAXS (excluding for structural biology), several groups implemented millifluidic XRD/WAXS quite early, and often combined with SAXS. Alison *et al.* utilized a glass capillary-based plug-flow reactor to investigate the crystallization of 2,6-dibromo-4-nitroaniline, a model compound for studying crystallization mechanisms.<sup>116</sup> Using a high flow rate and a turbulent 'teardrop' mixer, they observed the formation of non-crystalline particles by SAXS during the first second of precipitation and prior to the appearance of crystalline diffraction observed by WAXS. This combination of techniques thus allowed them to evidence potential crystallization pathways that do not follow single-step classical nucleation theory, which does not account for the formation of non-crystalline intermediate phases. Likewise, Chen *et al.* developed a millifluidic flow cell for studying scale formation from salt brines on different materials (including silicon and stainless steel).<sup>117</sup> Beginning with a study of the effect of temperature on CaCO<sub>3</sub> scaling, the authors went on to study both BaSO<sub>4</sub> and CaCO<sub>3</sub> scaling in the presence of anti-scaling agents.<sup>118,119</sup> Later, the same team developed an updated flow-cell that could perform GIWAXS studies of steel corrosion combined with simultaneous electrochemical monitoring (Fig. 4a).<sup>120</sup>

**3.3.2 Microfluidics.** More recently, researchers have miniaturized these WAXS and SAXS/WAXS studies further by utilizing microfluidic devices. Beuvier *et al.* studied the



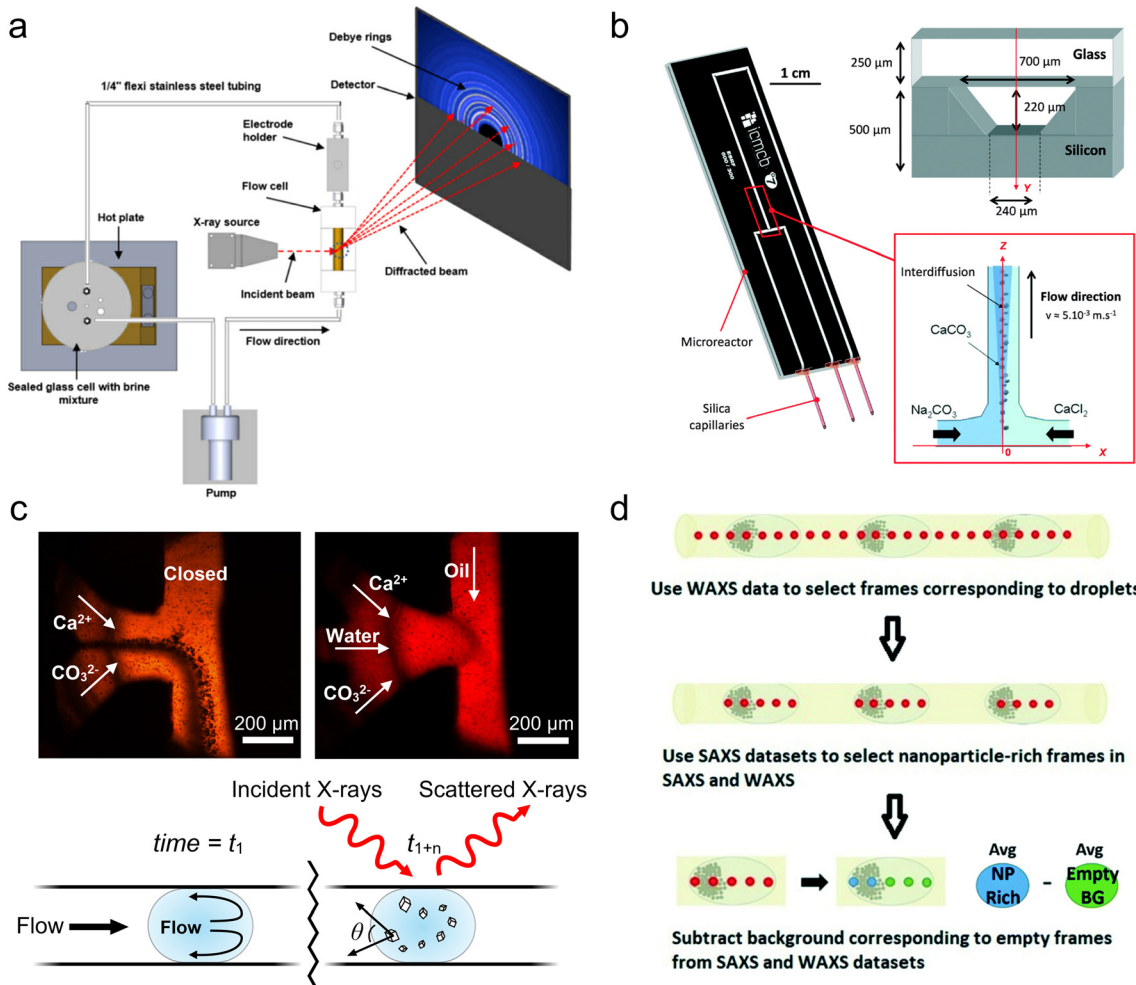


**Fig. 4** Devices for WAXS/XRD analysis. (a) An experimental setup for millifluidic GIWAXS and electrochemical measurement of steel corrosion (reprinted from Burkle *et al.* 2016 with the permission of AIP Publishing).<sup>120</sup> (b) A hybrid silicon-glass microfluidic device for continuous flow study of  $\text{CaCO}_3$  crystallization (reprinted with permission from Beuvier *et al.* 2015; Royal Society of Chemistry).<sup>121</sup> (c) Comparison of  $\text{CaCO}_3$  crystallization in microfluidic devices in continuous flow (top left) versus under conditions optimized to prevent scaling (top right). An illustration of the distance-to-time conversion enabled when scaling is prevented (bottom) (adapted with permission from Levenstein *et al.*, 2020; Royal Society of Chemistry).<sup>102</sup> (d) A workflow for SAXS/WAXS frame selection and background subtraction for droplet microfluidics (reprinted with permission from Radajewski *et al.*, 2021; Royal Society of Chemistry).<sup>124</sup>

precipitation of  $\text{CaCO}_3$  by SAXS/WAXS using a hybrid silicon-glass device (Fig. 4b),<sup>121</sup> where the single-crystalline silicon layer provided a very low SAXS background and the glass layer permitted visual monitoring of the flow. WAXS enabled the identification of the structure/polymorph of the  $\text{CaCO}_3$  crystals formed, and the presence of streak-like crystal truncation rods in the SAXS patterns enabled the determination of their micron-scale size. Similar to the above studies of mineral scaling, the authors observed the rapid growth of  $\text{CaCO}_3$  on device surfaces starting from the point of reactant mixing. However, as discussed in the previous section, for many applications, such surface growth is undesirable, making it more difficult to study processes occurring in the bulk flow. Levenstein *et al.* also performed a WAXS study of  $\text{CaCO}_3$  growth in a microfluidic device in order to test several different flow configurations and determine those best for minimizing device scaling.<sup>102</sup> They

identified that a combination of water buffer between reactants, hydrophobic surface treatment, segmented water-in-fluorinated oil flow, and triblock co-polymer surfactant facilitated studies of  $\text{CaCO}_3$  precipitation for ~1 hour without significant crystallization on surfaces (Fig. 4c). Importantly, this enabled the crystallization process to be studied as a function of a droplet's position along the channel with time, where the rotation of crystals within the droplets additionally allowed diffraction to be collected from a range of scattering angles  $\theta$ .

In order to isolate scattering from the droplets from that of the surrounding fluorinated oil phase, the authors implemented a multiframe data acquisition and processing approach first used for bioSAXS.<sup>101</sup> Briefly, short 20 ms frames were captured at a rate of 50 Hz and WAXS frames containing the characteristic scattering of the oil phase were identified and discarded. The remaining frames were then

summed to obtain a good signal-to-noise ratio at each position.<sup>122</sup> This WAXS-based technique was later implemented in a millifluidic flow system,<sup>123</sup> and a similar technique was also performed by Lange *et al.*, who utilized SAXS frames to distinguish between the water and oil phases.<sup>92</sup> More recently, Radajewski *et al.* presented an innovative data processing technique combining both WAXS and SAXS frame selection to isolate not only droplets, but also the sections of droplets with the highest concentration of sample for subsequent data treatment (Fig. 4d).<sup>124</sup> Alternatively, for studies not requiring *operando* measurements, van der Linden *et al.* developed a 3D-printed device for storing and measuring samples contained within isolated, static droplets to avoid signal from the oil phase.<sup>125</sup>

**3.3.3 Plug-and-play devices.** Despite this progress in microfluidic SAXS/WAXS studies, a growing trend is the use of simpler ‘plug-and-play’ millifluidic devices and set-ups that lower the fabrication, cost, and time barriers to performing *in situ* flow experiments. These often make use of commercially available compression fittings (e.g., Upchurch/IDEX, Swagelok) and/or mixers, the outlet of which is connected to a thin-walled glass capillary for performing SAXS and/or WAXS analysis. For example, Fleury *et al.* made use of a simple home-made turbulent mixer<sup>140</sup> to study the synthesis of luminescent Eu-doped YVO<sub>4</sub> nanoparticles.<sup>126</sup> Using combined SAXS, WAXS and fluorescence spectroscopy, they observed that the final fluorescent nanoparticles were formed from non-fluorescent amorphous aggregates, the size of which defined the size of the product crystallites. Similarly, Besenhard *et al.* studied the precipitation of iron oxide nanoparticles by XRD using commercial mixers combined with custom temperature controlled modules of varying lengths to adjust the age of the material probed in the beam (Fig. 5a).<sup>127</sup> They additionally tested mixers with different internal diameters, and thereby different Reynolds numbers, and showed that they produced similarly sized nanoparticles with production that was consistent over >30 min of operation. Recently, Durelle *et al.* used a simple device to compare *in situ* SAXS and WAXS measurements of crystal nucleation rates to traditional incubation-counting methods used in chemical engineering and found that traditional methods could result in underestimates of several orders of magnitude.<sup>128</sup> This illustrates clearly the power of even simple millifluidic continuous flow devices for *in situ* X-ray scattering. Many other studies utilizing such devices exist and cannot all be covered here.<sup>141–143</sup>

#### 3.4 Total scattering/PDF

In this final scattering section, we will cover recent efforts in millifluidic X-ray total scattering, used for performing pair distribution function (PDF) analysis of atomic to nanoscale correlations within materials. These measurements are usually performed at high energy beamlines to incorporate scattering from small length scales since wavelength and energy are inversely proportional and wavelength and the

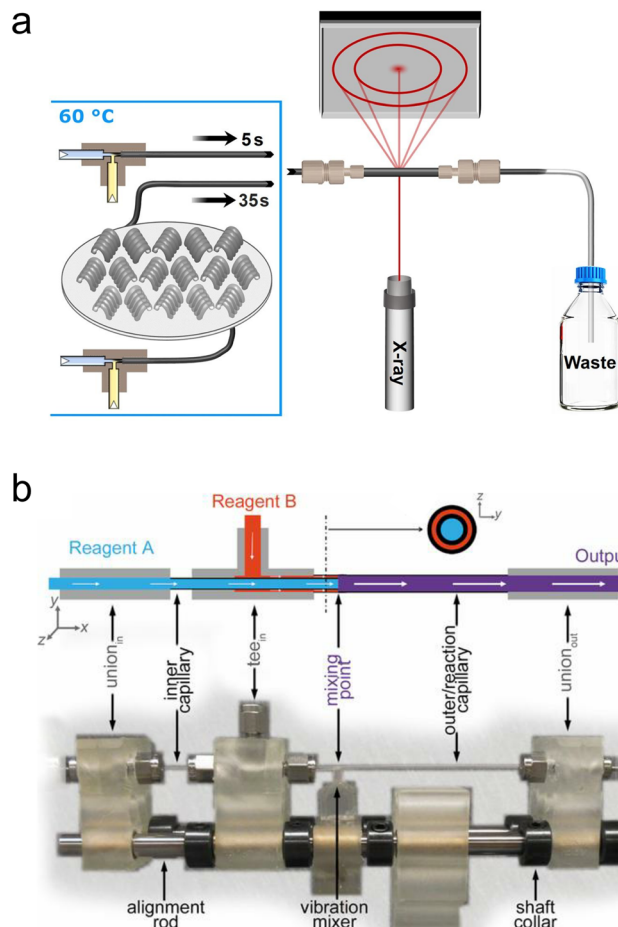


**Fig. 5** Simple ‘plug-and-play’ millifluidic devices for XRD/WAXS/PDF analysis. (a) A setup for *in situ* SAXS/WAXS utilizing commercial mixers and custom temperature-controlled sections for time-delay (reprinted from Besenhard *et al.*, 2020; with permission from Elsevier).<sup>127</sup> (b) A Norby-style device with active mixing for X-ray PDF analysis (adapted with permission from Beauvais *et al.* 2022; IUCr).<sup>131</sup>

probed length scale are directly proportional at fixed  $\theta$  (see eqn (1)). By utilizing crystalline Bragg diffraction and diffuse scattering at large angles normally neglected during XRD analysis (*i.e.*, the “total” scattering pattern), the PDF technique provides information on not only long-range crystalline order within a sample, but also short-range correlations within even amorphous materials.<sup>144</sup> These techniques are additionally well suited for *in situ* analysis because the high energies impart more penetration power and allow the use of thicker and denser samples and sample environments.

Terban *et al.* performed *in situ* X-ray PDF analysis of the synthesis of the zeolitic imidazolate framework, ZIF-8,<sup>129</sup> using a simple millifluidic continuous flow device consisting of a Kapton tube, a metallic frame and commercial fittings mounted on a goniometer head in the same way as a Norby cell. With this setup, they were able to observe the formation of long-lived solution species and amorphous solid phases during the synthesis of this model metal-organic



framework. Similarly, Beauvais *et al.* developed a millifluidic device resembling a Norby design but comprising an active vibration mixing element (Fig. 5b).<sup>131</sup> They tested a variety of injection capillary sizes, types and materials, including glass and Kapton, and converged on a design that fully mixed reactants in less than a few hundred milliseconds. The authors validated the system by studying the hydrolysis of  $\text{Al}^{3+}$  and then went on to study the formation of FeS by a ligand-exchange reaction, demonstrating the presence of previously unknown intermediate phases in the form of nanosheets.<sup>130</sup>

A few groups have also developed innovative cells that enable *in situ* X-ray PDF measurements of electrochemical processes. For example, Young *et al.* designed a millifluidic electrochemical cell with an epoxy-aligned carbon fiber capillary serving as both the working electrode and the X-ray window.<sup>132</sup> A recirculating flow of electrolyte solution could be applied through the capillary, and various samples relevant to electrocatalysis and batteries could be loaded and measured during cycling, including Pt nanoparticle-coated carbon nanotubes and  $\text{LiCoO}_2$  powder. Kwon *et al.* developed their own electrochemical cell consisting of a 3D porous glass capillary-array (GCA) sitting in an electrolyte reservoir with Kapton walls to facilitate X-ray analysis.<sup>133</sup> The GCA array was coated by gold and either indium tin oxide (ITO) or indium zinc oxide (IZO) to serve as the working electrode, and fresh electrolyte was pumped through the GCA pores from below the reservoir using a syringe pump during cycling.

## 4 Devices for X-ray spectroscopy

### 4.1 Brief theory and overview

X-ray spectroscopy techniques are utilized to obtain chemical information such as elemental composition, oxidation state, and coordination number. This section will be focused primarily on X-ray absorption spectroscopy (XAS), which is one of the main groups of X-ray spectroscopic techniques and the one utilized in most previous micro- and milli-fluidic studies. Another major type of X-ray spectroscopy is X-ray photoelectron spectroscopy (XPS), but to our knowledge, *in situ* XPS has been performed exclusively in free liquid jets,<sup>145</sup> likely due to the poor transmission of electrons exiting through device windows. There are two primary acquisition modes for XAS analysis: transmission and fluorescence. The most common, transmission XAS, is based on measuring the incident beam flux ( $I_0$ ) and the flux of the beam transmitted through the sample ( $I$ ), which are related by the Beer-Lambert law:

$$I = I_0 \cdot e^{-\mu(\lambda)x} \quad (2)$$

where  $\mu(\lambda)$  is the wavelength-dependent linear attenuation coefficient of the sample and  $x$  is the sample thickness.<sup>146</sup> XAS spectra are collected by scanning the wavelength of the incident X-ray beam across an absorption edge of an element

of interest in the sample, where the shape and position of the edge and post-edge oscillations are used to determine the chemical speciation of the target element. The location of the collected spectra in relation to the absorption edge subdivides XAS into different techniques based on where the data are collected, such as X-ray absorption near-edge structure (XANES) and extended X-ray absorption fine structure (EXAFS) spectroscopy for the edge and post-edge regions, respectively.<sup>146</sup>

XAS is performed in fluorescence mode by monitoring the total yield of secondary X-rays at  $90^\circ$  from the incident beam (normally  $45^\circ$  from the sample) rather than the transmitted flux, which is helpful when using thick or highly dilute samples.<sup>146,147</sup> For both modes, different acquisition strategies using polychromatic radiation and position/energy-resolved detectors can also be employed to more rapidly record full spectra without scanning the energy of the incident beam.<sup>148–150</sup> The closely related technique of X-ray fluorescence (XRF) has also been performed with microfluidic devices,<sup>151,152</sup> although primarily for 2D elemental mapping and laboratory analysis, and will thus be covered in sections 5 and 6, respectively. Further details on the micro- and milli-fluidic devices for X-ray spectroscopy discussed below can be found in Table 2.

### 4.2 XAS

**4.2.1 Hard X-rays.** Unlike with scattering methods, microfluidic XAS was developed and has been primarily conducted for the physical rather than biological sciences. Early work in micro- and milli-fluidic XAS was focused on devices designed for analyzing heavy elements at hard X-ray energies. The first devices, such as from Hoffman *et al.*, were made from corrosion-resistant metal alloys and diamond windows for studying high pressure phenomena.<sup>153,154</sup> Subsequent devices were made from silicon and glass using more conventional microfluidic fabrication processes and applied to catalysis and nanoparticle synthesis. Sankar *et al.* utilized such a device to study the dehydrogenation of methanol on a silver catalyst with XANES and EXAFS.<sup>155</sup> Using fluorescence mode acquisition at the Ag K-edge (25.5 keV), the authors evidenced a cyclical process of oxidation/reduction of the metal catalyst involved in the conversion of methanol to formaldehyde.

Chan *et al.* also utilized a silicon-glass microfluidic device to monitor a cation exchange reaction in semiconducting CdSe nanocrystals by XANES at the Se K-edge (12.66 keV).<sup>156</sup> In addition to silicon and glass, their device comprised a 2  $\mu\text{m}$  thick silicon nitride/SU-8 X-ray window designed for performing measurements in fluorescence mode (Fig. 6a). In their experiment, a suspension of CdSe nanocrystals was introduced in a hydrodynamic flow focusing geometry surrounded by a sheath flow of  $\text{Ag}^+$  ions. As the ions diffused into the stream of nanocrystals, the kinetics of the  $\text{CdSe} \rightarrow \text{Ag}_2\text{Se}$  transformation could be followed over  $\sim 100$  ms with  $\sim 8$  ms time resolution owing to the narrow channel width,



Table 2 Micro- and milli-fluidic devices for X-ray spectroscopy

X-ray technique(s)	Device material(s)	Fabrication and/or assembly method	Window material, thickness	Mode, beam pathlength	Sample(s) investigated	Beamline, source, X-ray energy	Beam size	Mixing time, $t_{mix}$	Minimum time step, $t_{step}$	Total residence time	Ref.
XRF	Fused silica capillary, polyethylene tubing	Interference fit	Polyethylene, 193 $\mu$ m wall	Fluorescence, 580 $\mu$ m	Co, Cu, and Zn solutions	X-26A, NSLS, 10 keV	30 $\mu$ m $\times$ 40 $\mu$ m	Multiframe, N/A	N/A	N/A	Ringo <i>et al.</i> (1999) <sup>151</sup>
	Fused silica capillary, polyethylene tubing	Interference fit	Polyethylene, 355 $\mu$ m wall	Fluorescence, 380 $\mu$ m	Fe, Co, Cu, and Zn solutions	X-26A, NSLS, 10 keV	40 $\mu$ m $\times$ 40 $\mu$ m	Multiframe, N/A	N/A	N/A	Mann <i>et al.</i> (2000) <sup>152</sup>
XANES and EXAFS	Ti-6Al-4V alloy, Pt/Ir alloy, diamond (type 1B)	Machining, press fit, clamping	Diamond, 2 $\times$ 1 mm	Transmission, ~1-100 mm	Tungstate solutions	ID-20, APS, W L <sub>3</sub> -edge (10.21 keV)	1.5 mm diameter	Unknown	N/A	N/A	Hoffmann <i>et al.</i> (2000) <sup>153</sup>
XANES and EXAFS	Silicon, glass	Deep reactive ion etching, anodic bonding	Silicon, unknown	Fluorescence, $\geq$ 250 $\mu$ m	Dehydrogenation of methanol on Ag	16.5, SRS Daresbury, Ag K-edge (25.5 keV)	0.4 mm $\times$ 10 mm	Single-shot, 40 min	N/A	N/A	Sankar <i>et al.</i> (2007) <sup>155</sup>
XANES and $\mu$ XRF	Silicon, glass, silicon nitride, SU-8	Photolithography, wet etching, reactive ion etching, anodic bonding	Silicon nitride, 1 $\mu$ m, SU-8, 1 $\mu$ m	Fluorescence, 570 $\mu$ m	CdSe $\rightarrow$ Ag <sub>2</sub> Se nanocrystals	10.3.2, ALS, Se K-edge (12.66 keV)	16 $\mu$ m $\times$ 7 $\mu$ m	Multiframe, 4 $\times$ >100 s	~14 ms	~8-16 ms	~50-100 ms
XANES	Silicon, glass	Deep reactive ion etching, fusion bonding	Silicon, 300 $\mu$ m, glass, 200 $\mu$ m	Fluorescence, $\geq$ 300 $\mu$ m	Au NPs	P06, Petra III, Au L <sub>3</sub> -edge (11.92 keV)	Unknown	Unknown	<1 ms	~1 $\mu$ s	20 ms
XANES	Silicon, glass	Deep reactive ion etching, fusion bonding	Silicon, 300 $\mu$ m, glass, 200 $\mu$ m	Fluorescence, $\geq$ 300 $\mu$ m	Au NPs	SupernAS, SLS, Au L <sub>3</sub> -edge (11.92 keV)	150 $\mu$ m $\times$ 100 $\mu$ m	Single-shot, 4 min	<2 ms	~1 $\mu$ s	20 ms
XANES and EXAFS	Silicon, borosilicate glass	Deep reactive ion etching, anodic bonding	Glass, 2 $\times$ 175 $\mu$ m	Transmission and fluorescence, 742 $\mu$ m	Fe, Br, and Pb salt solutions	Balder, MAX IV, Fe K-edge (7.11 keV), Pb L <sub>3</sub> -edge (13.04 keV), Br K-edge (13.47 keV)	50 $\mu$ m $\times$ 50 $\mu$ m	Multiframe, 10 $\times$ 100 s for EXAFS and 4-6 $\times$ 25 s for XANES	N/A	N/A	Michael Raj <i>et al.</i> (2021) <sup>159</sup>
XANES/EXAFS	Unknown	Unknown	Unknown	Fluorescence, unknown	Pt NPs	118, diamond, Pt L <sub>3</sub> -edge (11.56 keV)	400 $\mu$ m $\times$ ~250 $\mu$ m	Unknown	Unknown	Unknown	Britto <i>et al.</i> (2023) <sup>160</sup>

Table 2 (continued)

X-ray technique(s)	Device material(s)	Fabrication and/or assembly method	Window material, thickness	Mode, beam pathlength	Sample(s) investigated	Beamline, source, x-ray energy	Beam size	Acquisition mode, exposure time	Mixing time, $t_{mix}$	Minimum time step, $t_{step}$	Total residence time	Ref.
XANES	PMMA	Hot embossing	PMMA, unknown	≥500 μm	Fluorescence, Co NPs	XMP, CAMD, Co K-edge (7.78 keV)	50 μm × 80 μm	Single-shot, 5–7.5 min	Unknown	~2 ms	50 s	Zinov'eva <i>et al.</i> (2007) <sup>161</sup>
XANES and EXAFS	Unknown	Unknown	Kapton, unknown	≥500 μm	Fluorescence, CdSe NPs	BL13B1, PF, 12.6–12.7 keV	1 mm × 0.5 mm	Unknown	Unknown	47–118 ms	30 s	Oyanagi <i>et al.</i> (2011) <sup>162</sup>
XANES and EXAFS	PVC, brass, graphite	Machining, clamping, pressure fittings, conductive epoxy	Kapton, unknown, graphite, 500 μm	Transmission, ~400 μm (~200 μm electrolyte and ~200 μm sample)	Iron and iron oxide phases	ID24, ESRF, Fe K-edge (7.11 keV)	50 μm × 100 μm	Multiframe, ms exposures	N/A	N/A	Unknown	Monnier <i>et al.</i> (2008) <sup>163</sup>
XANES and EXAFS	PET	Commercially purchased	PET, unknown	Fluorescence, ≥150 μm	Au nanostructures	BM30b, ESRF, Fe K-edge (7.11 keV)	30 μm × 150 μm	Multiframe, 7 min for XANES, and 3 × 30 min for XANES + EXAFS	Unknown	Unknown	~25 s (neglecting mixing time)	Monnier <i>et al.</i> (2014) <sup>164</sup>
XANES and EXAFS	PETG filament	3D printing (FDM)	3D-printed polymer, unknown	Transmission, 80 mm	Pd NPs	10-ID, APS, Au L <sub>3</sub> -edge (11.92 keV)	50 μm × 50 μm	Unknown	Unknown	5.4 ms	~25 s	Krishna <i>et al.</i> (2013) <sup>165</sup>
EXAFS	Ti-6Al-4V alloy, diamond (type IIa)	Machining, epoxy, clamping, Peltier seal	Diamond, 2 × 25 μm	Transmission, 150 μm	CaCl <sub>2</sub> solution	STM, Kurchatov, Pd K-edge (24.35 keV)	0.7 mm × 0.7 mm	Single-shot, 10 min	Unknown	~2.7 min	~17.6 min	Dobrovolskaya <i>et al.</i> (2023) <sup>166</sup>
XAS and XES	PTFE, silicon, viton O-ring	Machined, clamped	Silicon nitride, 100 nm	Fluorescence, ≥500 μm	H <sub>2</sub> O, D <sub>2</sub> O	20-BM, APS, Ca K-edge (4.04 keV)	200 μm × 180 μm	Multiframe, 3 × 20 min	N/A	N/A	~15 min	Fulton <i>et al.</i> (2004) <sup>167</sup>
			silicon carbide, 150 nm		80.1, ALS, 550 eV	Unknown	Unknown		N/A	N/A	Unknown	Fuchs <i>et al.</i> (2008) <sup>168</sup>

Table 2 (continued)

X-ray technique(s)	Device material(s)	Fabrication and/or assembly method	Window material, thickness	Mode, beam pathlength	Sample(s) investigated	Beamline, source, x-ray energy	Beam size	Mixing time, $t_{mix}$	Minimum time step, $t_{step}$	Total residence time	Ref.
XANES	Silicon, PTFE, unknown O-ring and housing material	Machined, clamped	Silicon nitride, 2 × 100 nm	Transmission, 100–800 nm	Water	BL3U, UVSOR-II O K-edge (532 eV)	200 μm × 200 μm	~13 min	Single-shot, N/A	N/A	~1 s Nagasaka <i>et al.</i> (2010) <sup>169</sup>
XANES	Silicon, stainless steel, gold, unknown O-ring material	Machined, clamped	Silicon nitride, 2 × 100 nm	Transmission, 250 nm	Water, CoCl <sub>2</sub> solution, methanol–water mixture	PM3, BESSY II, O K-edge (532 eV) and Co L <sub>3</sub> -edge (778.6 eV)	100 μm diameter	Unknown	N/A	Unknown	Schreck <i>et al.</i> (2011) <sup>170</sup>
XANES and μXRF	Silicon, PDMS	Wet etching, photolithography, soft lithography, plasma bonding	Silicon nitride, 450 nm	Fluorescence, 57 μm	CaCO <sub>3</sub>	Phoenix, SLS, Ca K-edge (4.04 keV)	50 μm × 75 μm	10–15 × 8 min	Multiframe, <10 ms	~1 ms	~5 s Probst <i>et al.</i> (2021) <sup>171</sup>
XANES and μXRF	Silicon, PDMS or glass	Wet etching, deep reactive ion etching, photolithography, soft lithography, plasma bonding	Silicon nitride, 120 nm	Fluorescence, 127 μm	Ca <sup>2+</sup> ions and EDTA	Phoenix, SLS, Ca K-edge (4.04 keV)	3 μm × 3 μm	~100 min total	Multiframe, <2 ms	0.365 ms	2.7 s Brenker <i>et al.</i> (2022) <sup>172</sup>
XANES/EXAFS	Stainless steel, graphite, quartz wool	Machined, clamped	Graphite, 300 μm CaF <sub>2</sub> /glue, 300 μm	Transmission, 2 mm	Pt/Al <sub>2</sub> O <sub>3</sub> catalyst	SupersAXS, SLS, Pt L <sub>3</sub> -edge (11.56 keV)	100 μm × 100 μm	Single-shot, 1 s	N/A	N/A	~5 s Chiarello <i>et al.</i> (2014) <sup>173</sup>
XANES/EXAFS	Aluminum, CaF <sub>2</sub>	Machined, pressure fittings	Al, 2 × 250 μm	Transmission, 5 mm	Pd/Al <sub>2</sub> O <sub>3</sub> catalyst	ID12-EDE, diamond, Pd K-edge (24.35 keV)	500 μm × 150 μm	200 × 4.8 ms for EXAFS, single-shot 4.8 ms for XANES	N/A	N/A	Unknown Dann <i>et al.</i> (2019) <sup>174</sup>
XANES/EXAFS	Silicon, glass	Photolithography, deep reactive ion etching, anodic bonding	Si, 2 × 250 μm	Transmission, 3 mm	Pd/Al <sub>2</sub> O <sub>3</sub> catalyst	B18, diamond, Pd K-edge (24.35 keV)	200 μm × 100 μm	Single-shot, 180 s	N/A	N/A	Unknown Venezia <i>et al.</i> (2020) <sup>175</sup>
XANES and XES	Fused silica, Kapton	Laser-selective wet etching	Kapton tube, 27 μm wall thickness	Fluorescence, 510 μm	Ferricyanide and ascorbic acid	6-2b, SSRL, Fe K-edge (7.11 keV)	418 μm horizontal	Single-shot, 45 min	<1 ms	<1 ms	157 ms Huyke <i>et al.</i> (2021) <sup>176</sup>
XANES/EXAFS and SAXS	Silicon, glass (Pyrex)	Photolithography, deep reactive ion etching, anodic bonding	XAS: silicon, ~50 μm	XAS: fluorescence, ~382 μm	Pb NPs	XAS: X18B, NSLS, and 10-ID-B, APS, Pd mm, K-edge (24.35 keV)	X18B, 0.2 mm × 3 mm × 3 mm	Multiframe, 5 × 20 min	Unknown 30 s	95 min	Karim <i>et al.</i> (2015) <sup>177</sup>

Table 2 (continued)

X-ray technique(s)	Device material(s)	Fabrication and/or assembly method	Window material, thickness	Mode, beam pathlength	Sample(s) investigated	Beamline, source, x-ray energy	Beam size	Acquisition mode, exposure time	Mixing time, $t_{mix}$	Minimum time step, $t_{step}$	Total residence time	Ref.
XANES/EXAFS and anomalous SAXS	PEEK, Kapton (gold-coated)	Machined, clamped	SAXS: silicon, ~50 $\mu$ m + second layer of unknown thickness	SAXS: transmission, ~270 $\mu$ m	SAXS: 12-ID-C, APS, 18 keV and 12-ID-B, APS, 12 keV	SAXS: 12-ID-C, APS, 18 keV and 12-ID-B, APS, 12 keV	SAXS: unknown	N/A	N/A	N/A	N/A	Binninger <i>et al.</i> (2016) <sup>178</sup>
XANES and SAXS	OSTEMER 322, Kapton	Photolithography, PDMS injection molding, cured, cure-bonded	Kapton, 2 $\times$ 50 $\mu$ m	Transmission, 10–50 $\mu$ m of catalyst, 2 mm of electrolyte	Pt/IrO <sub>2</sub> –IrO <sub>2</sub> electrocatalyst, HClO <sub>4</sub> electrolyte	SAXS: SuperXAS, SLS, Ir L <sub>3</sub> -edge (11.22 keV)	XAS: 100 $\mu$ m $\times$ 100 $\mu$ m	XAS: multiframe, 120 $\times$ 500 ms	<0.3 ms	~100 ms	XAS: 30 s	Ramamoorthy <i>et al.</i> (2024) <sup>179</sup>
XPCS	Aluminum, Kapton Quartz capillary tube	Machining, clamping, Compression fittings	Kapton, 2 $\times$ unknown	Transmission, 1 mm	Transmission, 0.98 mm	SAXS: 11.56 keV	XAS: 20 $\mu$ m $\times$ 20 $\mu$ m	XAS: unknown	<0.3 ms	~100 ms	XAS: 30 s	Ramamoorthy <i>et al.</i> (2024) <sup>179</sup>
XPCS	Kapton tube	Compression fittings	Kapton tube, 100 $\mu$ m wall	Transmission, 1.32 mm	Transmission, SiO <sub>2</sub> NPs	SAXS: 11.5 keV	CSAXS, SLS, 10 $\mu$ m $\times$ 10 $\mu$ m	SAXS: unknown	N/A	N/A	N/A	Busch <i>et al.</i> (2008) <sup>180</sup>
XPCS	NOA 81, polystyrene	Photolithography, soft lithography, UV cutting, cure-bonding	Polystyrene, 2 $\times$ 50 $\mu$ m	Transmission, 200 $\mu$ m	Transmission, SiO <sub>2</sub> NPs	SAXS: 11.5 keV	CSAXS, SLS, 10 $\mu$ m $\times$ 10 $\mu$ m	SAXS: unknown	N/A	N/A	N/A	Fluerasu <i>et al.</i> (2010) <sup>181</sup>
Heterodyne XPCS	Copper, Kapton	Machining, epoxy, clamping	Kapton, 2 $\times$ unknown	Transmission, 0.69 or 0.8 mm	Transmission, SiO <sub>2</sub> NPs	SAXS: 11.5 keV	8-ID-1, APS, 5 $\mu$ m $\times$ 20 $\mu$ m	Multiframe, unknown $\times$	N/A	N/A	N/A	Fluerasu <i>et al.</i> (2010) <sup>182</sup>
Heterodyne XPCS and XAM	PEEK, stainless steel	Compression fittings, epoxy	PEEK, 2 $\times$ 2 mm	Transmission, 1 mm	Transmission, Li/PEO-LiTFSI/Li battery cell	SAXS: 11 keV	8-ID-1, APS, 15 $\mu$ m $\times$ 15 $\mu$ m	Multiframe, 6000 $\times$ 60 ms	N/A	N/A	N/A	Fluerasu <i>et al.</i> (2016) <sup>183</sup>
						SAXS: 8.1 keV	ID10, ESRF, 10 $\mu$ m $\times$ 15 $\mu$ m	Unknown				Steinrück <i>et al.</i> (2020) <sup>185</sup>



Table 2 (continued)

X-ray technique(s)	Device material(s)	Fabrication and/or assembly method	Window material, thickness	Mode, beam pathlength	Sample(s) investigated	Beamline, source, x-ray energy	Beam size	Acquisition mode, exposure time	Mixing time, $t_{mix}$	Minimum time step, $t_{step}$	Total residence time	Ref.
SP-XPXCS, XPXP, SAXS, WAXS	Ti-6Al-4V alloy, diamond (type IIa)	Machining, epoxy, clamping, Poulter seal	Diamond, 2 × 100 μm	Transmission, ~0.4–1 mm	Supercritical $\text{H}_2\text{O}$	SP-XPXCS: ICLS, 9.5 keV	3 μm diameter	SP-XPXCS: multiframe, 10 <sup>5</sup> × 8.33 ms	N/A	N/A	N/A	Muhunthan <i>et al.</i> (2024) <sup>186</sup>

fast flow rates, and use of a microfocused X-ray beam. Similarly, Hofmann *et al.*<sup>157</sup> and Tofighi *et al.*<sup>158</sup> used a silicon-glass microfluidic device to study the synthesis of Au nanoparticles by fluorescence-based XANES at the Au L<sub>3</sub>-edge (11.92 keV). By utilizing on-chip turbulent cyclone mixers with <2 ms mixing time, the authors were able to gain access to early stages of the synthesis after only 1–2 ms of dead time.

More recently, Micheal Raj *et al.* reported a silicon-glass type microfluidic device for performing both fluorescence and transmission mode XANES and EXAFS.<sup>159</sup> They validated their device by studying Fe, Pb, and Br salt solutions and evaluating the quality of fluorescence *vs.* transmission mode data collected at different ionic concentrations between 1 mM and 1 M (Fig. 6b). Good quality data were obtained for Pb and Br solutions at the Pb L<sub>3</sub>-edge (13.04 keV) and Br K-edge (13.47 keV), however, the thick glass windows of the device (~500 μm) resulted in strong attenuation at the Fe K-edge (7.11 keV), preventing further analysis. For Pb and Br, fluorescence detection performed better at concentrations of 1 mM, transmission better at 1 M, and both performed similarly at intermediate concentrations. The authors also paid particular attention to the world-to-chip connections of their device by designing a 3D-printed sample holder that enabled reproducible and safe mounting at the beamline. Britto *et al.* used a commercial microfluidic device for an *operando* XANES/EXAFS study of the synthesis of Pt NPs in fluorescence mode.<sup>160</sup> Their device had a long channel length, and by tuning the flow rates, the authors were able to study the synthesis over reaction times from a few seconds to almost 40 minutes. Using multivariate analysis of the data, they were able to identify two intermediate phases that formed during the conversion of the H<sub>2</sub>PtCl<sub>6</sub> precursor into metallic Pt.

Several polymer-based microfluidic devices have also been reported for XAS analysis at hard X-ray energies. For example, Zinoveva *et al.* utilized a PMMA microfluidic chip to study the synthesis of Co nanoparticles by fluorescence mode XANES at the Co K-edge (7.78 keV).<sup>161</sup> Similarly, Oyanagi *et al.* studied the nucleation and growth of CdSe nanoparticles using fluorescence mode XANES and EXAFS at the Se K-edge.<sup>162</sup> Their device consisted of two components: a microfluidic continuous flow mixer and a separate module comprising a Kapton capillary tube and a resistive heating element for studying reactions under high temperatures. Here, the combination of XANES and EXAFS enabled the modeling of the XANES data with multi-scattering calculations and comparison to EXAFS data in order to estimate the kinetics of Se–Cd bond formation. Monnier *et al.* developed a microfluidic electrochemical cell made from polyvinyl chloride (PVC) and brass for *operando* analysis of the reduction and oxidation of different iron-containing phases.<sup>163,164</sup> They performed XANES and EXAFS at the Fe K-edge using both transmission and fluorescence read-out in order to study the corrosion of archeological samples and materials for the storage of nuclear waste.

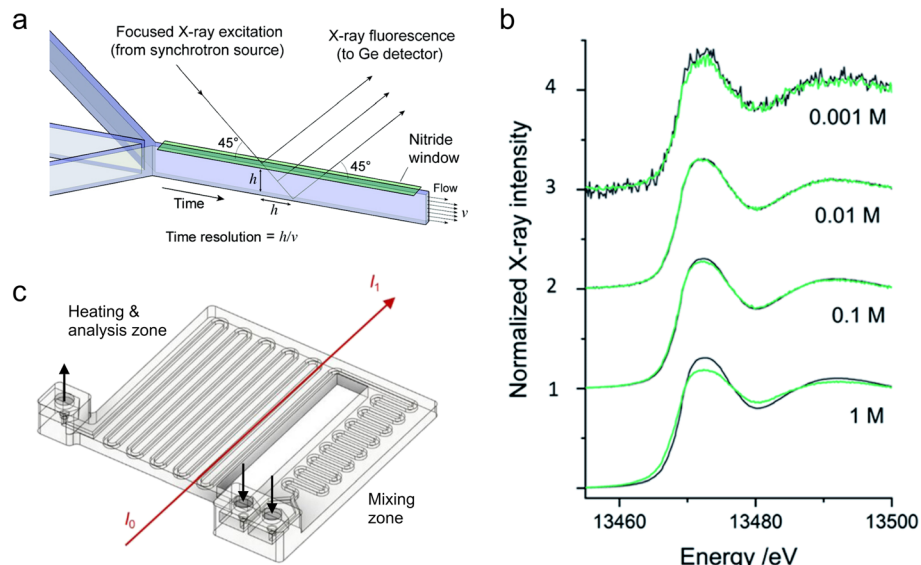


**Fig. 6** Devices for hard XAS analysis. (a) Design of a microfluidic device with a silicon nitride window for XAS in fluorescence mode (adapted with permission from Chan *et al.*, 2007; Copyright 2007 American Chemical Society).<sup>156</sup> (b) Br K-edge XANES spectra of aqueous NaBr solutions at the indicated molar concentrations. The dark grey curves are from transmission detection and the green curves are from fluorescence detection (adapted with permission from Micheal Raj *et al.*, 2021; Royal Society of Chemistry).<sup>159</sup> (c) Design of a 3D-printed millifluidic device for XAS in transmission mode (adapted with permission from Dobrovolskaya *et al.*, 2023; Copyright 2023 American Chemical Society).<sup>166</sup>

**4.2.2 Sensitivity considerations.** One problem in early microfluidic XAS, and especially EXAFS, was low sensitivity to dilute species—even in fluorescence mode—because of the short beam path through the solution. This often results in total scan times nearing or exceeding one hour to obtain sufficient signal-to-noise ratio. Attempts have been made to solve this problem in different ways. For example, Krishna *et al.* utilized a commercial polyester (PET) millifluidic device with wider channels to obtain a higher fluorescence yield.<sup>165</sup> The authors then employed this device to study the growth of nanostructured Au catalysts by XANES and EXAFS at the Au L<sub>3</sub>-edge. Alternatively, Dobrovolskaya *et al.* developed a 3D-printed millifluidic device for transmission-based XAS studies (Fig. 6c).<sup>166</sup> An 80 mm pathlength was obtained by illuminating along straight sections of a serpentine flow channel rather than across the shortest dimension of the channel as is standard practice. Such long pathlengths combined with highly penetrating X-rays at the Pd K-edge (24.35 keV) allowed the authors to perform *operando* XANES and EXAFS of the formation of Pd nanoparticles with scan times of only 10 min at a second-generation synchrotron. However, averaging the signal along 80 mm of the flow channel significantly limited the potential time resolution of the device.

**4.2.3 Soft X-rays.** Researchers have also explored performing microfluidic XAS in the soft and tender X-ray regime, where transmission is lowered and increased interaction between the beam and device materials must be taken into account. To our knowledge, the first such example comes from Fulton *et al.*, who modified the high-pressure cell of Hoffman *et al.*<sup>153</sup> with thinner windows and a shorter beam pathlength.<sup>167</sup> This enabled them to use the device

down into the tender X-ray regime in transmission mode, but not to lower energies. Subsequently, Fuchs *et al.* reported a lower pressure flow cell made from PTFE.<sup>168</sup> This cell was sealed by either a top silicon nitride (Si<sub>x</sub>N<sub>y</sub>) or silicon carbide membrane designed for fluorescence read-out of XAS data in the soft X-ray regime. They also performed X-ray emission spectroscopy (XES), which is equivalent to XRF with higher energy resolution. Nagasaka *et al.* utilized a flow-cell comprising Si<sub>x</sub>N<sub>y</sub> windows to perform transmission XANES measurements of liquid water at the O K-edge (532 eV).<sup>169</sup> Performing such low energy XAS in transmission mode was made possible by keeping the fluid layer <1 μm by controlling the spacing of the silicon nitride membranes. Schreck *et al.* developed a similar flow-cell and used it to study not only pure water, but also solutions of CoCl<sub>2</sub> and water-ethanol mixtures.<sup>170</sup>

More recently, Probst *et al.* utilized a PDMS-based droplet microfluidic device with a Si<sub>x</sub>N<sub>y</sub> window to study the crystallization of CaCO<sub>3</sub>.<sup>171</sup> They monitored the precipitation of amorphous calcium carbonation (ACC) over the first few seconds of the reaction by fluorescent XANES at the Ca K-edge (4.04 keV). However, owing to the background from the oil phase and the small droplet volumes, long scan times were required at each device position to obtain good photon counting statistics (>1 h). Additionally, the tender incident X-rays produced discolorations in the PDMS layer of the device, although the device shape and flow behavior were unaffected. Similarly, Brenker *et al.* utilized PDMS- and silicon-based droplet microfluidic devices with Si<sub>x</sub>N<sub>y</sub> windows for fluorescence mode XANES at the Ca K-edge and found that the silicon devices were more resilient to the incident



beam.<sup>172</sup> The authors also used the Ca K $\alpha$  line fluorescence yield to distinguish between droplets and the oil phase and isolate spectra from droplets. Despite this, the low total fluorescence yield still required the averaging of several long scans to obtain a good signal-to-noise ratio ( $>1$  h), which demands highly stable device operation over long durations and large sample volumes.

**4.2.4 Multi-technique analysis.** Finally, a large focus of research has been in developing single devices that could support not only XAS analysis, but also accommodate other X-ray methods or simultaneous acquisition of non-X-ray data. In these cases, an extra layer of difficulty is in selecting a window material that works for different techniques or having multiple analysis windows made of different materials. For example, Chiarello *et al.* developed a millifluidic gas flow-cell to support simultaneous transmission mode XAS and diffuse reflectance infrared Fourier transform spectroscopy (DRIFTS) on catalyst powder beds (Fig. 7a).<sup>173</sup> Since most IR transparent windows are made of crystalline materials that introduce diffraction artefacts in XAS spectra, the authors drilled a hole in their CaF<sub>2</sub> window and infilled it with an amorphous carbon glue to facilitate transmission of the X-ray beam (Fig. 7b).

Conversely, Dann *et al.* designed an aluminum XAS/DRIFTS reactor with a separate CaF<sub>2</sub> window for conducting IR analysis and used it to study a Pd-Al<sub>2</sub>O<sub>3</sub> catalyst operating at high temperature.<sup>174</sup> A polychromatic X-ray beam passed

directly through a thinned section of the Al reactor, where it was used to perform energy dispersive XANES and EXAFS at the Pb K-edge and collect full spectra in only 4.8 ms (for XANES). The gas effluent at the outlet of their device was also directed towards an instrument for performing simultaneous mass spectrometry (MS). Similarly, Venezia *et al.* developed a silicon-glass millifluidic chip for XAS/DRIFTS/MS analysis that had separate thin silicon windows for the X-ray and IR beams, respectively.<sup>175</sup> They also studied the operation of a Pd-Al<sub>2</sub>O<sub>3</sub> catalyst and its performance in two separate reactions. Huyke *et al.* developed a microfluidic device for performing XAS and XES.<sup>176</sup> Their device consisted of a fused silica hydrodynamic flow focusing mixer connected to a Kapton capillary for X-ray analysis. The authors used it to study the reduction of ferricyanide by ascorbic acid with millisecond time resolution.

Several devices have also been designed to support both XAS and SAXS analysis. For example, Karim *et al.* studied the synthesis of Pd nanoparticles in a silicon-glass microfluidic device with SAXS and fluorescence mode XANES/EXAFS at the Pd K-edge.<sup>177</sup> For SAXS analysis, the glass layer was replaced by another Si layer to lower background scattering. Binninger *et al.* also performed XAS and SAXS with a millifluidic electrochemical flow cell.<sup>178</sup> Their device was made from a polyether ether ketone (PEEK) housing that held two electrically conductive Kapton films to serve as both the X-ray windows and electrodes. Using this device, they

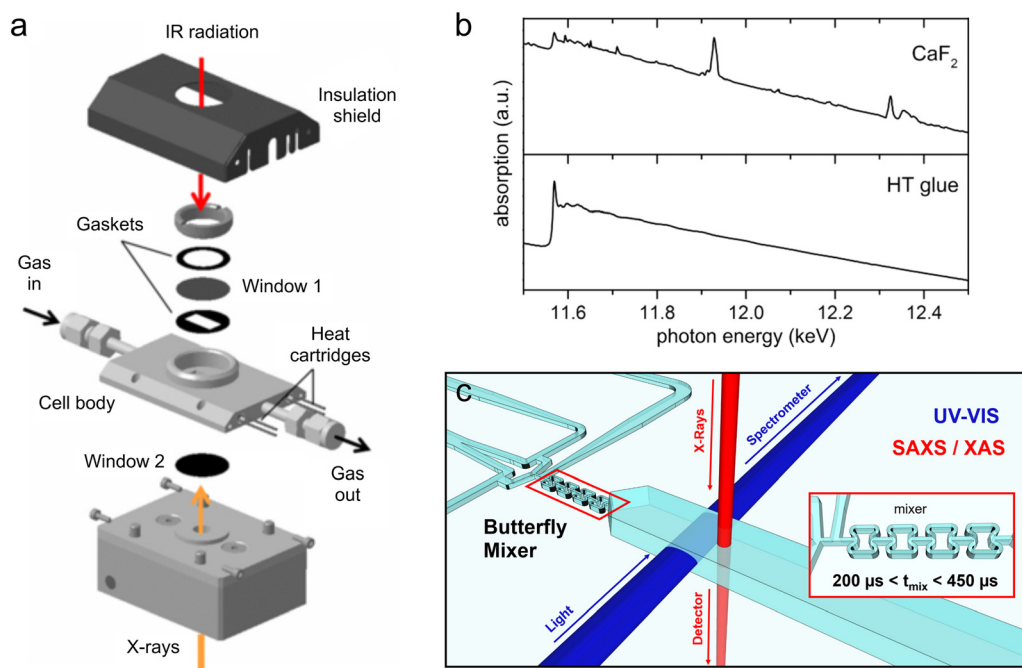


**Fig. 7** Hybrid devices for XAS and other techniques. (a) Exploded view of a millifluidic gas flow-cell for transmission mode XAS and simultaneous IR spectroscopy (adapted from Chiarello *et al.* 2014 with the permission of AIP Publishing).<sup>173</sup> (b) EXAFS spectra of a Pt/Al<sub>2</sub>O<sub>3</sub> catalyst obtained from the device in (a) with CaF<sub>2</sub> windows (top) and CaF<sub>2</sub> windows comprising a high temperature (HT) carbon glue bypass for X-ray transmission (bottom). Diffraction from the crystalline CaF<sub>2</sub> window produces artefacts in the EXAFS data, which are eliminated by using the HT glue bypass (adapted from Chiarello *et al.* 2014 with the permission of AIP Publishing).<sup>173</sup> (c) Conceptual design of an ultra-fast mixing device for XAS/SAXS/UV-vis analysis of nanoparticle synthesis. The inset shows the design of the butterfly mixing element (adapted with permission from Ramamoorthy *et al.*, 2024; Royal Society of Chemistry).<sup>179</sup>



performed Ir L<sub>3</sub>-edge (11.22 keV) transmission mode XANES/EXAFS to follow the oxidation state of a mixed Pt/IrO<sub>2</sub>–TiO<sub>2</sub> electrocatalyst as a function of the applied electric potential. In turn, anomalous SAXS was used to follow the degradation of the Pt cathode, where performing SAXS at energies near the Pt L<sub>3</sub>-edge enabled isolation of the scattering from the Pt nanoparticles from that of the IrO<sub>2</sub>–TiO<sub>2</sub> support. Recently, Ramamoorthy *et al.* demonstrated an ultra-fast microfluidic mixer for performing XAS, SAXS, and UV-vis analysis with dead times as low as 200  $\mu$ s (Fig. 7c).<sup>179</sup> They used the OSTEMER and Kapton-based device to study the nucleation and growth of Au NPs with transmission mode XANES at the Au L<sub>3</sub>-edge. With the aid of these three complementary techniques, the authors revealed the formation of transient pre-nucleation clusters and Au(i) lamellar phases prior to the nucleation of Au(0) nanoparticles. Notably, the authors performed both continuous and stopped-flow analysis on-chip to access shorter and longer reaction times, respectively.

#### 4.3 XPCS

X-ray photon correlation spectroscopy (XPCS) has also received some attention in continuous flow micro- and millifluidic devices. XPCS is not a true spectroscopy technique based on the measurement of light transmission as a function of wavelength, but rather it is a time spectroscopy.<sup>187</sup> Intensity fluctuations, or so-called “speckles”, appearing in X-ray scattering patterns collected over time using coherent X-ray radiation are temporally correlated to extract information on the physical dynamics of a sample, such as related to diffusive or advective motion.<sup>182</sup> More simply, the technique is an extension of Dynamic Light Scattering (DLS) into the X-ray regime, where it is useful for analyzing thicker, more turbid samples at smaller spatial scales.<sup>188</sup>

The technique was first performed in flow by Fluerasu and co-workers, who used a simple millifluidic capillary cell to determine the diffusive dynamics of PMMA and latex nanoparticle suspensions.<sup>180,181</sup> The authors found that scattering in the direction of the wavevector,  $q$ , perpendicular to the flow was insensitive to the advective component of particle motion at low shear rates (“transverse flow geometry”), whereas scattering in the direction parallel to the flow was strongly affected by advection (“longitudinal flow geometry”; Fig. 8). They thus exploited the transverse flow scattering to isolate the thermal motion of the particles and extract diffusion constants. Later, Fluerasu *et al.* followed up their work by using both the transverse and longitudinal scattering to study the diffusive and advective dynamics of a flow of silica nanoparticles.<sup>182</sup> Transverse flow scattering data were used to deconvolute the longitudinal scattering data collected from different radial positions along the cross-section of the flow tube in order to calculate the shear relaxation rate. The rates calculated at each position matched well with a Poiseuille model of the flow.

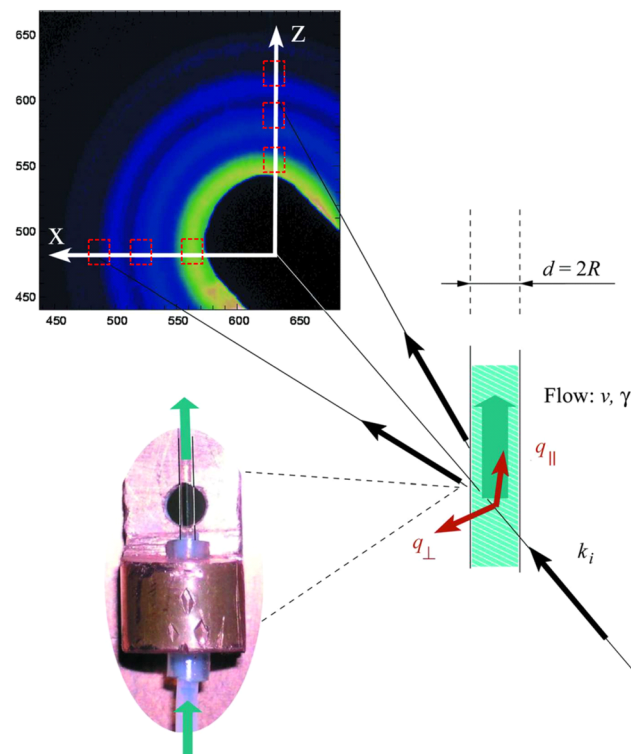


Fig. 8 An example of an XPCS flow experiment. Scattering of the incident beam ( $k_i$ ) in the longitudinal ( $q_{||}$ ) and transverse ( $q_{\perp}$ ) directions by fluid flowing within the capillary is obtained from averaging of the regions within the dotted lines along the Z and X axes of the area detector, respectively. The photo shows the simple capillary setup of Fluerasu *et al.* (2008). Adapted with permission of the International Union of Crystallography.<sup>181</sup>

More recently, Urbani *et al.* further miniaturized this technology using a microfluidic chip and a microfocused X-ray beam.<sup>183</sup> They mapped the advective dynamics at different channel positions along the chip, including straight and curved sections and a Venturi flow constriction. Flow velocities at the constriction calculated from XPCS data were compared to a CFD model with relatively good agreement, however some deviations were observed, especially at the center of the constriction where velocities were the highest. Lhermitte *et al.* improved the ability to calculate absolute flow velocities from XPCS data by performing heterodyne analysis, *i.e.*, collecting scattering from the dynamic sample and a static reference material simultaneously.<sup>184</sup> This heterodyne XPCS technique was subsequently utilized by Steinrück *et al.* to measure ion transport within the polymer electrolyte of a lithium-ion battery cell.<sup>185</sup> Finally, Muhunthan *et al.* recently demonstrated a millifluidic flow-cell for performing split-pulse XPCS (sp-XPCS), X-ray pump X-ray probe (XPXP), and SAXS/WAXS measurements under extreme conditions at both synchrotrons and XFELs.<sup>186</sup> The cell was constructed from titanium alloy with diamond windows and validated by obtaining speckle patterns from supercritical H<sub>2</sub>O at 380 °C and 25 MPa.



# 5 Devices for X-ray imaging

## 5.1 Brief theory and overview

The field of X-ray imaging comprises a wide variety of techniques that can provide morphological and chemical information on extended samples. These techniques can be divided broadly into two categories: full-field and scanning.<sup>189</sup> Full-field techniques make use of an X-ray beam that irradiates an entire sample or region of interest in transmission mode. Conversely, with a scanning technique, a sample is irradiated by a small X-ray beam in a 2D raster pattern, and the image is constructed as a mosaic of the data collected at each position.<sup>189,190</sup> Contrast in the image is obtained by recording the absorption or phase shift of X-rays by the sample using a 2D detector. Both of these quantities are related to a material's complex refractive index,  $n$ :

$$n = 1 - \delta + i\beta \quad (3)$$

where  $\delta$  is the real phase and  $\beta$  is the imaginary absorption of the sample material.<sup>191</sup> Importantly,  $\beta$  is related to the linear absorption coefficient ( $\mu$ ) of the material, and thus, similar to XAS, X-ray imaging can be used to probe the chemical state of the sample by varying the wavelength of the incident beam (see eqn (2)).<sup>189</sup> For obtaining contrast between soft materials or materials of similar densities, it is often necessary to probe the phase shift or utilize X-ray energies at an absorption edge of a target element.

With a scanning technique, data can be collected using different geometries and may be composed of single-wavelength absorption contrast measurements, or more commonly, of measurements collected at multiple wavelengths. Scanning instruments making use of other types of detection are also possible and can be used to construct, for example, fluorescence, scattering, or diffraction "maps". Most techniques can also be made 3D by collecting 2D data (called "projections") from multiple orientations of a sample under rotation and reconstructing the 3D volume using tomographic algorithms.<sup>192</sup>

In science and engineering applications, full-field X-ray imaging techniques relying on either phase-shift or absorption contrast are collectively referred to as full-field transmission X-ray microscopy (TXM), while scanning techniques are collectively referred to as scanning transmission X-ray microscopy (STXM). In both cases, the maximum spatial resolution is about 20–50 nm, mainly determined by the imaging zone plate in TXM, and by the focusing zone plate (which dictates the minimum raster step) in STXM. This resolution may be degraded in liquid though, in particular due to Brownian motion.

Owing to the wide variety of specific imaging techniques, this section will be organized by the type and application of the micro/millifluidic device rather than by the specific measurement technique as in the previous two sections. In fact, despite the number of beamlines and devices utilized, most studies have been conducted using similar device styles

for similar applications. Specifically, the majority of papers report either thin microfluidic devices for performing TXM and STXM, often for electrochemistry applications, or larger millifluidic flow cells for performing tomographic studies of fluid flow and geochemistry within porous media. More details on all the papers reviewed below can be found in Table 3.

## 5.2 Devices for STXM and TXM

**5.2.1 Early work (static cells).** Microfluidic STXM began in the early 1990s for the study of cells and subcellular structures,<sup>231,232</sup> and these first studies influenced the design of most subsequent devices for both TXM and STXM. Both techniques are often performed at soft X-ray energies (<2 keV) at which beam pathlengths of more than a few microns through water result in significant attenuation. Therefore, microfluidic devices comprising ultrathin silicon nitride ( $\text{Si}_x\text{N}_y$ ) windows spaced just a few microns apart are ideally suited for performing *in situ* TXM and STXM experiments (Fig. 9a). While these types of devices are very thin, the window width is normally on the order of a millimeter, allowing large regions of the flow to be imaged. To our knowledge, microfluidic studies of hard condensed matter samples were not reported until a few years later in the year 2000. For example, Neuhausler *et al.* studied static samples of clay aggregates<sup>193</sup> within a similar  $\text{Si}/\text{Si}_x\text{N}_y$  wafer-based device and Rieger *et al.* studied the crystallization of  $\text{CaCO}_3$  from pre-mixed solutions using a device with  $\text{Si}/\text{SiO}_2$ -coated polyimide windows.<sup>194</sup> Subsequently, Guay *et al.* upgraded the basic silicon chip design by patterning Au electrodes over the  $\text{Si}_x\text{N}_y$  windows to enable electrochemical measurements and time-lapse imaging of samples under electrical stimulus.<sup>195</sup> Many similar static electrochemical cells for TXM/STXM were developed over the succeeding years and more information on these can be found in earlier reviews.<sup>233,234</sup>

**5.2.2 Gas flow cells.** The first flow reactor for *in situ* STXM was developed by Drake *et al.* to study catalysts under controlled gaseous environments at high temperatures.<sup>196</sup> Their reactor had ultrathin  $\text{Si}_x\text{N}_y$  windows coated with a patterned aluminum thin film to provide local resistive heating. The channels of the device were fabricated from glass and PDMS and had a total depth of 0.8 mm, a beam pathlength made possible by the lower attenuation coefficient of gases compared to liquids. The authors studied the oxidation and reduction of a Cu catalyst at temperatures up to 260 °C in CO/He atmospheres using spectro-STXM, *i.e.*, spatially resolved XANES. By obtaining a series of STXM images at energies between 926 eV and 937 eV, where the Cu L<sub>3</sub>-edge is located, the authors could monitor the relative presence of Cu(i) and Cu(ii) within the catalyst particles. Huthwelker *et al.* developed a gas-cell for spectro-STXM that they used to monitor aerosol particles and environmental contaminants under gases with different relative humidities.<sup>197</sup> Notably, their device comprised two parts that



Table 3 Micro- and milli-fluidic devices for X-ray imaging

X-ray technique(s)	Device type	Device material(s)	Fabrication and/or assembly method	Window material, thickness	Geometry, beam pathlength	Sample(s) investigated	Conditions	Beamline, source, X-ray energy	Beam size/ resolution	Acquisition mode and exposure time	Ref.
STXM and XANES	Microfluidic static cell	Silicon	Clamping	Silicon nitride, 2 × 100 nm	Transmission, ~3 µm	Clay	Ambient temperature & pressure	X1-A, NSLS, C K-edge (283.8 eV)	Unknown	Unknown	Neuhauser <i>et al.</i> (2000) <sup>193</sup>
TXM	Microfluidic static cell	Polyimide, silicon	Clamping	Si/Si <sub>x</sub> N <sub>y</sub> -coated polyimide, 2 × 150 nm	Transmission, ~10 µm	CaCO <sub>3</sub>	Ambient temperature & pressure	IPR, BESSY I, "water window" between 282–533 eV	~40 nm resolution	Multiframe, 2–10 s per exposure	Rieger <i>et al.</i> (2000) <sup>194</sup>
Spectro-STXM and XANES	Microfluidic electro-chemical cell	Silicon, poly(chloro-trifluoroethyl)-ene)	Epoxy, vacuum grease	Silicon nitride, 2 × 75 nm	Transmission, ~1 µm	Polyaniline thin film	Ambient temperature & pressure	5.3.2, ALS, C K-edge (283.8 eV) and N K-edge (401.6 eV)	~50 nm resolution	Unknown, <60 s	Guay <i>et al.</i> (2005) <sup>195</sup>
Spectro-STXM	Millifluidic gas flow cell	Silicon, PDMS, glass	Photolithography, wet etching, plasma etching, sputter coating, micromachining, plasma bonding, adhesive	Silicon nitride, 2 × 100 nm	Transmission, 0.8 mm	Cu catalyst	260 °C, ambient pressure	11.0.2, ALS, Cu L <sub>3</sub> -edge (931.1 eV)	~40–100 nm resolution	Multiframe, ~12 s per image per energy, full spectra in ~15 min	Drake <i>et al.</i> (2004) <sup>196</sup>
Spectro-STXM	Microfluidic gas flow cell	Silicon, aluminum, stainless steel, viton	Machining, clamping, glue/wax	Silicon nitride, 2 × 50 nm	Transmission, ~200 µm	NaBr and diesel soot	5–27 °C, ambient pressure	Pollux, SLS, O K-edge (532 eV)	30–40 nm beam spot	Unknown	Huthwelker <i>et al.</i> (2010) <sup>197</sup>
Spectro-STXM	Microfluidic gas flow cell	Silicon, PEEK or aluminum, viton, PTFE	Machining, clamping, epoxy	Silicon nitride, 2 × unknown	Transmission, ~0.5–1.5 mm	Ammonium sulfate	Ambient temperature & pressure	11.0.2 and 5.3.2.2, ALS, O K-edge (532 eV)	25 nm outer zone plate width	Multiframe, ~1 ms per pixel	Zelenay <i>et al.</i> (2011) <sup>198</sup>
Spectro-STXM	Microfluidic gas flow cell	Silicon, glass, brass, viton	Machining, microfabrication, clamping	Silicon nitride, 2 × 10 nm	Transmission, ~4 µm	Fe-based FTS catalyst	25–350 °C, ambient pressure	11.0.2, ALS, C K-edge (283.8 eV), O K-edge (532 eV), and Fe L <sub>3</sub> - and L <sub>2</sub> -edges (708.1 and 721.1 eV)	~40 nm resolution	Unknown	Kelly <i>et al.</i> (2013) <sup>199</sup>
Spectro-STXM	Microfluidic gas flow cell	Silicon, glass, brass, viton	Machining, microfabrication, clamping	Silicon nitride, 2 × 10 nm	Transmission, ~50 µm	Fe-based FTS catalyst	25–500 °C, ambient pressure	10ID1, CLS, O K-edge (532 eV), and Fe L <sub>3</sub> and L <sub>2</sub> -edges (708.1 and 721.1 eV)	~40 nm resolution	Unknown	de Smit <i>et al.</i> (2008) <sup>200</sup>
Spectro-STXM	Microfluidic gas/liquid flow cell	Silicon, fluoropolymer O-ring	Photolithography, reactive ion etching, chemical vapor deposition, wet etching, E-beam evaporation, clamping	Silicon nitride, 2 × 50 nm	Transmission, ~500 nm	Ce <sub>x</sub> TiO <sub>3</sub> -supported Pt catalyst	140 °C, ambient pressure	~55 nm resolution	Multiframe, 0.1–2 ms per pixel	Yoo <i>et al.</i> (2020) <sup>202</sup>	

Table 3 (continued)

X-ray technique(s)	Device type	Device material(s)	Fabrication and/or assembly method	Window material, thickness	Geometry, beam pathlength	Sample(s) investigated	Conditions	Beamline, source, X-ray energy	Beam size/ resolution	Acquisition mode and exposure time	Ref.
TXM	Microfluidic continuous flow cell	Silicon, stainless steel, unknown O-ring material	Machining, clamping, glue	Silicon nitride, 2 × 100 nm	Transmission, unknown	Ag nanowires reacting with Au	Ambient temperature & pressure	~25 nm resolution	Multiframe, 0.5 Hz	Sun and Wang (2011) <sup>203</sup>	
Spectro-STXM and μXAS	Microfluidic electro-chemical cell	Silicon, SU-8, NOA 84	Photolithography, UV curing	Silicon nitride, 2 × Unknown	Transmission, unknown	Co-polyppyrrole electrocatalyst	Ambient temperature & pressure	Unknown	Unknown	Bozzini <i>et al.</i> (2014) <sup>236</sup>	
Spectro-STXM	Microfluidic electro-chemical cell	Silicon, fluoropolymer O-ring	Photolithography, reactive ion etching, chemical vapor deposition, wet etching, E-beam evaporation, clamping	Silicon nitride, 2 × 75 nm	Transmission, ~1 μm	Li <sub>x</sub> FePO <sub>4</sub> crystals	Ambient temperature & pressure	50 nm beam spot	Multiframe, 1 ms per pixel	Lim <i>et al.</i> (2016) <sup>204</sup>	
Spectro-STXM	Microfluidic electro-chemical cell	Silicon, fluoropolymer O-ring	Photolithography, reactive ion etching, chemical vapor deposition, wet etching, E-beam evaporation, clamping	Silicon nitride, 2 × 100 nm	Transmission, ~1 μm	Co(OH <sub>2</sub> ) crystals	Ambient temperature & pressure	50 nm resolution	Multiframe, 2 ms per pixel + 2 ms delay, full spectra in ~30 min	Mefford <i>et al.</i> (2019) <sup>205</sup>	
Spectro-STXM	Microfluidic electro-chemical cell and microfluidic gas flow cell	Silicon, viton, unknown housing material	Machining, clamping, tape	Silicon nitride, 2 × 100 nm	Transmission, ~20 μm	FeSO <sub>4</sub> solution, polymer	Ambient temperature & pressure	~40–50 nm resolution	Unknown	Ohigashi <i>et al.</i> (2016) <sup>207</sup>	
Spectro-STXM	Microfluidic electro-chemical cell	Silicon, acrylic polymer resin, unknown O-ring material	3D printing, proprietary techniques, clamping	Silicon nitride, 2 × 50 nm	Transmission, ~1–1.5 μm	Cu deposition on Au electrode	Ambient temperature & pressure	~25 nm resolution	Multiframe, ~20 s per image	Prabu <i>et al.</i> (2018) <sup>208</sup>	
Spectro-STXM	Microfluidic continuous flow reactor	Silicon, PDMS, stainless steel	Machining, soft lithography, clamping	Silicon nitride, 2 × 50 nm	Transmission, 3 μm	CaCO <sub>3</sub> with polymer additive	Ambient temperature, ≤1 bar pressure drop	~43 nm resolution	Multiframe, ~5–50 ms per pixel, ~5–11 min per image	SOLEIL, 510 eV and Ca L <sub>3</sub> - and L <sub>2</sub> -edges (346.4 and 350 eV) HERMES, ~37–60 nm resolution	Gosse <i>et al.</i> (2020) <sup>89</sup>
X-ray PIV (2D)	Millifluidic continuous flow	PTFE tubing	Unknown	PTFE, unknown	Transmission, 750 μm	Alumina microspheres	Ambient temperature & pressure	12.3 μm resolution	Multiframe, 50 Hz	Lee and Kim (2003) <sup>209</sup>	

Table 3 (continued)

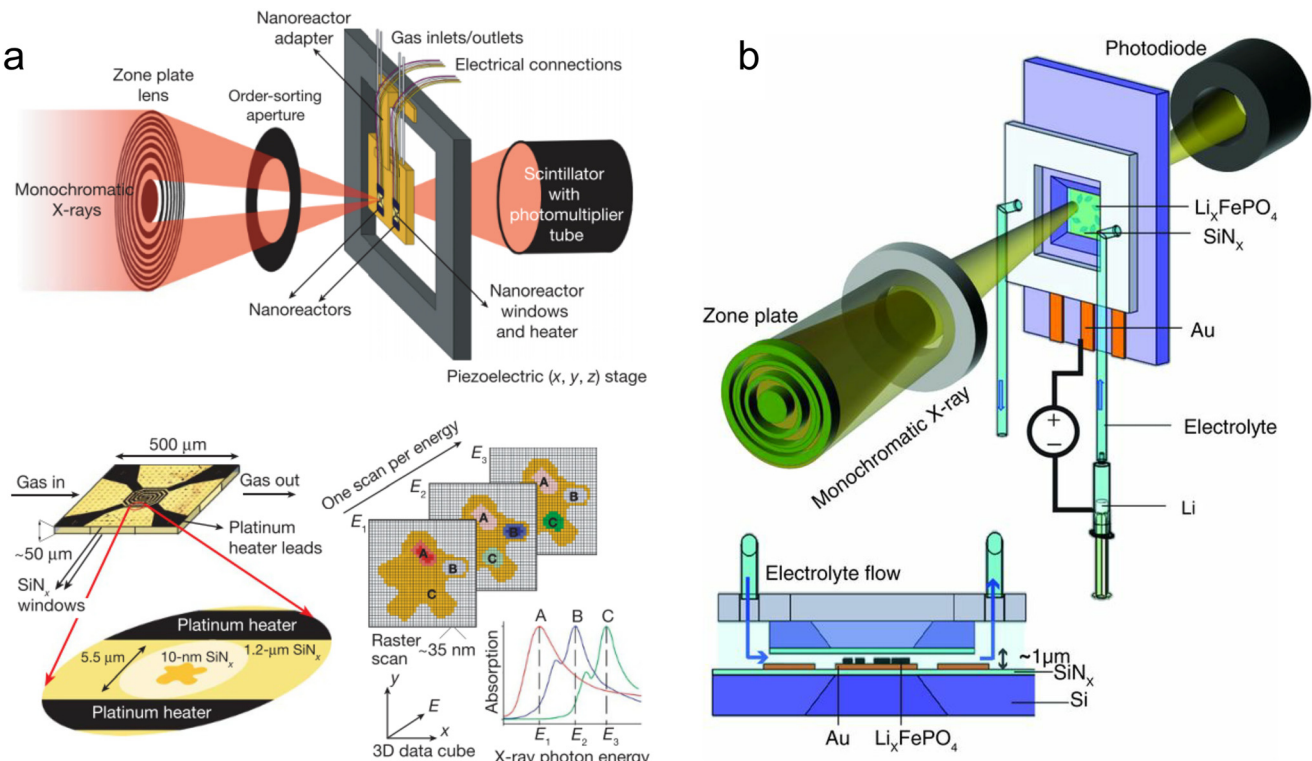
X-ray technique(s)	Device type	Device material(s)	Fabrication and/or assembly method	Window material, thickness	Geometry, beam pathlength	Sample(s) investigated	Conditions	Beamline, source, X-ray energy	Beam size/ resolution	Acquisition mode and exposure time	Ref.
X-ray PIV (3D)	Microfluidic continuous flow	Silicone tubing	Unknown	Silicone, unknown	Transmission, 490 $\mu$ m	Aluminum or solder microparticles	Ambient temperature & pressure	XOR-32-ID, APS, 18 keV	3.87 $\mu$ m pixel size	Multiframe, 60 Hz	Lee <i>et al.</i> (2011) <sup>210</sup>
$\mu$ CT	Millifluidic flow cell	Polyethylene, unknown	Unknown	Polyethylene, unknown	Transmission, 6.5 mm	Multiphase flow in porous polyethylene	Ambient temperature & pressure	X2B, NSLS, unknown	4.1 $\mu$ m voxel size	Multiframe, collection of tomograms after each injection	Prodanović <i>et al.</i> (2006) <sup>211</sup>
$\mu$ CT	Millifluidic flow cell	Silicone, PTFE, epoxy resin	Epoxy, compression fittings	Silicone and PTFE, unknown	Transmission, 9 mm	Carbonated salt solution in limestone core	Ambient temperature, 0-3 MPa pressure	ID19, ESRF, 40 keV	6 $\mu$ m resolution	Multiframe, collection of tomograms at six time points	Noiriel <i>et al.</i> (2007) <sup>212</sup>
Fast- $\mu$ CT	Millifluidic flow cell with integrated pumps	Polycarbonate, unknown	Unknown	Polycarbonate, unknown	Transmission, 4 mm	Multiphase flow in sandstone	Ambient temperature, <10 kPa	TOMCAT, SLS, 21.25 keV	3 $\mu$ m voxel size	Multiframe, 12 ms per projection, 16.8 s tomogram acquisition	Berg <i>et al.</i> (2013) <sup>213</sup>
Fast- $\mu$ CT	Millifluidic flow cell with integrated pumps	Unknown	Unknown	Unknown	Transmission, 4 mm	Multiphase flow in Robulglas	Ambient temperature, <10 kPa	TOMCAT, SLS, 36 keV	2.11 $\mu$ m pixel size	Multiframe, 40 ms per projection, continuous collection	Armstrong <i>et al.</i> (2014) <sup>214</sup>
Fast- $\mu$ CT	Millifluidic flow cell	PEEK	Compression fittings	PEEK, unknown	Transmission, 4.8 mm	Multiphase flow in glass bead column	Ambient temperature, 517.1 kPa	I22, diamond, unknown	3.25 $\mu$ m resolution	over 12 min	Hasan <i>et al.</i> (2020) <sup>215</sup>
Fast- $\mu$ CT	Millifluidic passive wicking cell	PMMA with organic binders	Powder-based 3D printing	No window	Transmission, 2 or 3.5 mm depending on the orientation	Water in porous microbead column	Ambient temperature & pressure	ID19, ESRF, 40 keV “pink beam”	1.1 $\mu$ m pixel size	Multiframe, 0.5 s tomogram acquisition	Piovesan <i>et al.</i> (2020) <sup>216</sup>
Fast- $\mu$ CT	Millifluidic gravity-feed flow cell	PMMA	Compression fittings	PMMA, unknown	Transmission, 6 and 25 mm	Multiphase flow in sandstone gravel column	Ambient temperature & pressure	I12, diamond, “white beam” between 50 and 150 keV or monochromatic beam of unknown energy	2.5 to 3.8 $\mu$ m voxel size	read-out time	Dobson <i>et al.</i> (2016) <sup>217</sup>
Tomographic X-ray PIV	Millifluidic high-pressure flow cell	Viton, PEEK	Compression fittings	Viton, unknown	Transmission, 4 mm	Multiphase flow containing silver-coated	Ambient temperature, 2 MPa	TOMCAT, SLS, glassy carbon and borosilicate	2.75 $\mu$ m voxel size	Multiframe, 0.5 ms per projection,	Bultreys <i>et al.</i> (2024) <sup>218</sup>

Table 3 (continued)

X-ray technique(s)	Device type	Device material(s)	Fabrication and/or assembly method	Window material, thickness	Geometry, beam pathlength	Sample(s) investigated	Conditions	Beamline, source, X-ray energy	Beam size/ resolution	Acquisition mode and exposure time	Ref.
μCT	(Hassler core holder)										
μCT	Microfluidic continuous flow mixer (Kenics mixer)	IPS resin	Two-photon stereolithography, UV curing, epoxy	IPS resin, unknown	Transmission, 200 μm		Ambient temperature & pressure	P05, PETRA III, 11 keV	P05: 1.14 μm voxel size	P05: 0.5 s tomogram acquisition	Koška <i>et al.</i> (2020) <sup>219</sup>
μCT	Millifluidic high pressure flow cell	Epoxy resin, other unknown materials	Compression fittings	Epoxy resin, unknown	Transmission, 9 mm		Ambient temperature, 0.13 MPa back pressure	ID19, ESRF, 40 keV	6 μm resolution	TOMCAT: 80 ns per projection	Noiriel <i>et al.</i> (2013) <sup>220</sup>
μCT	Millifluidic flow cell	Quartz tube	Sintering, compression fittings	Quartz, 1.4 mm wall	Transmission, 1.6 mm	BaSO <sub>4</sub> in microporous quartz column	Ambient temperature & pressure	13-ID-B, APS, 22 keV	1.24 μm voxel size	Multiframe, collection of tomograms at six time points every 24 min	Godinho <i>et al.</i> (2016) <sup>221</sup>
Fast-μCT	Millifluidic high-pressure flow cell (Hassler core holder)	Stainless steel, aluminum, steel wire, silicone, heatshrink tubing and O-rings of unknown material	Machining, compression fittings	Aluminum, silicone, shrink wrap, unknown	Transmission, 3 mm	Salt solution in olivine rock	200 °C, 10 MPa fluid pressure and 15 MPa confining pressure	2-BM, APS, 65 keV “pink beam”	1.47 μm pixel size	Multiframe, 10 ms exposure per projection, 20 s tomogram acquisition	Fusseis <i>et al.</i> (2014) <sup>222</sup>
X-ray laminography	Microfluidic packed-bed reactor	Silicon, glass (Pyrex)	Photolithography, wet etching, anodic bonding	Glass, unknown, silicon, unknown	Transmission, 30 μm	CaCO <sub>3</sub>	Ambient temperature & pressure	ID19, ESRF, 26 keV	0.7 μm resolution	Unknown	Morais <i>et al.</i> (2023) <sup>223</sup>
μCT	Millifluidic passive counter-diffusion cell	Tygon tubing, heatshrink tubing	Heat-shrinking	Heat-shrink tubing, unknown	Transmission, 3 mm	BaSO <sub>4</sub> in shale	Ambient temperature & pressure	I13-2, diamond, 27.6 keV “pink beam”	1.6 μm voxel size	Multiframe, 100 ms exposure per projection, 80 s tomogram acquisition	Godinho <i>et al.</i> (2019) <sup>224</sup>

Table 3 (continued)

X-ray technique(s)	Device type	Device material(s)	Fabrication and/or assembly method	Window material, thickness	Geometry, beam pathlength	Sample(s) investigated	Conditions	Beamline, source, X-ray energy	Beam size/ resolution	Acquisition mode and exposure time	Ref.
µCT and XRD-CT	Millifluidic passive counter-diffusion cell	Glass tubes, His-3 BAG heatshrink tubing, silicone tubing	Heat-shrinking	No window	Transmission, 2.8 mm	CaSO <sub>x</sub> H <sub>2</sub> O in CPG rod	Ambient temperature & pressure	µCT: 1132, diamond, unknown	µCT: 1.6 µm pixel size	µCT: multiframe, 100 ms exposure per projection, 80 s	Anduix-Canto <i>et al.</i> (2021) <sup>225</sup>
Scanning µXRF and XAS	Microfluidic continuous flow mixer	PDMS, silicon O-rings and holder of unknown materials	Soft lithography, machining, clamping, compression fittings	Silicon nitride, 100 nm	Fluorescence, 87.2 µm	Water and pyridine	Ambient temperature & pressure	BL3U, UVSOR-III, N K-edge (401.6 eV) and O K-edge (532 eV) LUCIA, Soleil, Fe K-edge (7.11 keV)	30 µm × 30 µm, beam size, 30–61 µm step size	Tomogram acquisition XRD-CT: single-shot, 1 s exposure per grid point	Nagasaki <i>et al.</i> (2019) <sup>226</sup>
Scanning µXRF, SAXS/WAXS, and XRD	Microfluidic continuous flow mixer (and others)	PDMS, Kapton, 3D-printed resin, O-ring of unknown materials	Soft lithography, plasma bonding, 3D printing, clamping, gluing, compression fittings	Kapton, 8 µm, PDMS, 30 µm	Fluorescence, >500 µm	Iron oxide NPs	Ambient temperature & pressure	3.5 µm × 3.5 µm beam size, 5 µm step size	Single-shot, 300 ms exposure per grid point	Chaussavoine <i>et al.</i> (2020) <sup>227</sup>	
Scanning µXRF and XAS	Microfluidic continuous flow cell	Silicon, AF-32 Eco glass	Photolithography, reactive ion etching, machining, plasma ashing, muffle furnace firing, epoxy, UV epoxy, compression fittings	Glass, 30 µm	Fluorescence, >30 µm	Fe-As-S geochemical reactions	Ambient temperature & pressure	4-BM, NSLS-II, 14 keV (for µXRF mapping)	5 µm × 5 µm beam size, 5–45 µm step size	Single-shot, 50–200 ms exposure per grid point	Chen and Kocar (2021) <sup>228</sup>
Scanning nano-XRF	Microfluidic electro-chemical cell	Glass, NOA, PET, PDMS	Photolithography, wet etching, sputter coating, machining, UV epoxy	Glass, ≤1 µm, PET, 12 µm	Fluorescence, ~20–50 µm	Electrodeposition of Ag/AgCl	Ambient temperature & pressure	Carnaúba, Sirius, 9.7–13.7 keV	600 nm × 600 nm beam size, 5 µm step size	Single-shot, 22.5 ms per grid point, 62 s for full map	Neckel <i>et al.</i> (2021) <sup>229</sup>
XFEL-CDI	Microfluidic continuous flow cell	Silicon, Kapton	Unknown	Silicon nitride, 2 × 200 nm	Transmission, 12 µm	Ag NPs	Ambient temperature, ambient to vacuum pressure	BL2, SACLIA, 4 keV	100 nm × 100 nm beam size	Single-shot, 10 fs	Matsumoto <i>et al.</i> (2022) <sup>230</sup>



**Fig. 9** Microfluidic devices for operando TXM/STXM. (a) A STXM setup with a MEMS gas nanoreactor for studying catalysis at high temperature (top). The inset shows a detailed illustration of the Pt electrode design and the  $\text{Si}_x\text{N}_y$  windows (bottom left) and an example of spectro-STXM data from a heterogeneous catalyst particle (bottom right) (reprinted with permission from de Smit *et al.* 2008; Copyright 2008 Springer Nature).<sup>200</sup> (b) An electrochemical STXM setup based on a Si/ $\text{Si}_x\text{N}_y$  chip for studying Li-ion battery particles. The inset shows the side view of the device and the  $\sim 1\ \mu\text{m}$  spacing between the  $\text{Si}_x\text{N}_y$  windows (from Lim *et al.*, 2016; reprinted with permission from AAAS).<sup>204</sup>

enabled ease of mounting and rapid sample exchange: a back piece containing the heating/cooling system, gas connections, and standard mounting fixtures and a front clip holding the sample. The device was then utilized for subsequent environmental studies of ammonium sulfate aerosols.<sup>198</sup> Kelly *et al.* designed a similar device comprising  $\text{Si}_x\text{N}_y$  windows and a body machined from either aluminum or PEEK.<sup>199</sup> However, they improved upon the design of Huthwelker *et al.* by enabling temperature and humidity measurements directly on-chip.

De Smit *et al.* adapted a micro-electromechanical systems (MEMS) cell designed for transmission electron microscopy (TEM)<sup>235</sup> to perform the first spectro-STXM study of a working catalyst (Fig. 9a).<sup>200</sup> They studied an iron-based catalyst during a Fischer-Tropsch synthesis (FTS), which is used to convert CO and  $\text{H}_2$  gas into hydrocarbon products. Imaging the catalyst at the C K-edge, O K-edge and Fe  $\text{L}_{2,3}$ - and  $\text{L}_3$ -edges enabled them to quantify the different iron phases formed and investigate their contribution to the FTS reaction. The same team followed up this work by imaging a single catalyst particle at different FTS reaction temperatures up to 500 °C.<sup>201</sup> Yoo *et al.* also adapted a commercial cell designed for TEM to study the oxidation of CO gas by a  $\text{TiO}_2$ -supported Pt catalyst.<sup>202</sup> By using STXM at the Ce M-edge, they showed that doping of the  $\text{TiO}_2$  support with Ce encouraged the formation of highly efficient Pt single atoms at  $\text{CeO}_x\text{-TiO}_2$  interfaces.

**5.2.3 Liquid flow cells.** Although originally developed for the field of biology,<sup>231,232</sup> most subsequent liquid flow cells for TXM/STXM have been developed for applications in electrochemistry. Sun and Wang constructed a stainless steel flow cell with silicon nitride windows to study a galvanic replacement reaction between Ag nanowires and aqueous Au species by TXM.<sup>203</sup> However, this device contained no active electrical components. To our knowledge, the first active electrochemical flow-cell was reported by Bozzini *et al.*<sup>236</sup> Like previous designs for static electrochemical cells, theirs was also based on a Si/ $\text{Si}_x\text{N}_y$  chip, however, better device sealing and more consistent spacing between  $\text{Si}_x\text{N}_y$  windows were obtained through the use of a UV-curable resin instead of glue or vacuum grease. They used their device to study the electrodeposition of a Co-polypyrrole electrocatalyst using both STXM and scanning  $\mu$ XAS with fluorescence read-out to perform XANES at particular points of interest.

Lim *et al.* used a commercial electrochemical flow-cell to study single Li-ion battery particles under charging and discharging cycles (Fig. 9b).<sup>204</sup> STXM enabled them to observe spatial heterogeneities in Li composition arising from non-uniform rates of lithiation and delithiation, which could affect battery performance and safety. Similarly, Mefford *et al.* used the same electrochemical flow cell to study compositional heterogeneities and the resulting catalytic heterogeneities within electrocatalyst single



crystals.<sup>205,206</sup> Other microfluidic electrochemical cells for TXM/STXM have been reported for studying electrode-electrolyte interactions,<sup>207</sup> including the hybrid device of Prabu *et al.*, which combined a Si/Si<sub>x</sub>N<sub>y</sub> type chip with a 3D-printed holder for making world-to-chip connections.<sup>208</sup>

In contrast to most of the flow devices we have reviewed for scattering and spectroscopy, which were designed for rapid fluid mixing, most *in situ* TXM/STXM—and even TEM—studies have not been focused on flow management. This is likely because the reactions of interest were initiated by localized heating or an applied voltage rather than by the mixing of chemical reactants, and simply ensuring the replenishment of an electrolyte was sufficient for device operation. In this context, Gosse *et al.* presented a Si/Si<sub>x</sub>N<sub>y</sub> type device for STXM designed to study precipitation reactions with precise flow control.<sup>89</sup> By using a pressure-actuated, rather than syringe-driven, system with flow meters upstream and downstream of the chip, the authors demonstrated the ability to adjust or stop flows within seconds. They also showed that the liquid within the Si/Si<sub>x</sub>N<sub>y</sub> cell could be completely refreshed in less than two minutes using flows of only a few microliters per minute.

### 5.3 Tomography for flow imaging

**5.3.1 Early two-dimensional and tomographic work.** Two-dimensional X-ray imaging of macroscale flows dates back to the 1950s and 1960s, when it was used to visualize opaque multiphasic fluidized beds and chemical reactors that could not be imaged by optical methods.<sup>237</sup> Much later work at third generation synchrotron sources on X-ray phase contrast imaging paved the way for higher resolution studies of weakly absorbing liquids and soft materials.<sup>238</sup> Lee and Kim exploited these developments to perform the first 2D X-ray particle image velocimetry (PIV) study of a microflow in 2003.<sup>209</sup> Using an X-ray beam, rather than a conventional laser-based PIV probe, the authors irradiated a flow of alumina microspheres within a 750 μm diameter PTFE tube to extract the velocity field. Lee *et al.* subsequently extended the technique into 3D by using a beam splitter and mirror to image a microflow from two directions and extract a third velocity component.<sup>210</sup>

Around the same time, work was beginning in the geological community to visualize processes within porous rocks that were also inaccessible to light microscopy. X-ray micro-computed tomography (μCT) was already an established method for investigating the internal 3D microstructure of geological samples. The next step was to combine it with a fluidic sample environment to perform dynamic studies. Cylindrical rock cores with diameters on the millimeter scale are thin enough to allow the transmission of hard X-rays, and they can also be assembled into simple millifluidic devices by sealing the sides with an epoxy resin and making fluid connections at both ends. Early work in this area required the sample to be alternatively applied with a flow and then taken to the beamline for

imaging due to the difficulty of attaching flow equipment to a rotating tomography stage.<sup>239</sup> Subsequent studies, such as from Prodanović *et al.*<sup>211</sup> and Noirliel *et al.*,<sup>212</sup> were performed *in situ* but not *operando*, in that the devices were mounted on the stage during flow, but the flows were stopped during imaging. Thus, the difficulty of connecting the flow apparatus to the sample stage and the long acquisition times required to obtain a full tomogram continued to limit the potential time-resolution of the technique.

**5.3.2 Investigations of flow phenomena.** The situation improved with the development of so-called “fast-μCT” methods, in which full tomograms can be acquired in seconds or less. This is made possible using synchrotron radiation and high frame rate detectors by synchronizing the rotation of the sample stage with the acquisition of 2D projections.<sup>240,241</sup> Berg *et al.* were the first to utilize these advances in fast-μCT for *operando* studies of fluid transport within opaque porous media.<sup>213</sup> To enable the fast rotation of the sample for the rapid acquisition of projections, the authors constructed an integrated millifluidic device containing pumps, fluid reservoirs, and an encased rock sample that could be mounted directly on the motorized stage without external tubing connections (Fig. 10a). They investigated the displacement of oil within a sub-millimeter porous network of sandstone and observed Haines jumps, snap-off events, and the entrapment of oil droplets with a temporal resolution of 16.8 s in 3D (Fig. 10b). Armstrong *et al.* later followed up this work to obtain better spatial and temporal resolution by incorporating information from individual 2D projections on the millisecond time-scale.<sup>214</sup> The authors utilized the continuous rotation of the sample and simultaneous collection of projections to identify time points at which fluid motion occurred. Then the projections from intervals of relatively little motion could be reconstructed into 3D tomograms with fewer blurring artefacts.

The time resolution of full tomograms has continued to increase. For example, Hasan *et al.* used fast-μCT to study solute transport in water-saturated and -unsaturated porous media with a full-tomogram time resolution as short as 6 s.<sup>215</sup> Piovesan *et al.* fabricated a porous millifluidic device using a powder-based 3D printer and used it to study capillary wicking in 3D.<sup>216</sup> They performed fast-μCT with sub-second time resolution, however, the readout time of the detector limited the frequency of tomogram acquisition, requiring a 12 s time step between consecutive tomograms. To the best of our knowledge, Dobson *et al.* performed the first *operando* fast-μCT experiment with both a sub-second time resolution and time step, with full-tomogram acquisition frequencies up to 20 Hz.<sup>217</sup> More recently, Bultreys *et al.* combined earlier work in 2D X-ray PIV with fast-μCT to perform the first synchrotron-based 3D X-ray PIV study of flow within porous media.<sup>218</sup> They imaged multiphase flows containing tracer particles within limestone and sintered glasses and obtained tomograms with 0.25 s time resolution at an acquisition rate of 4 Hz. Many



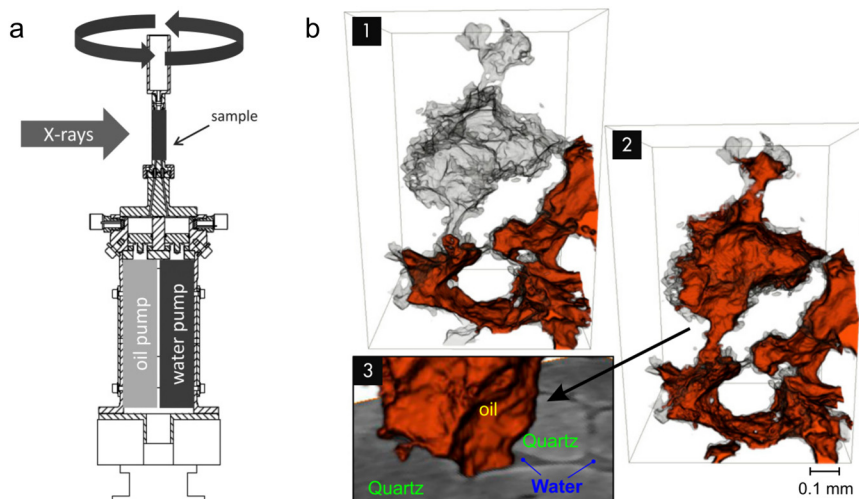


**Fig. 10** *Operando* X-ray micro-computed tomography. (a) An integrated millifluidic device for fast- $\mu$ CT that can be mounted on a rotated tomography stage without external connections (adapted with permission from Armstrong *et al.* 2014; Copyright 2014 John Wiley and Sons).<sup>214</sup> (b) Drainage of water (gray) and infilling of oil (red) within sandstone pores observed with fast- $\mu$ CT (1–2). (3) Cross-section at a pore throat showing the three phases (water, oil, and quartz rock) (used with permission from Berg *et al.* 2013; Copyright 2013 The Authors).<sup>213</sup>

additional studies of hydrology in porous media have been conducted using fast- $\mu$ CT and millifluidics and cannot all be covered here.<sup>242–247</sup> To our knowledge, the only microfluidic  $\mu$ CT study of fluid transport was reported by Knoška *et al.*, who characterized the flow within a helical Kenics mixer by merging streams of low-contrast water and a high-contrast KI solution.<sup>219</sup> Due to the steady-state concentration profile of the flows in the static mixer, standard  $\mu$ CT with an acquisition time of  $\sim$ 2.5 h was sufficient to capture the mixing process.

**5.3.3 Investigations of geochemistry and mineral precipitation.** In parallel with tomographic work focused on fluid transport, *operando* tomography was also used to investigate geochemical processes occurring at the fluid-pore interface. Unlike for fluid dynamics, due to the slow speed of many of these processes, it is not always necessary or practical to obtain consecutive tomograms of near-second resolution over durations of hours. This would result in the collection of large volumes of redundant data. For this reason, slower acquisition rates are often used, and collections may be spaced further apart throughout the experiment. For example, Noiriel *et al.* used  $\mu$ CT and a millifluidic device to study the dissolution of calcite within fractured limestone under acidic conditions. They followed the dissolution process over 55 hours using tomograms collected at six different time points.<sup>220</sup> Similarly, Godinho *et al.* used a continuous flow millifluidic device to study the precipitation of barite ( $\text{BaSO}_4$ ) within a microporous silica column.<sup>221</sup> Using  $\mu$ CT with a time resolution of 24 minutes, they followed the precipitation-induced occlusion of pores and the resulting changes in the flow velocity and crystal growth rate. Fusseis *et al.* developed a Hassler-type millifluidic cell for performing fast- $\mu$ CT of fluid–rock interactions under extreme conditions up to 200 °C and 15 MPa.<sup>222</sup> In particular, they studied the dissolution and

precipitation of magnesium-based minerals under high salt and carbonate solution conditions. More recently, Morais *et al.* further miniaturized these geochemical studies by using a packed-bed microfluidic reactor and X-ray laminography,<sup>223</sup> a computed tomography technique for obtaining high-resolution 3D images of thin planar samples.<sup>248</sup> The authors packed a wide microfluidic reservoir with particles of calcite and subsequently injected packets of acidified media to study the dissolution dynamics of this mineral bed. X-ray tomograms were acquired between each injection of an acidified fluid volume, and the changing structure of the bed caused by the dissolution process was input into a CFD model to simulate the resulting flow profiles.

To investigate diffusive- rather than advective-driven transport processes in samples with smaller pore sizes, several researchers fabricated simple counter-diffusion-based devices. These devices are easier to set up at tomography beamlines than their flow-based counterparts since it is not necessary to mount pumps on the sample stage or connect devices to external equipment. For example, Godinho *et al.* made a passive-diffusion cell by connecting short sections of tubing to both sides of a 3 mm-diameter shale sample containing micrometer-scale fractures and sub-micron sized pores.<sup>224</sup> The tubing sections served as fluid reservoirs containing counter-ions, which were allowed to diffuse into the sample, and the whole assembly was mounted vertically on the stage using one of the tubes as the support. Using this device, the authors continued their  $\mu$ CT studies of  $\text{BaSO}_4$ . They observed that as  $\text{Ba}^{2+}$  and  $\text{SO}_4^{2-}$  ions diffused and reacted within the sample, barite precipitated first within the larger fractures and then later in smaller fractures and pores.

Anduix-Canto *et al.* used a similar setup to study the precipitation of calcium sulfate within controlled porous glass (CPG) rods with an average pore diameter of 7 nm.<sup>225</sup> The authors performed not only  $\mu$ CT, but also X-ray

diffraction computed tomography (XRD-CT) to reveal both the morphology and crystal structure of the phases that precipitated over time. Utilization of CPGs enabled the authors to confine the solution within nanopores that were completely isolated from macropores, and this nanoscale confinement effect led to the precipitation and stabilization of normally unstable amorphous and hemihydrate  $\text{CaSO}_4 \cdot x\text{H}_2\text{O}$  phases. The field of geological  $\mu\text{CT}$  is a large area, often on the border between milli- and “macro”-fluidics, and thus cannot be completely covered here. The reader is directed to other reviews for further information.<sup>246,249</sup>

#### 5.4 Other scanning techniques

In addition to absorption- and phase-contrast X-ray imaging and tomography, several microfluidic studies have made use of the spatially resolved acquisition of other types of X-ray data. The most popular approach in the physical sciences has been using scanning  $\mu\text{XRF}$  to map micromixers and visualize the concentration profiles of chemical species. Such an approach was implemented by Nagasaka *et al.*, who utilized a microfluidic device comprising a PDMS microchannel and a silicon nitride window to study the mixing of pyridine and water.<sup>226</sup> They first mapped the steady-state laminar microflow by  $\mu\text{XRF}$  and then obtained N K-edge XAS spectra at different points across the width of the microchannel to determine the local pyridine concentration. Similarly, Chaussavoine *et al.* developed a vacuum-compatible microfluidic device for studying the synthesis of iron (hydr)oxide nanoparticles.<sup>227</sup> They performed  $\mu\text{XRF}$  of the channel and identified regions of interest at which to acquire full Fe K-edge XANES spectra using fluorescence read-out. This approach was also utilized in several studies previously reviewed in section 4.<sup>156,171,172</sup>

Scanning  $\mu\text{XRF}$  has also been used to study spatial heterogeneities within planar microfluidic devices. For example, Chen and Kocar investigated Fe-As-S geochemical reactions using devices containing arrays of quartz micro-posts as models of porous rock.<sup>228</sup> First, the authors would mix a basal salts solution (BSS) with an  $\text{Fe}^{2+}$  solution to precipitate iron (hydr)oxides. Subsequently, As- and S-containing solutions were introduced along with NaBr as a flow tracer, and the resulting flow profiles and sorption of As/S were visualized by  $\mu\text{XRF}$  (Fig. 11). Similarly, Neckel *et al.* used scanning XRF to map the electrodeposition of Ag/AgCl films within a microfluidic electrochemical cell.<sup>229</sup> They utilized a nanobeam to obtain maps of Ag nucleation sites with sub-micron resolution.

Finally, in an interesting recent study, Matsumoto *et al.* utilized a multi-window  $\text{Si}/\text{Si}_3\text{N}_4$  microfluidic device at an XFEL to perform coherent diffraction imaging (CDI) of nanoparticle aggregation.<sup>229</sup> Two separate suspensions of spherical and rod-shaped gold nanoparticles, respectively, were stored on-chip. Mixing of the solutions was initiated by an XFEL pulse breaking a silicon nitride window at the end of the flow channel and rapidly depressurizing the device

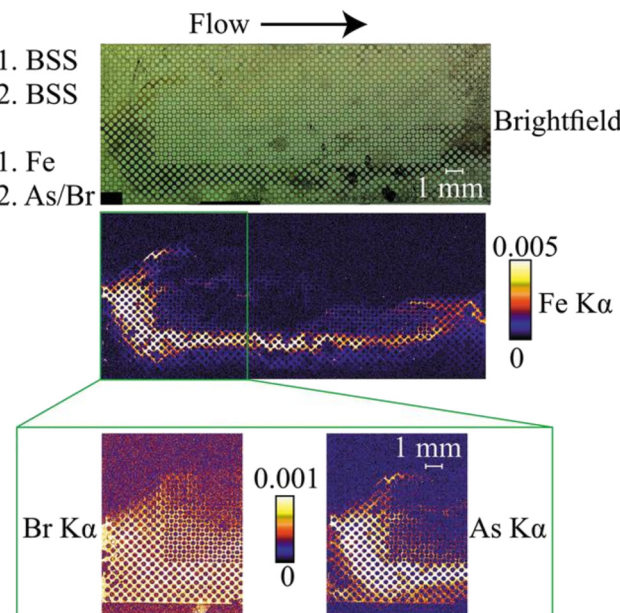


**Fig. 11** Scanning  $\mu\text{XRF}$  within a microfluidic device containing micro-post arrays. Brightfield optical image illustrating the flow direction and chemical addition (top). Model geochemical reactions in the Fe-As-S system are monitored using the appropriate  $\text{K}\alpha$  fluorescence peak (bottom and insets). Br is utilized as a flow tracer (reproduced with permission from Chen and Kocar, 2021; International Union of Crystallography).<sup>228</sup>

under vacuum. Once a flow was established, the device was scanned upstream along the channel to image particles under different aggregation states. To our knowledge, this may be the only example of on-chip microfluidic analysis at an XFEL, and it illustrates a creative way to overcome the challenge of X-ray pulse-induced device damage through experimental design.

## 6 Developments in laboratory-based analysis

In this final review section, we will look at developments in performing *in situ* micro- and milli-fluidics experiments in the ‘home’ laboratory, that is, using laboratory X-ray instruments rather than large-scale facilities. Even researchers and institutions with strong official links to a synchrotron radiation facility cannot expect more than a few weeks of beamtime per year under normal circumstances. For other researchers and relative newcomers to user facilities, more than a few days per year might be a luxury. Conducting an experiment with a complex sample environment at another institution also requires a great deal of planning, set-up, and hard work. Additionally, one may utilize unfamiliar equipment or software and rely heavily on the help of local staff, who will have varying levels of investment in user experiments. These are just a few of the many reasons why researchers are interested in the ability to



perform microfluidics experiments—and *in situ* experiments in general<sup>250,251</sup>—in a laboratory setting.

Fortunately, there have been substantial improvements in laboratory X-ray sources and hardware over the past decade and a half. First and foremost, the flux of rotating anode and liquid metal jet X-ray sources has approached that of second-generation synchrotron facilities,<sup>11</sup> achieving up to  $\sim 10^9$  photons per second at the sample depending on the source type and collimation/focusing optics.<sup>15,252</sup> State-of-the-art sealed tube sources are also improving and able to reach the  $\sim 10^7$ – $10^8$  range. Multilayer optics and scatterless slits have provided better quality beams,<sup>253,254</sup> and sensitive, low-noise, hybrid photon counting detectors used at synchrotrons are now commonly employed on laboratory systems.<sup>255,256</sup> Further, current commercial systems offer better software and increased functionality, automation, and sample control, reducing the need to build custom platforms. All these factors have increased the performance and user-friendliness of laboratory X-ray instruments, resulting in renewed interest in using them to perform *operando* experiments. While they still cannot compete with third- and fourth-generation synchrotrons in terms of flux or coherence, more and more micro- and milli-fluidics experiments are becoming feasible in the laboratory, as the papers reviewed below demonstrate (Table 4). Here, we will again cover progress in scattering/diffraction, spectroscopy, and imaging, and we will also include biological and soft matter applications since, to our knowledge, laboratory X-ray analysis in these areas has not been reviewed previously. Where possible we will also compare the data quality and time resolution of laboratory-based studies to similar synchrotron experiments.

## 6.1 X-ray scattering and diffraction

**6.1.1 Early work and acquisition time considerations.** Micro- and milli-fluidic laboratory-based X-ray scattering analysis has its origin in the recirculating flow cells used to sample materials forming within batch reactors. This early work focused on monitoring the crystallization of model pharmaceutical compounds by powder X-ray diffraction<sup>288,289</sup> or the synthesis of nanoparticles by SAXS,<sup>290</sup> where the continuous recirculation of products between mL- to L-scale batch reactors and the X-ray instrument facilitated *operando* measurements. To our knowledge, it was Polte *et al.* who first coupled a true continuous flow reactor to a laboratory X-ray instrument for *operando* analysis (Fig. 12a).<sup>257</sup> The authors utilized a millifluidic mixer module connected to a glass capillary to study the synthesis of gold NPs by SAXS. By using different lengths of tubing between the mixer and analysis capillary, the authors were able to study reaction times from 0.1 to 136 s with  $\sim 100$  ms time resolution, despite requiring  $\sim 3$  min to acquire laboratory SAXS curves. The authors followed-up this work by using the same flow system to study silver<sup>258</sup> and palladium<sup>259</sup> NP synthesis.

A similar approach was later employed by Chen *et al.* and Herbst *et al.* to study the nucleation and growth of gold and

ZnO NPs, respectively, over hours by simultaneous SAXS/WAXS and UV-vis spectroscopy.<sup>260,261</sup> In contrast to Polte *et al.*, once a steady flow was achieved within the capillary, flows were stopped and the reactions were followed within the static solutions. The authors analyzed the syntheses with a time resolution of between 0.5 and 10 minutes depending on the required acquisition time. Tillier *et al.* used a modified version of the electrochemical flow cell of Binninger *et al.* (reviewed in section 4.2.4) to study the degradation of carbon-supported Pt NP catalysts.<sup>262</sup> Compared to their synchrotron experiments with exposure times on the second to minute time-scale, the acquisition of laboratory SAXS patterns with good signal-to-noise ratio required approximately 1 hour. Therefore, it is clear that depending on the kinetics of a reaction or process of interest, the experiment must be designed to consider the acquisition time required for lower flux laboratory sources.

**6.1.2 Biological applications.** Laboratory sources have also been utilized for biological applications. Bucciarelli *et al.* used a laboratory SAXS platform with an integrated millifluidic flow system to study biomolecules fractionated by inline size-exclusion chromatography (SEC).<sup>263</sup> This so-called “SEC-SAXS” technique is utilized to produce monodisperse populations of often heterogeneous and unstable biological samples so that quantitative information on the structure, dynamics, and molecular weight of specific biomolecules can be extracted from SAXS data. This was the first time SEC-SAXS was performed without the use of synchrotron radiation, and the authors demonstrated that high quality data could be obtained with a similar amount of sample consumption and total experimental time with no radiation damage. Anaraki *et al.* used millifluidics and laboratory SAXS to study the stability of NP suspensions in the presence of biomolecules, an important parameter related to the behavior of nanoparticles in the environment and within the human body.<sup>264</sup> The authors utilized a micromixer coupled to a quartz capillary to study the aggregation of silica NPs in the presence of human serum albumin (HSA) and in media with differing pH and ionic strength. They found that HSA significantly accelerates the aggregation of silica compared to the pH or ionic strength jumps studied.

**6.1.3 Multi-source studies.** Several research teams have also worked on projects using a combination of synchrotron radiation and laboratory sources. For example, Besenhard *et al.* used synchrotron PXRD (see section 3.3.3) and laboratory SAXS to study the synthesis of iron oxide nanoparticles.<sup>127</sup> The authors used a continuous flow millifluidic device to assess the aggregation state of freshly precipitated NPs, finding that they were already highly aggregated after 5 s of reaction time. They subsequently used a semi-batch setup to study the de-agglomeration of the NPs using a neutralizing solution of citric acid, confirming de-agglomeration began within 20 s of citric acid addition. Lange *et al.* performed a synchrotron SAXS and WAXS study (see section 3.3.2) and used a laboratory SAXS platform to design and evaluate their microfluidic device before their





Table 4 Micro- and milli-fluidic devices for laboratory-based X-ray analysis

X-ray technique(s)	Device type	Device material(s)	Fabrication and/or assembly method	Window material, thickness	Geometry/mode, beam pathlength	Sample(s) investigated	Conditions	Instrument, source, detector	Beam size/resolution	Acquisition mode, exposure time	Ref.
SAXS	Millifluidic continuous flow reactor	Teflon tubing, quartz capillary, commercial micromixer	Components connected by tubing, compression fittings	Quartz capillary, 10 $\mu\text{m}$ wall	Transmission, 1–3.8 mm	Au NPs and Ag NPs	Ambient temperature & pressure	SAXSess (Anton Paar), sealed tube source (PANalytical, 8.04 keV), CCD detector (Roper Scientific)	Unknown	Multiframe, 20 $\times$ 10 s	Polte <i>et al.</i> (2010) <sup>257</sup> Polte <i>et al.</i> (2012) <sup>258</sup>
SAXS	Millifluidic continuous flow reactor	Teflon tubing, quartz capillary, commercial micromixer	Components connected by tubing, compression fittings	Quartz capillary, 10 $\mu\text{m}$ wall	Transmission, 1 mm	Pd NPs	Ambient temperature & pressure	SAXSess (Anton Paar), sealed tube source (PANalytical, 8.04 keV), CCD detector (Roper Scientific)	Unknown	Multiframe, unknown	Kettemann <i>et al.</i> (2015) <sup>259</sup>
SAXS/WAXS	Millifluidic continuous flow reactor	Teflon, polyethylene tubing, quartz capillary	Components connected by tubing, compression fittings	Quartz capillary, 10 $\mu\text{m}$ wall	Transmission, 1 mm	Au NPs	22, 33, and 45 °C, pressure	Double Ganesh AIR (SAXSLAB), rotating anode source (Rigaku, 8.04 keV), hybrid-photon counting detector (Dectris)	Unknown	SAXS: multiframe, 60, 300, or 600 s exposures depending on the condition and reaction time WAXS: unknown	Chen <i>et al.</i> (2015) <sup>260</sup>
SAXS/WAXS	Millifluidic continuous flow reactor	Teflon, polyethylene tubing, quartz capillary	Components connected by tubing, compression fittings	Quartz capillary, 10 $\mu\text{m}$ wall	Transmission, 1 mm	ZnO NPs	40 and 50 °C, pressure	Double Ganesh AIR (SAXSLAB), rotating anode source (Rigaku, 8.04 keV), hybrid-photon counting detector (Dectris)	Unknown	SAXS: multiframe, 30, 60, or 600 s exposures depending on the reaction time WAXS: multiframe, 1200 s exposures	Herbst <i>et al.</i> (2019) <sup>261</sup>
SAXS	Millifluidic electrochemical flow cell	PEEK, Kapton (gold-coated)	Machined, clamped	Kapton, 2 $\times$ 50 $\mu\text{m}$	Transmission, 50–123 $\mu\text{m}$ of catalyst, 2 mm of electrolyte	Pt NPs on a carbon support	Ambient temperature & pressure	X-Pert Pro (PANalytical), sealed tube source (PANalytical, 8.04 keV), 1D solid-state detector (PiXcel)	Unknown	Multiframe 7 $\times$ 1 h	Tillier <i>et al.</i> (2016) <sup>262</sup>

Table 4 (continued)

X-ray technique(s)	Device type	Device material(s)	Fabrication and/or assembly method	Window material, thickness	Geometry/mode, beam pathlength	Sample(s) investigated	Conditions	Instrument, source, detector	Beam size/resolution	Acquisition mode, exposure time	Ref.
SAXS	Millifluidic high performance liquid chromatography system	Unknown	Compression fittings connecting multiple commercial devices	Glass capillary, unknown wall	Transmission, unknown	Proteins	Ambient temperature & pressure	BioXolver L (Xenocs), liquid metal jet source (Excillum, 9.25 keV)	~1 mm × 1 mm	Single-shot, 60 s	Bucciarelli <i>et al.</i> (2018) <sup>263</sup>
SAXS	Millifluidic continuous flow mixer	PMMA, quartz capillary	Unknown	Quartz capillary, unknown wall	Transmission, 2 mm	SiO <sub>2</sub> NPs and human serum albumin	Ambient temperature & pressure	NanoStar (Bruker), microfocus source (8.04 keV), 2D gas-based detector (VANTEC-2000)	~300 μm diameter	Single-shot, 2.5–30 h	Anaraki <i>et al.</i> (2020) <sup>264</sup>
SAXS	Millifluidic continuous flow reactor	Glass capillary, PTFE tubing, polymer fittings	Compression fittings, tubing coiling	Quartz capillary, 10 μm wall	Transmission, 1 mm	Iron oxide NPs	60 °C, ambient pressure	SAXSess (Anton Paar), sealed tube source (GE, 8.04 keV), 1D solid-state detector (Debris) Xeuss 2.0 (Xenocs), sealed tube source (Xenocs, 8.04 keV), hybrid photon counting detector (Debris)	17 mm × 0.25 mm	Single-shot, 60 s	Besenhard <i>et al.</i> (2020) <sup>127</sup>
SAXS	Microfluidic segmented flow	OSTEMER 322	Photolithography, soft lithography, cured and laminated	OSTEMER 322, 2 × 200 μm	Transmission, 150 μm	Device materials	Ambient temperature & pressure	Xeuss 2.0 (Xenocs), sealed tube source (Xenocs, 8.04 keV), hybrid photon counting detector (Debris)	Unknown	Multiframe, 500 s total scan time	Lange <i>et al.</i> (2020) <sup>92</sup>
Micro-XRD	Microfluidic electro-chemical cell	PVC, brass, graphite	Machining, clamping, pressure fittings, conductive epoxy	Kapton, unknown, graphite, 500 μm	Transmission, ~400 μm	Iron and iron oxide phases	Ambient temperature & pressure	Custom diffractometer, rotating anode source (Rigaku, 17.4 keV), image plate detector (unknown)	400 μm diameter or 20 × 20 μm	Multiframe, 20 min scan time	Monnier <i>et al.</i> (2008) <sup>163</sup> Monnier <i>et al.</i> (2014) <sup>164</sup>
SAXS	Microfluidic evaporative flow	PDMS	Photolithography, soft lithography, plasma bonding	PDMS, ~150 μm	Transmission, 25 μm	Au colloidal supercrystals	Ambient temperature & pressure	Rotating anode source (Rigaku, 8.04 keV), hybrid-photon counting detector (Debris)	~0.5 mm × 0.5 mm	Single-shot, ~3.5 min	García-Lojo <i>et al.</i> (2021) <sup>265</sup>
SAXS	Millifluidic dialysis device	COC, commercial dialysis insert	3D printing	COC, 2 × 50 μm	Transmission, 12 mm	Lipids and polymers	Ambient temperature & pressure	Microfocus source (Xenocs, 17.4 keV), unknown	Unknown	Multiframe, 360 × 1 min Single-shot, 20 min	Ehm <i>et al.</i> (2022) <sup>266</sup>

Table 4 (continued)

X-ray technique(s)	Device type	Device material(s)	Fabrication and/or assembly method	Window material, thickness	Geometry/mode, beam pathlength	Sample(s) investigated	Conditions	Instrument, source, detector	Beam size/resolution	Acquisition mode, exposure time	Ref.
SAXS/WAXS and PXRD	Microfluidic segmented flow	PMMA, PTFE, Kapton, silicone	UV laser cutting, clamped, compression fittings	Kapton, 2 × 75 µm	Transmission, 300 µm	CaCO <sub>3</sub> with nucleating agents, silica NPs	Ambient temperature & pressure	detector Xeuss 2.0 (Xenocs), liquid metal jet source (Excillum, 9.25 keV), hybrid photon counting detector (Dectris)	~250 µm × 250 µm	Multiframe, 60 × 0.5 s	Levenstein <i>et al.</i> (2022) <sup>15</sup>
	Milli-fluidic segmented flow	Kapton capillary	Interference fit, compression fittings	Kapton capillary, 100 µm wall	Transmission, 1 mm	Calcite and paracetamol crystals		Xtalab Synergy R or Synergy Custom (Rigaku), microfocus rotating anode source (Rigaku, 8.04 keV), hybrid photon counting detector (Rigaku)	~140 µm × 140 µm	Multiframe, 3600 × 25 ms	
SAXS	Microfluidic continuous flow	OSTEMER, Kapton	Photolithography, PDMS injection molding, cured, cure-bonded	OSTEMER, 2 × 50 µm and Kapton, 25 µm	Transmission, 400 µm	Au NPs, silica NPs, BSA protein, latex NPs	Ambient temperature & pressure	detector Xeuss 2.0 (Xenocs), microfocus source (Xenocs, 8.04 keV), hybrid photon counting detector (Rigaku)	250 µm × 250 µm	Single-shot, 10–60 min	Radajewski <i>et al.</i> (2023) <sup>267</sup>
SAXS	Millifluidic continuous flow reactor	PFA tubing, glass capillary	Compression fittings, tubing, coiling	Glass capillary, unknown wall	Transmission, unknown	Polymer nano-objects	75 °C, 6.9 bar backpressure	detector Xeuss 3.0 (Xenocs), liquid metal jet source (Excillum, 9.25 keV), hybrid photon counting detector (Dectris)	0.4 mm diameter	Single-shot, 5 min	Guild <i>et al.</i> (2023) <sup>268</sup>
PXRD	Various micro- and milli-fluidic devices	Various	Various	Various	Calcite, theophylline, KNO <sub>3</sub> , Na <sub>2</sub> SO <sub>4</sub>	Various		Xtalab Synergy Custom (Rigaku), microfocus rotating anode source (Rigaku, 8.04 keV), hybrid photon counting	150 µm diameter, tunable	Multiframe, 18 s exposure per frame	Turner <i>et al.</i> (2024) <sup>269</sup>



Table 4 (continued)

X-ray technique(s)	Device type	Device material(s)	Fabrication and/or assembly method	Window material, thickness	Geometry/mode, beam pathlength	Sample(s) investigated	Conditions	Instrument, source, detector	Beam size/resolution	Acquisition mode, exposure time	Ref.
XANES	Millifluidic photocatalysis cell	Unknown body material, scotch tape	3D printing (DLP), clamping, tape	Scotch tape, unknown	Fluorescence, unknown	Pt catalyst on TiO <sub>2</sub> support	Ambient temperature, Ar atmosphere	RXAS Looper (Rigaku), unknown source at Pt L <sub>3</sub> -edge, silicon drift detector (Rigaku)	Unknown	Single-shot, ~1-2 min	Kozyr <i>et al.</i> (2023) <sup>270</sup>
XRF	Capillary electro-phoresis cell	Fused silica capillary with polyimide coating	Capillary mounted in plastic housing	Fused silica capillary with polyimide coating, 33.5 μm wall thickness	Fluorescence, unknown	Free and complexed metal ions	Ambient temperature & pressure	Eagle II (EDAX), Rh target excitation source (EDAX), SiLi detector (EDAX)	~50 μm spot	Multiframe, 10 s dwell time for full spectra	Miller <i>et al.</i> (2003) <sup>271</sup>
μXRF and XRD	Miniaturized XRF chip	Glass, PDMS, lead	Various	Glass, unknown	Fluorescence, unknown	Metal foils	Ambient temperature & pressure	XRD spectrometer with HPGe detector (Canberra Industries)	Uncollimated radiation from Am source	Unknown	Greaves and Manz (2005) <sup>18</sup>
	Various millifluidic XRD chips	Polycarbonate, PDMS, borosilicate glass,	Various materials of unknown thickness	Transmission, unknown	Corundum powder			D8 Discover (Bruker), sealed 2D GADDS detector	1 mm diameter		
XRF	Microfluidic liquid-liquid extraction device	Kapton, PLA	3D printing, epoxy, glue	Kapton, 7 μm	Fluorescence, >200 μm	La, Eu, and Yb ions in aqueous and organic media	20-35 °C, 60 mbar back pressure in aqueous channel	X-ray spectrometer with sealed tube source (Moxtek, X-123 SDD detector (AmpTEK))	Unknown	Multiframe, 120 s per exposure	Maurice <i>et al.</i> (2022) <sup>272</sup>
XRF	Millifluidic solid-phase extraction device	Kapton tubes, PEEK tubing, 3D-printed holder	3D printing, tape, silicone sealant	Kapton tubes, 38 μm wall thickness	Fluorescence, 1.52 mm	La, Nd, Yb and Fe ions in acidic media	Ambient temperature & pressure	X-ray spectrometer with sealed tube source (Moxtek, X-123 SDD detector (AmpTEK))	Unknown	Multiframe, 123 s per frame	Olivier <i>et al.</i> (2023) <sup>273</sup>
μCT	Millifluidic cell (Hassler core holder)	PEEK body with other unknown materials	Compression fittings	PEEK, 2 mm	Transmission, 6 mm	Multiphase flow in sandstone	Ambient temperature & pressure	5 μm voxel size	Multiframe, 80 min tomogram acquisition	Youssef <i>et al.</i> (2009) <sup>274</sup>	

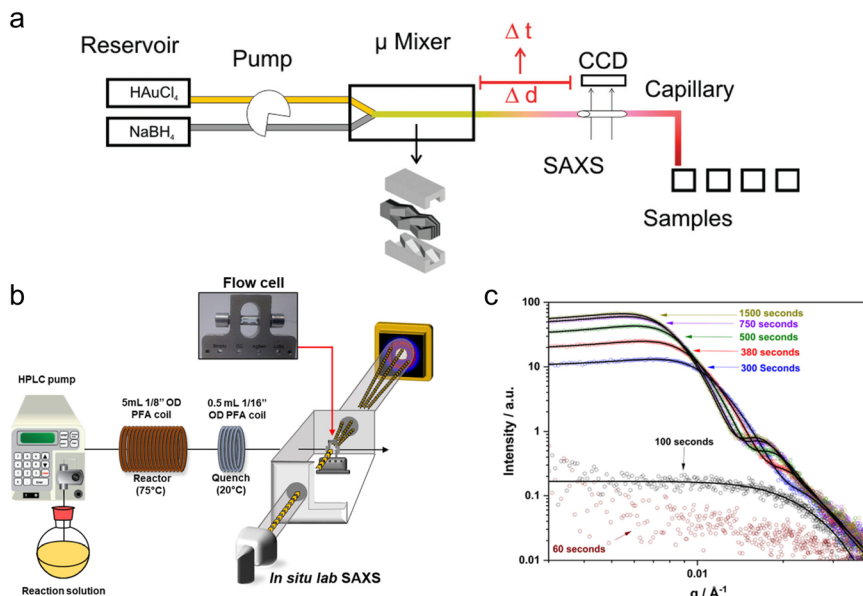


Table 4 (continued)

X-ray technique(s)	Device type	Device material(s)	Fabrication and/or assembly method	Window material, thickness	Geometry/mode, beam pathlength	Sample(s) investigated	Conditions	Instrument, source, detector	Beam size/resolution	Acquisition mode, exposure time	Ref.
µCT	Millifluidic high-pressure flow cell (Hassler core holder)	M55 carbon fiber, viton, aluminum, Kapton	Compression fittings	Carbon fiber, viton, aluminum, and Kapton, unknown thickness	Transmission, 4–6 mm	Supercritical CO <sub>2</sub> and brine in limestone	50–63 °C, 10 MPa pore pressure, 11–13.1 MPa confining pressure	Versa XRM-500 (Xradia), unknown source and detector	2–6.4 µm voxel size	Multiframe, continuous collection of projections, 75–90 min tomogram acquisition	Andrew <i>et al.</i> (2013) <sup>275</sup>
Fast-µCT	Millifluidic flow cell (Hassler core holder)	PMMA, viton, viton O-rings, hydrophobic membranes of unknown material	Compression fittings	PMMA, viton, unknown thickness	Transmission, 6 mm	Multiphase flow in sandstone	Ambient temperature, unknown pressure	Custom gantry-based scanner, microfocus sealed tube source, 2D CMOS scintillator detector	7.4–14.8 µm voxel size	Multiframe, continuous collection of projections, 12 s or 21 min tomogram acquisition	Bultreys <i>et al.</i> (2014) <sup>277</sup>
µCT	Millifluidic high-pressure flow cell (Hassler core holder)	M55 carbon fiber, steel, viton, aluminum, Kapton	Compression fittings	Carbon fiber, viton, aluminum, and Kapton, unknown thickness	Transmission, 4 mm	Multiphase flow in limestone	50 °C, 10 MPa pore pressure, 13 MPa confining pressure	Versa XRM-500 (Xradia), unknown source and detector	3.8 µm resolution	Multiframe, ~15 min tomogram acquisition	Menke <i>et al.</i> (2015) <sup>279</sup>
µCT	Millifluidic flow cell	Glass, heat shrink tubing	Sintering, compression fittings, heat shrink	Heat-shrink tubing, unknown	Transmission, 6 mm	BaSO <sub>4</sub> in microporous glass column	Ambient temperature & pressure	Custom scanner, 2D detector (PerkinElmer)	4.3 µm voxel size	Multiframe, 0.25, 1.5 and 4.9 h tomogram acquisition depending on number of projections selected	Gajjar <i>et al.</i> (2018) <sup>280</sup>
Helical-CT	Millifluidic cell	Quartz	Sintering, compression fittings	No window	Transmission, 3.9 mm	CaCO <sub>3</sub> in microporous glass column	Ambient temperature & pressure	Heliscan (FEI), unknown source and detector	2.24 µm voxel size	Multiframe, ~2.5 h tomogram acquisition	Godinho <i>et al.</i> (2018) <sup>281</sup>
µCT	Millifluidic packed-bed cell	PEEK	Compression fittings, grain packing	PEEK, unknown	Transmission, 7.5 mm	CaCO <sub>3</sub> grains	Ambient temperature & pressure	NSI XCT scanner (North Star Imaging), unknown source, 2D detector (PerkinElmer)	19.3 µm voxel size	Multiframe, 83 s tomogram acquisition	Singh <i>et al.</i> (2024) <sup>282</sup>

Table 4 (continued)

X-ray technique(s)	Device type	Device material(s)	Fabrication and/or assembly method	Window material, thickness	Geometry/mode, beam pathlength	Sample(s) investigated	Conditions	Instrument, source, detector	Beam size/resolution	Acquisition mode, exposure time	Ref.
Tomographic X-ray PIV	Millifluidic flow cell and microporous column	Carbon fiber tube	Sintering, compression fittings	Carbon fiber, 1 mm	Transmission, 6.35 mm	Silver-coated hollow glass spheres in different creeping flows	Ambient temperature & pressure	CoTeOM (TBSCAN), sealed tube source, 2D silicon detector	18 $\mu\text{m}$ voxel size	Multiframe, 14.5 ms per projection, <3 s tomogram acquisition	Mäkitalo et al. (2021) <sup>283</sup>
Tomographic X-ray PIV	Millifluidic flow cell (Hassler core holder)	Viton and other unknown materials	Sintering, compression fittings, grain packing	Unknown	Transmission, 4 mm	Silver-coated hollow glass spheres in a sand pack and microporous glass column	Ambient temperature, 2 MPa confining pressure	Custom gantry-based scanner, microfocus sealed tube source, 2D CMOS scintillator detector	11.8 $\mu\text{m}$ voxel size	Multiframe, 100 ms per projection, 70 s tomogram acquisition	Bultrey et al. (2022) <sup>284</sup>
GE-XRF and scanning $\mu\text{XRF}$	Passive semi-open microfluidic chip	Unknown	Unknown fabrication steps, acidic surface treatment, silanization	No window	Fluorescence, dried sample thickness	Dried Cd, and Fe salts	Ambient temperature & pressure	GE-XRF: ~10 mm	GE-XRF: single-shot, 300 s	GE-XRF: single-shot, 100 ms per grid point	Tsujii et al. (2005) <sup>285</sup>
Confocal 3D-XRF	Multi-layer microfluidic chip	PET	Commercially purchased	PET, 2 $\times$ 125 $\mu\text{m}$	Fluorescence, 849 $\mu\text{m}$	Aqueous Co and Cu solutions	Ambient temperature & pressure	$\mu\text{XRF}$ : 50 $\mu\text{m}$ spot (Rontec) Ceramic sealed tube source (RW, 17.4 keV), silicon drift detector (Bruker)	$\mu\text{XRF}$ : 50 $\mu\text{m}$ spot (Rontec) Ceramic sealed tube source (RW, 17.4 keV), silicon drift detector (Bruker)	unknown	Nakano and Tsujii (2010) <sup>286</sup>
Scanning $\mu\text{XRF}$	Passive microfluidic chip	Kapton, polycarbonate, silicone transfer tape	$\text{CO}_2$ laser cutting, tape	Kapton, 40 $\mu\text{m}$	Fluorescence, $\geq 1$ mm	Sr solutions	Ambient temperature & pressure	Custom $\mu\text{XRF}$ system, sealed tube source (XDS, 20.22 keV), silicon drift detector (Hitachi)	Custom: 200 $\mu\text{m}$ diameter, 200 $\mu\text{m}$ step size	Custom: single-shot, 1 s per grid point	McIntosh et al. (2014) <sup>287</sup>
								Eagle III (EDAX): sealed tube source (20.22 keV), Si(Li) detector		Commercial: single-shot, 0.2 s per grid point	



**Fig. 12** Laboratory-based X-ray scattering analysis. (a) A flow system for *operando* SAXS studies of the synthesis of gold nanoparticles. Different tubing lengths ( $\Delta d$ ) between a commercial micro-mixer and the X-ray beam give access to different time points (used with permission from Polte *et al.*, 2010; Copyright 2010 American Chemical Society).<sup>257</sup> (b) A flow system for *in situ* SAXS studies of the polymerization-induced self-assembly comprising a heated reactor module and a cold-quench to stop the reaction before SAXS analysis. (c) Time-resolved SAXS data of nano-objects obtained with the system in (b) at reaction times controlled by the applied flow rate (adapted with permission from Guild *et al.* 2023; Copyright 2023 The Authors).<sup>268</sup>

beamtime.<sup>92</sup> They evaluated the scattering profile of their chosen device material, OSTE+, as a potential X-ray window against more commonly used Kapton and found that it had lower background and structure in the SAXS region. After selecting to use a completely OSTE+ device, they checked its transmission profile as a function of its thickness. They also refined the fabrication protocol to produce devices that would not age under the beam, and thus result in inconsistent background signal. Similarly, Monnier *et al.* used laboratory micro-XRD to complement their synchrotron XAS experiments on the corrosion of iron phases (see section 4.2.1).<sup>163,164</sup> Micro-XRD was used to confirm the phase composition before and after redox processes and identify reaction intermediates that contributed to shifting absorption edges in the XANES spectra.

García-Lojo *et al.* performed a synchrotron and laboratory SAXS study of the assembly of NPs into colloidal supercrystals by pervaporation in microfluidic channels.<sup>265</sup> In comparing 2D SAXS data collected at the synchrotron and the laboratory, they observed that single-crystal small angle diffraction spots were much better resolved in the synchrotron data due to the smaller beam size and higher angular resolution. Finally, Ehm *et al.* 3D printed a millifluidic dialysis chamber with COC windows for monitoring 100  $\mu\text{L}$  samples by SAXS.<sup>266</sup> They demonstrated the device by following reversible structural transitions in lipids and polymers induced by changing media pH and salt concentration over hours using acquisition times of 20 min. The *in situ* laboratory SAXS data were compared to *ex situ* data collected using synchrotron radiation with good agreement.

**6.1.4 Exploring the limits of laboratory analysis.** Two recent studies sought to explore the limits of *in situ* laboratory-based X-ray scattering analysis of micro- and millifluidic sample environments. Levenstein *et al.* studied a range of different samples, fluidic devices, and X-ray instruments and compared the type of data that could be obtained with an instrument optimized for performing SAXS/WAXS to an instrument optimized for performing single-crystal XRD.<sup>15</sup> In particular, they investigated the potential of using a multi-frame measurement approach with short acquisition times to study processes with fast kinetics. They found that on the highly collimated SAXS/WAXS setup with lower flux at the sample ( $3.7 \times 10^6$  photons  $\text{s}^{-1}$ ), decent quality SAXS data from flowing silica NP solutions could be obtained with even sub-second acquisition times. However, the WAXS signal-to-noise ratio from such short acquisitions was too low to obtain valuable data. Conversely, on the microfocused XRD setup with higher flux at the sample ( $5.7 \times 10^9$  photons  $\text{s}^{-1}$ ), the authors could obtain powder diffraction patterns from flowing organic and inorganic crystallites with acquisition times as short as 25 ms. These results demonstrate that WAXS/XRD analysis is clearly flux limited on laboratory sources, yet SAXS analysis, which requires more collimated beams to avoid smearing at small angles, appears less restricted by the source flux.

Radajewski *et al.* performed a microfluidic SAXS study on a state-of-the-art laboratory SAXS platform that was modified to obtain a small  $0.25 \times 0.25 \text{ mm}^2$  beam while providing a flux density of almost  $10^7$  photons  $\text{s}^{-1}$ .<sup>267</sup> In particular, they investigated the quality of data that could be obtained from



flows of strongly scattering inorganic nanoparticles to moderately to weakly scattering proteins and polymer materials. For the high contrast gold and silica NPs studied, 10 min exposures were enough to obtain good quality SAXS patterns that could be fit with form and structure factors and for which the invariant could be calculated. For more weakly scattering bovine serum albumin (BSA) and latex NPs, longer 1 hour acquisitions were required to fit form factors, and even in these cases, increased noise especially at high  $q$ , made it difficult to resolve all the structure peaks of dilute samples. However, these results are very promising, especially for stronger contrast inorganic materials, and the use of a rotating anode or liquid metal jet source could provide between one and two orders of magnitude greater flux with the same optical configuration.

**6.1.5 Laboratory facilities dedicated to *in situ* measurements.** In the previous subsections, we highlighted research from several groups who have developed methodology for *in situ* laboratory-based X-ray scattering analysis including at the Federal Institute for Materials Research and Testing (BAM, DE),<sup>257,258</sup> the Förster group (DE),<sup>260,261</sup> and our own laboratory at CEA Paris-Saclay (FR).<sup>92,254,290</sup> These advances have led to the recent creation of two new laboratory X-ray facilities dedicated to *operando* X-ray experiments. The first is the DL-SAXS facility managed by the I22 beamline of Diamond Light Source (UK).<sup>268</sup> This facility comprises a commercial SAXS/WAXS platform with a high flux liquid metal jet source, and it is designed to enable tests of sample environments before use on the beamline or as an alternative to synchrotron radiation. Guild *et al.*, recently demonstrated the use of this facility to study the self-assembly of block co-polymer nano-objects with a millifluidic continuous flow system (Fig. 12b).<sup>268</sup> Using acquisition times of 5 min, the authors were able to study the polymer self-assembly process over reaction times of 1 to 25 minutes controlled by adjusting the flow rate of reactants through the system and into the analysis capillary. These measurements revealed a two-step assembly process, beginning with the formation of loose hydrated aggregates between 60 and 100 s and the subsequent densification of the aggregates into well-defined spherical nano-objects over ~300–750 s (Fig. 12c).

The second platform is the Flow-XI National Facility for Analysis of Crystallization in Flow Systems located at the University of Leeds (UK).<sup>269</sup> Flow-XI is built around an X-ray diffractometer with a microfocussed rotating anode source that is also coupled to a Raman spectrometer for performing simultaneous XRD/Raman. This facility was designed specifically for performing *operando* flow-based experiments, and as such, is equipped with a range of sample environments from millifluidic flow cells and humidity chambers to microfluidic devices. Commissioning experiments on this platform performed by Turner *et al.* demonstrated its potential for studying the nucleation and growth of inorganic and organic materials from aqueous solution.<sup>269</sup> XRD and Raman yielded information on the

dynamics of both the solid phases and solution chemistry, with limits of detection of 0.02–0.1 wt% and 0.625–2.5 g L<sup>-1</sup>, respectively, depending on the materials and solution species studied. For *operando* analysis of the cooling crystallization of NaSO<sub>4</sub>, XRD and Raman acquisition times of 18 and 17 s, respectively, were found to be sufficient to obtain data with good signal-to-noise ratio.

## 6.2 X-ray spectroscopy

**6.2.1 X-ray absorption spectroscopy.** Less work has been performed on micro- and milli-fluidic laboratory-based X-ray spectroscopy compared to X-ray scattering and diffraction. Taking XAS as an example, even for *ex situ* experiments, it is still most often performed at synchrotron radiation facilities.<sup>291</sup> While laboratory-based XAS is indeed becoming more common, most *in situ* studies to date have utilized Norby-type capillary devices (see section 2.1.2).<sup>292,293</sup> Despite this, we are aware of at least one millifluidic laboratory XAS study. Kozyr *et al.* developed a 3D-printed photocatalytic cell for performing XANES with inline mass spectrometry of gas production.<sup>270</sup> This cell had two windows, one for holding a TiO<sub>2</sub> support film and performing XANES in fluorescence mode and the other for UV irradiation. The cell also had a fluid port for the injection of a Pt salt solution and a gas inlet and outlet for applying a continuous flow of Ar gas. The authors used this cell to follow the photodeposition of a Pt catalyst onto the support and its subsequent catalytic activity in a hydrogen evolution reaction. Although due to the low flux of the laboratory source, the acquisition of full XANES spectra was too slow for *operando* kinetics studies. Therefore, only three representative wavelengths (pre-edge, edge, and post-edge) were selected to follow with time.

**6.2.2 X-ray fluorescence.** XRF instruments are much more commonly found in laboratories than XAS instruments, and perhaps for this reason, there exist a few more micro- and milli-fluidic laboratory XRF studies. To the best of our knowledge, the first example comes from Miller *et al.*, who coupled a classic microfluidic capillary electrophoresis device to a benchtop micro-XRF spectrometer.<sup>271</sup> The authors demonstrated the separation and detection of a variety of metal and organic species with a comparable limit of detection ( $\sim 10^{-4}$  M) to previous synchrotron studies.<sup>151,152</sup> Greaves and Manz built a lead-lined miniaturized XRF device containing a small radioactive Am source for on-chip production of X-rays.<sup>18</sup> They analyzed the sensitivity of the device to detect various metal films inserted into the chip and obtained decent signal-to-noise ratios despite the relatively low flux of the Am source compared to standard XRF instruments. More recently, Maurice *et al.* reported an automated setup for microfluidic liquid–liquid extraction of metal waste streams using inline XRF (Fig. 13).<sup>272</sup> They demonstrated the utility of the system by performing extractions of three rare earth elements and quantifying the metal concentration within both liquid phases as a function of the fluid contact time. Olivier *et al.* followed-up this study



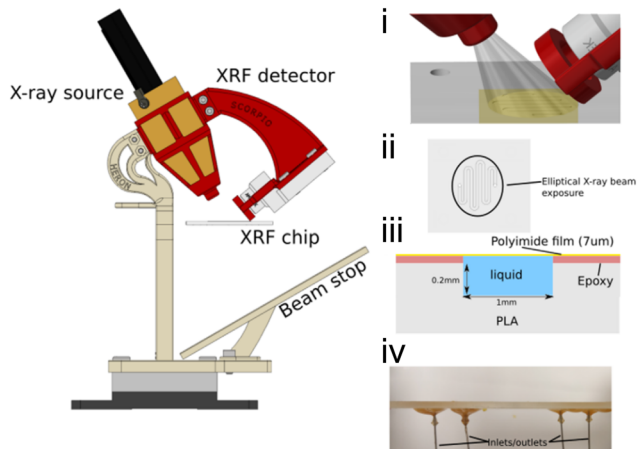


**Fig. 13** Experimental setup for laboratory-based X-ray fluorescence analysis (left). (i) View of the measurement area. (ii) Illustration of the microchannel path and the elliptical footprint of the X-ray beam. (iii) Cross-section of the microchannel. (iv) Photograph of the XRF device (used with permission from Maurice *et al.*; Copyright 2021 The Authors).<sup>272</sup>

by developing a similar millifluidic platform with inline XRF for quantifying solid-phase metal extraction.<sup>273</sup> There are additional examples of micro- and milli-fluidic laboratory-based XRF studies where 2D or 3D spatial mapping was performed, and these will be covered in the next subsection.

### 6.3 X-ray imaging

**6.3.1 Development of laboratory-based *in situ* μCT.** Similar to X-ray scattering and diffraction, there has also been a great deal of work in micro- and milli-fluidic devices for *in situ* and *operando* X-ray imaging with laboratory sources. Most of this has been focused on X-ray tomography as the small beam sizes and soft X-rays normally utilized for STXM are not readily available in the laboratory and decreased flux makes scanning techniques impractical for time-resolved experiments. Before the development of miniaturized flow cells for laboratory μCT, the wetting and diffusion dynamics within cm-scale rock samples were first analyzed in 2D with X-ray radiography<sup>294</sup> and then in 3D using X-ray tomography.<sup>295</sup> Various groups also developed new laboratory X-ray imaging instruments for visualizing flows, such as X-ray stereography setups with two perpendicular source-detector pairs for obtaining 3D information without requiring the slow tomographic rotation of a sample.<sup>296</sup> Work was also done in enabling helical-CT, where a sample is both rotated and translated vertically during tomogram acquisition to reduce beam artefacts and measure longer samples,<sup>297,298</sup> and in using gantry-based systems where the source and detector are rotated instead of the sample.<sup>298</sup> Although this list is far from exhaustive, we note in particular developments at the Center for Multiphase Flow Research and Education at Iowa State University (CoMFRE, US),<sup>296</sup> the Micro CT Facility of the Australian National University (CTLab),<sup>297,299</sup> the

Ghent University Centre for X-ray Tomography (UGCT, BE),<sup>298</sup> and the Henry Moseley X-Ray Imaging Facility at the University of Manchester (HMXIF, UK)<sup>280</sup> for improving *in situ* μCT of fluid flow.

**6.3.2 μCT for geophysical studies.** To the best of our knowledge, Youssef *et al.* performed the first *operando* flow-based laboratory μCT study.<sup>274</sup> They used a millifluidic Hassler-type cell made from PEEK to analyze an oil–water drainage/imbibition cycle within a 6 mm-diameter core of sandstone. The authors used different oil flow rates that produced equilibrium conditions within the core and visualized the various 3D fluid distributions that developed. Continued flow ensured that the fluid distribution remained relatively stationary, so that even long tomogram acquisition times of 80 minutes could reliably capture different steps in the drainage/imbibition cycle. Andrew *et al.* performed a similar experiment using a high-pressure Hassler flow cell to study geological CO<sub>2</sub> sequestration in limestone.<sup>275</sup> In this experiment, 2D projections were collected continuously during the injection of super-critical CO<sub>2</sub> until reaching steady-state, at which point a full tomogram was acquired. The authors later expanded their study to analyze the trapping of super-critical CO<sub>2</sub> in a range of different rocks<sup>276</sup> and worked to quantify wetting in the three-phase CO<sub>2</sub>–brine–limestone system by extracting contact angles from 2D slices of tomograms.<sup>277</sup> Bultreys *et al.* performed the first laboratory-based fast-μCT study of flow within porous media.<sup>278</sup> Using a gantry-based system with a microfocus X-ray source and CMOS detector, the authors were able to acquire full tomograms within 12 s with a voxel size of ~15 μm. Data quality at this fast speed was improved using information on the sample obtained *a priori* from a higher resolution tomogram collected under equilibrium conditions.

**6.3.3 μCT for geochemical studies.** As for synchrotron-based studies, laboratory-based μCT studies have also investigated geochemical processes occurring within porous media. For example, Menke *et al.* used a millifluidic Hassler cell to study the dissolution of a limestone core during the injection of a CO<sub>2</sub>-saturated brine at 50 °C and 10 MPa.<sup>279</sup> They followed the dissolution of the pores over ~2.5 hours with a spatial and temporal resolution of 3.8 μm and 15 minutes, respectively. Gajjar *et al.* studied the precipitation of barite within a microporous glass column.<sup>280</sup> The authors used an innovative approach in which projections were acquired at angles calculated by the golden-ratio rather than sampling at equally spaced angles around the sample. While taking longer to acquire each projection, this approach required fewer projections to reconstruct a tomogram. In this way, the authors tried to find a protocol that optimized the spatial and temporal resolution of tomograms. Godinho *et al.* used a similar microporous column to study calcite precipitation and performed the first *operando* helical-CT study of flow in porous media.<sup>281</sup> They followed the slow growth of calcite over 17 days with nine tomograms collected at different times, each taking 2.5 hours. More recently, Singh *et al.* performed a μCT study of calcite dissolution with

a tomogram acquisition time of 83 s and a voxel size of 19.3  $\mu\text{m}$ .<sup>282</sup>

**6.3.4 Tomographic X-ray PIV/PTV.** Before 3D tomographic X-ray particle image velocimetry (PIV) or particle tracking velocimetry (PTV) was performed at the synchrotron, at least two groups implemented it with a laboratory source. Mäkiharju *et al.* performed a proof-of-concept study by analyzing a creeping flow of 60  $\mu\text{m}$  diameter tracer particles within a single-phase pipe flow, a microporous glass column, and a thin liquid film around a flow of gas slugs (Fig. 14).<sup>283</sup> In each case, the cylindrical flow channel was continuously rotated at  $\sim$ 20 rpm while projections were acquired at 68 Hz (14.5 ms per projection) and full tomograms completed in  $\sim$ 3 seconds. As the tracer particles were moving at only  $\sim$ 20–50  $\mu\text{m s}^{-1}$  in the pipe flow, the authors could collect high contrast projections with negligible blur and use standard PIV/PTV algorithms to obtain the 3D velocity fields. However, the flow constrictions in the other two cases increased the flow velocity, so that only particles that had become stuck could be resolved. Bultreys *et al.* performed a similar analysis of a creeping flow within porous media and successfully resolved the flowing particles to extract the 3D velocity field.<sup>284</sup> While they used a slower scan speed of 100 ms per projection and 70 s for acquiring a full tomogram, they utilized flow rates of only tens of nanoliters per minute that produced particle velocities of  $\sim$ 100–200  $\mu\text{m s}^{-1}$ . They also utilized a filtered backprojection algorithm during reconstruction that interleaved data between two consecutive tomograms, effectively decreasing the time step between tomograms to 35 s. Together, the flow rates and reconstruction methods meant that, on average, particles moved only 0.5 voxels between frames providing a sufficient resolution for particle tracking. Despite this progress, it is

clear that laboratory-based 3D X-ray PIV can only follow slow flow dynamics, and its time resolution cannot compare to subsequent work in synchrotron-based X-ray PIV (see section 5.3.2).

**6.3.5 XRF mapping.** There has been some limited work in laboratory-based  $\mu$ XRF for *in situ* microfluidic chemical mapping. Tsuji *et al.* developed microfluidic chips for concentrating medical and environmental samples for elemental analysis with a benchtop XRF spectrometer.<sup>285</sup> They developed two chips, one for preparing samples for grazing-incidence XRF and one for scanning  $\mu$ XRF. In the case of  $\mu$ XRF, the authors demonstrated that a nL sample of solution containing just nanograms of Cu, Cd, and Fe could be concentrated, dried, and then mapped on-chip. Subsequently, Nakano and Tsuji performed confocal 3D-XRF on a multi-layer polymer microfluidic device containing separate microchannels within the different layers.<sup>286</sup> To demonstrate the method, they filled one channel with a Cu solution and one with a Co solution (both 3 mg  $\text{mL}^{-1}$ ) and obtained a 3D map that distinguished both channels with elemental selectivity. Finally, McIntosh *et al.* developed a polycarbonate-Kapton microfluidic device for monitoring Pu concentrations in nuclear waste.<sup>287</sup> Using Sr as a surrogate for Pu due to its similar fluorescent signature, the authors demonstrated that chips could be filled directly from a micropipette with 5  $\mu\text{L}$  of solution and subsequently mapped for their Sr content with a limit of detection of  $\sim$ 5 ppm.

## 7 Discussion and outlook

The numerous examples cited in this review demonstrate the huge interest in using micro/millifluidics to carry out *in situ* and *operando* X-ray analyzes in both liquids and gases. We

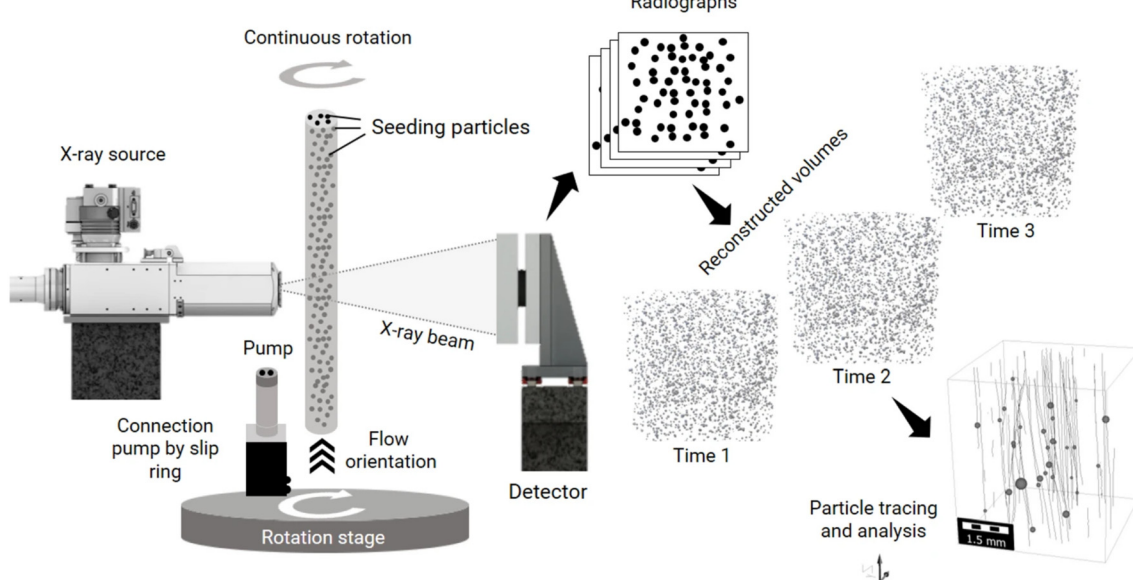


**Fig. 14** Experimental setup for laboratory-based 3D tomographic X-ray particle tracking velocimetry of a creeping millifluidic flow (used with permission from Mäkiharju *et al.*; Copyright 2021 The Authors).<sup>283</sup>



have seen that there is interest across all types of X-ray analysis, whether scattering, spectroscopy, or imaging and using both synchrotron and laboratory sources. In total, we have reviewed 148 articles (139 explicitly found in Tables 1–4), which we believe represents a near-comprehensive account of micro- and milli-fluidic X-ray literature in the physical sciences from the year 1999 until 2023. The growth in the number of articles produced is clear (Fig. 15), where the average number of papers produced per year from 1999 to 2015 was ~4 and the number per year since the life sciences review of Ghazal *et al.*<sup>12</sup> in 2016 is ~10.

There is good reason for this high and growing level of interest. Specifically for continuous flow devices, the renewal of fluid under the beam has several advantages for X-ray measurements, including increasing their temporal resolution. In continuous flow, time resolution does not depend on the frame rate of a detector, but rather on the time it takes for fluid to pass through the beam and, therefore, on the linear velocity of the fluid as well as the beam size (and, in certain cases, on the initial mixing processes). Inline fluidic devices also make it possible to reduce the aging time of the sample before analysis by eliminating the step of introducing the sample under beam. This both reduces the observation dead time while guaranteeing the repeatability of measurements, *e.g.*, by eliminating sample preparation artefacts. Using an inline fluidic configuration can also increase the rate at which samples can be measured thanks to the possibility of changing the nature of the sample (*e.g.*, flow rate ratio, temperature) without a disassembly/reassembly operation, a particularly time-consuming process for techniques requiring operation under vacuum. This time saving makes it possible to accelerate data collection and even consider performing large screening studies. Finally, the continuous renewal of the sample under an ionizing beam limits the effects of radiation damage.

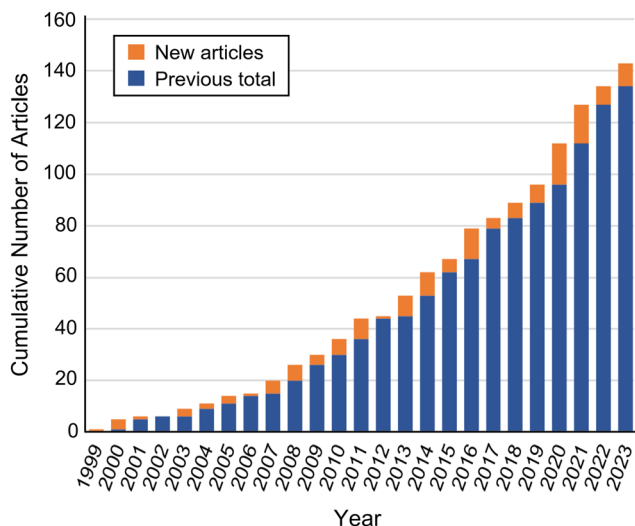


Fig. 15 Chronology of the articles covered in this review (excluding articles from 2024).

The size reduction associated with microfluidic devices adds further advantages to the previous list. It makes it possible to reduce the necessary sample volumes by one or more orders of magnitude, to carry out transmission analysis of highly absorbing samples (crucial in the soft X-ray domain), to access reaction times of less than a millisecond due to very efficient mixing functions at the micro-scale, and more generally, to combine many types of sample manipulation (*e.g.*, droplet generation, separation, heating) into a single platform. It also results in an increase in the surface area-to-volume ratio, which can be a significant advantage when the objective is to probe the interactions between the substrate of the device and the objects conveyed by the flow, for instance, in catalysis studies. This increase of surface effects can, however, also constitute a point of weakness when uncontrolled events of adsorption and/or heterogeneous nucleation on the walls of a microchannel obscure or alter the bulk phenomena of interest.<sup>102</sup>

Initially condensing into a field of research in its own right,<sup>96</sup> microfluidics quickly became a formidable tool for manipulating samples in domains as varied as biology, clinical diagnostics, synthetic chemistry, and materials science.<sup>83,84,300,301</sup> Many research groups and companies have found success in applying microfluidic tools to these various areas. However, “going microfluidic” normally requires a large investment in equipment and technical skill, and this has been no different for groups looking to use fluidic devices for *in situ* X-ray analysis. In our opinion, perhaps the greatest bottleneck here has been in the complex microfabrication techniques and specific environments required for making conventional microfluidic devices. Such environments, of the “cleanroom” type, are characterized by a very low concentration of particles in the air as well as controlled temperature and relative humidity. Various specific equipment, such as spin-coaters, UV mask aligners, and plasma cleaners are also necessary. The investment, both in terms of cost and manpower, needed to establish such an environment cannot, therefore, be justified when its use is only occasional. This strongly hinders the uptake of microfluidics by non-specialist laboratories.

Fortunately, this barrier is continually being lowered due to the increasing availability of commercial solutions and the development of more accessible methods in microfabrication. Some companies (*e.g.*, Microfluidic ChipShop, Micronit, Protochips) offer turnkey microfluidic devices associated with different fluidic functions such as droplet production, mixing, and electrochemistry. This solution thus relieves the user of any microfabrication duties and might only require access to a laminar flow hood to guarantee sufficient cleanliness when setting up the fluidic system. Indeed, many of the studies reviewed herein were performed with commercially available components or completely commercial chips, for example, ref. 160, 165 and 287 and several others.

At the same time, microfabrication is beginning to require less expertise due to new technologies that reduce the



number of fabrication steps and guarantee very good device reproducibility and reliability. For photolithographic cleanroom-based fabrication, the use of commercial polymer films (*i.e.*, dry film photoresists) of calibrated thickness for the creation of molds avoids the production of photoresist films by spin-coating, the result of which strongly depends on the temperature and humidity of the laboratory.<sup>302</sup> Many non-cleanroom routes are also available. The use of hot embossable materials such as cyclic olefin copolymers (*e.g.*, TOPAS®) or cyclic olefin polymers (*e.g.*, ZEONOR®, ZEONEX®) makes it possible to replicate the same device many times in an automated and repeatable manner.<sup>303,304</sup> The use of laser micromachining makes it possible to produce monolithic devices from many types of materials and/or to produce “sandwich”-type devices combining different materials, again in an automated manner.<sup>102,305,306</sup> The main challenge with the high-performing femtosecond laser machining platforms required for patterning small features in a large range of materials is that their cost is on the scale of large cleanroom equipment. Much less expensive, 3D printing now makes it possible to directly print devices with minimum channel sizes below 100  $\mu\text{m}$  using commercial printers with minimal to no modifications.<sup>125,307</sup> Indeed, a large number of the studies used here were performed with 3D-printed components or chips (*e.g.*, ref. 131, 216 and 266). Further, the adoption of simple plug-and-play millifluidic devices or millifluidic devices with lower requirements in manufacturing precision can still produce excellent data (see ref. 127, 262 and 273 for example). The multiplicity of available fabrication techniques now enables one to be more selective in the choice of device material to optimize key parameters such as its X-ray absorption or scattering profile or even its degradation under irradiation. For example, in our laboratory, where we perform a variety of different X-ray techniques for different types of samples, we have investigated every process mentioned above and found them all to be useful depending on the technique requirements and demands of the particular experiment.

These developments should ultimately encourage the use of micro- and milli-fluidic sample environments for *in situ* characterization at the synchrotron and in the laboratory. Until very recently, synchrotron studies conducted with microfluidic devices produced relatively little data due to the numerous technical challenges encountered during their implementation. Their handling, already delicate, is made even more difficult at the synchrotron and away from one's own laboratory environment. Consequently, journal publications only reflect a small part of the real effort made by the scientific community to develop micro- and milli-fluidic tools that better exploit the potential of X-ray analysis. For their part, synchrotron facilities have largely participated in this effort by developing microfocused beams compatible with the typical size of microfluidic channels (typically hundreds of microns). Many synchrotron facilities have also formed dedicated teams to help users with sample preparation in general, or microfluidics in particular, such as

the Partnership for Soft Condensed Matter at the ESRF,<sup>125</sup> the Microfluidic Laboratory at SOLEIL,<sup>227</sup> and the Sample Environment Development Laboratory at Diamond Light Source.

Additional actions on their part could further facilitate micro- and milli-fluidic experiments. These include the installation of “clean” zones in the form of laminar flow hoods or biosafety cabinets (ISO 7 or 5)—essential for the preparation of the devices before experiments—near the beamline experimental hutch, the provision of commercial microfluidic environments already tested and integrated by the beamline staff, and the inclusion of inline optical microscopes for the visualization of microfluidic channels and the identification of measurement points. To our knowledge, automated or remote access to microfluidic equipment has not yet been implemented at a synchrotron beamline. However, this has been demonstrated for stopped-flow devices at bioSAXS beamlines (*e.g.*, SSRL 4.2, PETRA III P12) and may be possible in the future for continuous flow micro- and milli-fluidic platforms for greater accessibility.

There are also several things beamline users can do to increase the success rate of their microfluidics beamtimes. The first is ensuring that the devices they bring are safe and reliable, *e.g.*, not prone to leaking on expensive beamline hardware. Beamline staff have invested significant time in building their unique instruments and must continue to devote time to hosting user experiments. When users come with unreliable devices that do not produce data and thus, do not produce papers, they are less enthusiastic about recommending future microfluidics experiments. We have seen above that there are many routes to making robust micro- and milli-fluidic devices. We have also seen in section 6 that laboratory-based analysis is becoming more and more feasible. For this reason, we recommend that potential users try to perform an experiment with a laboratory instrument before applying for synchrotron beamtime. For example, the Sample Environment Development Laboratory at Diamond even offers this opportunity in partnership with beamline I22 and their offline SAXS platform.<sup>268</sup> Even if an experiment is not feasible with the lower flux of a laboratory source, using a laboratory instrument to first characterize the scattering/absorption of a device such as done by Lange *et al.*<sup>92</sup> or practicing the mounting of a device to avoid any potential surprises at a beamtime can go a long way.

X-ray analysis techniques, whether performed with a synchrotron or a laboratory source, are powerful tools for structural and chemical characterization. When combined with a micro- or milli-fluidic sample environment, they offer unparalleled possibilities for *in situ* and *operando* studies. The combination makes it possible, on one hand, to eliminate the preparation artifacts inherent in post-mortem analyses, and substantially improves, on the other hand, the temporal resolution compared to studies in a static configuration (*i.e.*, without fluid renewal). However, while synchrotron light sources have long been and will continue to be a powerful tool in the arsenal of crystallographers and



chemists, the relative inaccessibility of these facilities does limit the progress of individual research teams, which could otherwise measure more samples, develop more robust workflows, and iterate more rapidly. It is here we see tremendous potential for the current generation of commercial laboratory X-ray instruments, not just to permit more efficient use of synchrotron beamtime, but also to support completely independent *in situ* flow-based analysis platforms (see section 6.1.5).

Perhaps the most innovative prospect in the use of micro- and milli-fluidic X-ray sample environments is the possibility of exercising feedback control over the injected reagents, temperature, or other reaction conditions. Real-time analysis of data coupled with machine learning, as demonstrated by Fong *et al.*<sup>111</sup> and Younes *et al.*<sup>112</sup> for SAXS (section 3.2.3), makes it possible to direct the system towards a state corresponding to a pre-defined structural or chemical parameter. For example, in the field of (nano)materials synthesis, this ability should facilitate a departure from the classical trial-and-error approach and guarantee both the outcome of the syntheses and their reproducibility. Another recent study reported an autonomous laboratory for the high temperature synthesis of solid powders and their characterization by XRD.<sup>308</sup> We could envision a similar type of system,<sup>309</sup> but one using XRD/SAXS analysis for automated liquid phase synthesis with a micro- or milli-fluidic device benefiting from all of the advantages discussed above. The industrial value of such a paradigm shift would be considerable. Thus, making these techniques more accessible to the point of being routine, both at the synchrotron and in the laboratory, is a worthwhile effort not only for gaining fundamental scientific understanding, but also for developing new materials and processes for industrial and societal use.

## Data availability

No primary research results, software or code have been included and no new data were generated or analysed as part of this review.

## Author contributions

MAL conceived the idea for the review and refined the concept in discussions with all authors. MAL performed the literature survey for sections 2, 3, 4, and 6. MAL and CC performed the literature survey for section 5. MAL wrote the manuscript with contributions from CC. MAL and CC edited the manuscript. FM, FT, and OT provided feedback in their areas of expertise.

## Conflicts of interest

There are no conflicts to declare.

## Acknowledgements

This work received state support managed by the French National Research Agency (ANR) under the France 2030 framework (ANR-22-PEXD-0006 and ANR-22-PEXD-0007). The authors would like to thank the many beamline scientists and staff who have supported their micro- and milli-fluidics beamtimes over the years, with a special mention of Sarah Day, Chiu Tang, Manfred Burghammer, Javier Perez, Thomas Bizien, Stefan Stanescu, Rachid Belkhoud, Diego Pontoni, and Peter van der Linden. We also thank our editor, David Lake, for his assistance and patience during the preparation of the review.

## References

- 1 J. J. De Yoreo, P. U. P. A. Gilbert, N. A. J. M. Sommerdijk, R. L. Penn, S. Whitelam, D. Joester, H. Zhang, J. D. Rimer, A. Navrotsky, J. F. Banfield, A. F. Wallace, F. M. Michel, F. C. Meldrum, H. Cölfen and P. M. Dove, *Science*, 2015, **349**, aaa6760.
- 2 A. E. S. Van Driessche, N. Van Gerven, P. H. H. Bomans, R. R. M. Joosten, H. Friedrich, D. Gil-Carton, N. Sommerdijk and M. Sleutel, *Nature*, 2018, **556**, 89–94.
- 3 Z. Gao, M. Odstrcil, S. Böcklein, D. Palagin, M. Holler, D. F. Sanchez, F. Krumeich, A. Menzel, M. Stampanoni, G. Mestl, J. A. van Bokhoven, M. Guizar-Sicairos and J. Ihli, *Sci. Adv.*, 2021, **7**, eabf6971.
- 4 M. Macino, A. J. Barnes, S. M. Althahban, R. Qu, E. K. Gibson, D. J. Morgan, S. J. Freakley, N. Dimitratos, C. J. Kiely, X. Gao, A. M. Beale, D. Bethell, Q. He, M. Sankar and G. J. Hutchings, *Nat. Catal.*, 2019, **2**, 873–881.
- 5 D. P. Finegan, M. Scheel, J. B. Robinson, B. Tjaden, I. Hunt, T. J. Mason, J. Millichamp, M. Di Michiel, G. J. Offer, G. Hinds, D. J. L. Brett and P. R. Shearing, *Nat. Commun.*, 2015, **6**, 6924.
- 6 S. N. S. Hapuarachchi, Z. Sun and C. Yan, *Adv. Sustainable Syst.*, 2018, **2**, 1700182.
- 7 Z. Ning, D. S. Jolly, G. Li, R. De Meyere, S. D. Pu, Y. Chen, J. Kasemchainan, J. Ihli, C. Gong, B. Liu, D. L. R. Melvin, A. Bonnin, O. Magdysyuk, P. Adamson, G. O. Hartley, C. W. Monroe, T. J. Marrow and P. G. Bruce, *Nat. Mater.*, 2021, **20**, 1121–1129.
- 8 D. H. Bilderback, P. Elleaume and E. Weckert, *J. Phys. B*, 2005, **38**, S773.
- 9 H. Weise and W. Decking, presented in part at the *38th International Free Electron Laser Conference, FEL2017*, Santa Fe, NM, USA, 2017.
- 10 S. Shin, *AAPPS Bull.*, 2021, **31**, 21.
- 11 T. Skarzynski, *Acta Crystallogr., Sect. D: Biol. Crystallogr.*, 2013, **69**, 1283–1288.
- 12 A. Ghazal, J. P. Lafleur, K. Mortensen, J. P. Kutter, L. Arleth and G. V. Jensen, *Lab Chip*, 2016, **16**, 4263–4295.
- 13 M. A. Bañares, *Catal. Today*, 2005, **100**, 71–77.
- 14 M. Ilett, M. Afzali, B. Abdulkarim, Z. Aslam, S. Foster, M. Burgos-Ruiz, Y.-Y. Kim, F. C. Meldrum and R. M. Drummond-Brydson, *J. Microsc.*, 2024, **1–14**, DOI: [10.1111/jmi.13300](https://doi.org/10.1111/jmi.13300).

15 M. A. Levenstein, K. Robertson, T. D. Turner, L. Hunter, C. O'Brien, C. O'Shaughnessy, A. N. Kulak, P. Le Magueres, J. Wojciechowski, O. O. Mykhaylyk, N. Kapur and F. C. Meldrum, *IUCrJ*, 2022, **9**, 538–543.

16 C. L. Hansen, E. Skordalakes, J. M. Berger and S. R. Quake, *Proc. Natl. Acad. Sci. U. S. A.*, 2002, **99**, 16531–16536.

17 B. Zheng, J. D. Tice, L. S. Roach and R. F. Ismagilov, *Angew. Chem., Int. Ed.*, 2004, **43**, 2508–2511.

18 E. D. Greaves and A. Manz, *Lab Chip*, 2005, **5**, 382–391.

19 E. Lawrence Bright, C. Giacobbe and J. P. Wright, *J. Synchrotron Radiat.*, 2021, **28**, 1377–1385.

20 U. Weierstall, *Philos. Trans. R. Soc., B*, 2014, **369**, 20130337.

21 S. Sui and S. L. Perry, *Struct. Dyn.*, 2017, **4**, 032202.

22 L. Paulson, S. R. Narayanasamy, M. L. Shelby, M. Frank and M. Trebbin, *Struct. Dyn.*, 2024, **11**, 011101.

23 I. Grillo, *Curr. Opin. Colloid Interface Sci.*, 2009, **14**, 402–408.

24 J. T. Avaro, S. L. P. Wolf, K. Hauser and D. Gebauer, *Angew. Chem., Int. Ed.*, 2020, **59**, 6155–6159.

25 R. J. Clarke and M. A. A. Khalid, in *Pumps, Channels, and Transporters*, 2015, pp. 179–209, DOI: [10.1002/9781119085126.ch7](https://doi.org/10.1002/9781119085126.ch7).

26 O. L. J. Virtanen, M. Kather, J. Meyer-Kirschner, A. Melle, A. Radulescu, J. Viell, A. Mitsos, A. Pich and W. Richtering, *ACS Omega*, 2019, **4**, 3690–3699.

27 S. Schmöller, D. Gräbner, M. Gradzielski and T. Narayanan, *Phys. Rev. Lett.*, 2002, **88**, 258301.

28 G. Guilera, M. A. Newton, C. Polli, S. Pascarelli, M. Guinó and K. K. Hii, *Chem. Commun.*, 2006, **41**, 4306–4308.

29 B. Abécassis, F. Testard, O. Spalla and P. Barboux, *Nano Lett.*, 2007, **7**, 1723–1727.

30 J. Polte, T. T. Ahner, F. Delissen, S. Sokolov, F. Emmerling, A. F. Thünemann and R. Krahnert, *J. Am. Chem. Soc.*, 2010, **132**, 1296–1301.

31 T. M. Stawski, A. E. S. van Driessche, M. Ossorio, J. Diego Rodriguez-Blanco, R. Besseling and L. G. Benning, *Nat. Commun.*, 2016, **7**, 11177.

32 M. L. Whittaker, P. J. M. Smeets, H. Asayesh-Ardakani, R. Shahbazian-Yassar and D. Joester, *Angew. Chem., Int. Ed.*, 2017, **56**, 16028–16031.

33 J. Bolze, B. Peng, N. Dingenaouts, P. Panine, T. Narayanan and M. Ballauff, *Langmuir*, 2002, **18**, 8364–8369.

34 J. Cravillon, C. A. Schroder, R. Nayuk, J. Gummel, K. Huber and M. Wiebcke, *Angew. Chem., Int. Ed.*, 2011, **50**, 8067–8071.

35 F. Carraro, J. D. Williams, M. Linares-Moreau, C. Parise, W. Liang, H. Amenitsch, C. Doonan, C. O. Kappe and P. Falcaro, *Angew. Chem., Int. Ed.*, 2020, **59**, 8123.

36 M. J. Quayle, R. J. Davey, A. J. McDermott, G. J. T. Tiddy, D. T. Clarke and G. R. Jones, *Phys. Chem. Chem. Phys.*, 2002, **4**, 416–418.

37 P. J. Chupas, K. W. Chapman, C. A. Kurtz, J. C. Hanson, P. L. Lee and C. P. Grey, *J. Appl. Crystallogr.*, 2008, **41**, 822–824.

38 C. G. Roessler, R. Agarwal, M. Allaire, R. Alonso-Mori, B. Andi, J. F. R. Bachega, M. Bommer, A. S. Brewster, M. C. Browne, R. Chatterjee, E. Cho, A. E. Cohen, M. Cowan, S. Datwani, V. L. Davidson, J. Defever, B. Eaton, R. Ellson, Y. Feng, L. P. Ghislain, J. M. Glownia, G. Han, J. Hattne, J. Hellmich, A. Héroux, M. Ibrahim, J. Kern, A. Kuczewski, H. T. Lemke, P. Liu, L. Majlof, W. M. McClintock, S. Myers, S. Nelsen, J. Olechno, A. M. Orville, N. K. Sauter, A. S. Soares, S. M. Soltis, H. Song, R. G. Stearns, R. Tran, Y. Tsai, M. Uervirojnakorn, C. M. Wilmot, V. Yachandra, J. Yano, E. T. Yukl, D. Zhu and A. Zouni, *Structure*, 2016, **24**, 631–640.

39 R. H. Morris, E. R. Dye, D. Axford, M. I. Newton, J. H. Beale and P. T. Docker, *Sci. Rep.*, 2019, **9**, 12431.

40 B. Chance, *Rev. Sci. Instrum.*, 1951, **22**, 619–627.

41 R. L. Berger, B. Balko and H. F. Chapman, *Rev. Sci. Instrum.*, 1968, **39**, 493–498.

42 P. Panine, S. Finet, T. M. Weiss and T. Narayanan, *Adv. Colloid Interface Sci.*, 2006, **127**, 9–18.

43 L. Matthews and T. Narayanan, *Colloid Polym. Sci.*, 2023, **301**, 721–728.

44 A. Zabilska, A. H. Clark, D. Ferri, M. Nachtegaal, O. Kröcher and O. V. Safonova, *Phys. Chem. Chem. Phys.*, 2022, **24**, 21916–21926.

45 C. K. Christensen, M. A. Karlsen, A. O. Drejer, B. P. Andersen, C. L. Jakobsen, M. Johansen, D. R. Sorensen, I. Kantor, M. R. V. Jorgensen and D. B. Ravnsbaek, *J. Synchrotron Radiat.*, 2023, **30**, 561–570.

46 P. Norby, *Mater. Sci. Forum*, 1996, **228–231**, 147–152.

47 R. Hodyss, T. H. Vu, M. Choukroun and M. L. Cable, *J. Appl. Crystallogr.*, 2021, **54**, 1268–1270.

48 B. S. Clausen, G. Steffensen, B. Fabius, J. Villadsen, R. Feidenhans'l and H. Topsøe, *J. Catal.*, 1991, **132**, 524–535.

49 P. Norby, *J. Am. Chem. Soc.*, 1997, **119**, 5215–5221.

50 K. M. O. Jensen, H. L. Andersen, C. Tyrsted, E. D. Bojesen, A. C. Dippel, N. Lock, S. J. L. Billinge, B. B. Iversen and M. Christensen, *ACS Nano*, 2014, **8**, 10704–10714.

51 J. A. Rodriguez, X. Wang, P. Liu, W. Wen, J. C. Hanson, J. Hrbek, M. Pérez and J. Evans, *Top. Catal.*, 2007, **44**, 73–81.

52 T. R. Jensen, T. K. Nielsen, Y. Filinchuk, J.-E. Jorgensen, Y. Cerenius, E. M. Gray and C. J. Webb, *J. Appl. Crystallogr.*, 2010, **43**, 1456–1463.

53 N. V. Y. Scarlett, D. Hewish, R. Pattel and N. A. S. Webster, *Rev. Sci. Instrum.*, 2017, **88**, 105104.

54 T.-D. Nguyen-Phan, Z. Liu, S. Luo, A. D. Gamalski, D. Vovchok, W. Xu, E. A. Stach, D. E. Polyansky, E. Fujita, J. A. Rodriguez and S. D. Senanayake, *J. Phys. Chem. C*, 2016, **120**, 3472–3482.

55 J. Becker, M. Bremholm, C. Tyrsted, B. Pauw, K. M. O. Jensen, J. Eltzholz, M. Christensen and B. B. Iversen, *J. Appl. Crystallogr.*, 2010, **43**, 729–736.

56 P. Ferrer, I. da Silva, J. Rubio-Zuazo, B. F. Alfonso, C. Trobajo, S. Khainakov, J. R. Garcia, S. Garcia-Granda and G. R. Castro, *J. Synchrotron Radiat.*, 2012, **19**, 93–100.

57 H. N. Chapman, P. Fromme, A. Barty, T. A. White, R. A. Kirian, A. Aquila, M. S. Hunter, J. Schulz, D. P. DePonte, U. Weierstall, R. B. Doak, F. Maia, A. V. Martin, I. Schlichting,



L. Lomb, N. Coppola, R. L. Shoeman, S. W. Epp, R. Hartmann, D. Rolles, A. Rudenko, L. Foucar, N. Kimmel, G. Weidenspointner, P. Holl, M. N. Liang, M. Barthelmess, C. Caleman, S. Boutet, M. J. Bogan, J. Krzywinski, C. Bostedt, S. Bajt, L. Gumprecht, B. Rudek, B. Erk, C. Schmidt, A. Homke, C. Reich, D. Pietschner, L. Struder, G. Hauser, H. Gorke, J. Ullrich, S. Herrmann, G. Schaller, F. Schopper, H. Soltau, K. U. Kuhnel, M. Messerschmidt, J. D. Bozek, S. P. Hau-Riege, M. Frank, C. Y. Hampton, R. G. Sierra, D. Starodub, G. J. Williams, J. Hajdu, N. Timneanu, M. M. Seibert, J. Andreasson, A. Rocker, O. Jonsson, M. Svenda, S. Stern, K. Nass, R. Andritschke, C. D. Schroter, F. Krasnqi, M. Bott, K. E. Schmidt, X. Y. Wang, I. Grotjohann, J. M. Holton, T. R. M. Barends, R. Neutze, S. Marchesini, R. Fromme, S. Schorb, D. Rupp, M. Adolph, T. Gorkhover, I. Andersson, H. Hirsemann, G. Potdevin, H. Graafsma, B. Nilsson and J. C. H. Spence, *Nature*, 2011, **470**, U73–U81.

58 D. P. DePonte, U. Weierstall, K. Schmidt, J. Warner, D. Starodub, J. C. H. Spence and R. B. Doak, *J. Phys. D: Appl. Phys.*, 2008, **41**, 195505.

59 M. O. Wiedorn, D. Oberthur, R. Bean, R. Schubert, N. Werner, B. Abbey, M. Aepfelbacher, L. Adriano, A. Allahgholi, N. Al-Qudami, J. Andreasson, S. Aplin, S. Awel, K. Ayyer, S. Bajt, I. Barak, S. Bari, J. Bielecki, S. Botha, D. Boukhelef, W. Brehm, S. Brockhauser, I. Cheviakov, M. A. Coleman, F. Cruz-Mazo, C. Danilevski, C. Darmanin, R. B. Doak, M. Domaracky, K. Dorner, Y. Du, H. Fangohr, H. Fleckenstein, M. Frank, P. Fromme, A. M. Ganan-Calvo, Y. Gevorkov, K. Giewekemeyer, H. M. Ginn, H. Graafsma, R. Graceffa, D. Greiffenberg, L. Gumprecht, P. Gottlicher, J. Hajdu, S. Hauf, M. Heymann, S. Holmes, D. A. Horke, M. S. Hunter, S. Imlau, A. Kaukher, Y. Kim, A. Klyuev, J. Knoska, B. Kobe, M. Kuhn, C. Kupitz, J. Kuper, J. M. Lahey-Rudolph, T. Laurus, K. Le Cong, R. Letrun, P. L. Xavier, L. Maia, F. Maia, V. Mariani, M. Messerschmidt, M. Metz, D. Mezza, T. Michelat, G. Mills, D. C. F. Monteiro, A. Morgan, K. Muhlig, A. Munke, A. Munnich, J. Nette, K. A. Nugent, T. Nuguid, A. M. Orville, S. Pandey, G. Pena, P. Villanueva-Perez, J. Poehls, G. Previtali, L. Redecke, W. M. Riekehr, H. Rohde, A. Round, T. Safenreiter, I. Sarrou, T. Sato, M. Schmidt, B. Schmitt, R. Schonherr, J. Schulz, J. A. Sellberg, M. M. Seibert, C. Seuring, M. L. Shelby, R. L. Shoeman, M. Sikorski, A. Silenzi, C. A. Stan, X. T. Shi, S. Stern, J. Sztuk-Dambietz, J. Szuba, A. Tolstikova, M. Trebbin, U. Trunk, P. Vagovic, T. Ve, B. Weinhausen, T. A. White, K. Wrona, C. Xu, O. Yefanov, N. Zatsepin, J. G. Zhang, M. Perbandt, A. P. Mancuso, C. Betzel, H. Chapman and A. Barty, *Nat. Commun.*, 2018, **9**, 11.

60 U. Weierstall, D. James, C. Wang, T. A. White, D. Wang, W. Liu, J. C. H. Spence, R. Bruce Doak, G. Nelson, P. Fromme, R. Fromme, I. Grotjohann, C. Kupitz, N. A. Zatsepin, H. Liu, S. Basu, D. Wacker, G. Won Han, V. Katritch, S. Boutet, M. Messerschmidt, G. J. Williams, J. E. Koglin, M. Marvin Seibert, M. Klinker, C. Gati, R. L. Shoeman, A. Barty, H. N. Chapman, R. A. Kirian, K. R. Beyerlein, R. C. Stevens, D. Li, S. T. A. Shah, N. Howe, M. Caffrey and V. Cherezov, *Nat. Commun.*, 2014, **5**, 3309.

61 K. R. Beyerlein, H. O. Jönsson, R. Alonso-Mori, A. Aquila, S. Bajt, A. Barty, R. Bean, J. E. Koglin, M. Messerschmidt, D. Ragazzon, D. Sokaras, G. J. Williams, S. Hau-Riege, S. Boutet, H. N. Chapman, N. Timneanu and C. Caleman, *Proc. Natl. Acad. Sci. U. S. A.*, 2018, **115**, 5652–5657.

62 J. A. Sellberg, C. Huang, T. A. McQueen, N. D. Loh, H. Laksmono, D. Schlesinger, R. G. Sierra, D. Nordlund, C. Y. Hampton, D. Starodub, D. P. DePonte, M. Beye, C. Chen, A. V. Martin, A. Barty, K. T. Wilkfeldt, T. M. Weiss, C. Caronna, J. Feldkamp, L. B. Skinner, M. M. Seibert, M. Messerschmidt, G. J. Williams, S. Boutet, L. G. M. Pettersson, M. J. Bogan and A. Nilsson, *Nature*, 2014, **510**, 381–384.

63 H. Laksmono, T. A. McQueen, J. A. Sellberg, N. D. Loh, C. Huang, D. Schlesinger, R. G. Sierra, C. Y. Hampton, D. Nordlund, M. Beye, A. V. Martin, A. Barty, M. M. Seibert, M. Messerschmidt, G. J. Williams, S. Boutet, K. Amann-Winkel, T. Loerting, L. G. M. Pettersson, M. J. Bogan and A. Nilsson, *J. Phys. Chem. Lett.*, 2015, **6**, 2826–2832.

64 E. A. Schriber, D. W. Paley, R. Bolotovsky, D. J. Rosenberg, R. G. Sierra, A. Aquila, D. Mendez, F. Poitevin, J. P. Blaschke, A. Bhowmick, R. P. Kelly, M. Hunter, B. Hayes, D. C. Popple, M. Yeung, C. Pareja-Rivera, S. Lisova, K. Tono, M. Sugahara, S. Owada, T. Kuykendall, K. Yao, P. J. Schuck, D. Solis-Ibarra, N. K. Sauter, A. S. Brewster and J. N. Hohman, *Nature*, 2022, **601**, 360–365.

65 F. Lehmkühler, F. Dallari, A. Jain, M. Sikorski, J. Möller, L. Frenzel, I. Lokteva, G. Mills, M. Walther, H. Sinn, F. Schulz, M. Dartsch, V. Markmann, R. Bean, Y. Kim, P. Vagovic, A. Madsen, P. Mancuso, Adrian and G. Grübel, *Proc. Natl. Acad. Sci. U. S. A.*, 2020, **117**, 24110–24116.

66 A. Aquila, M. S. Hunter, R. B. Doak, R. A. Kirian, P. Fromme, T. A. White, J. Andreasson, D. Arnlund, S. Bajt, T. R. M. Barends, M. Barthelmess, M. J. Bogan, C. Bostedt, H. Bottin, J. D. Bozek, C. Caleman, N. Coppola, J. Davidsson, D. P. DePonte, V. Elser, S. W. Epp, B. Erk, H. Fleckenstein, L. Foucar, M. Frank, R. Fromme, H. Graafsma, I. Grotjohann, L. Gumprecht, J. Hajdu, C. Y. Hampton, A. Hartmann, R. Hartmann, S. Hau-Riege, G. Hauser, H. Hirsemann, P. Holl, J. M. Holton, A. Hömke, L. Johansson, N. Kimmel, S. Kassemeyer, F. Krasnqi, K.-U. Kühnel, M. Liang, L. Lomb, E. Malmerberg, S. Marchesini, A. V. Martin, F. R. N. C. Maia, M. Messerschmidt, K. Nass, C. Reich, R. Neutze, D. Rolles, B. Rudek, A. Rudenko, I. Schlichting, C. Schmidt, K. E. Schmidt, J. Schulz, M. M. Seibert, R. L. Shoeman, R. Sierra, H. Soltau, D. Starodub, F. Stellato, S. Stern, L. Strüder, N. Timneanu, J. Ullrich, X. Wang, G. J. Williams, G. Weidenspointner, U. Weierstall, C. Wunderer, A. Barty, J. C. H. Spence and H. N. Chapman, *Opt. Express*, 2012, **20**, 2706–2716.

67 V. Panneels, W. T. Wu, C. J. Tsai, P. Nogly, J. Rheinberger, K. Jaeger, G. Cicchetti, C. Gati, L. M. Kick, L. Sala, G. Capitani, C. Milne, C. Padeste, B. Pedrini, X. D. Li, J. Standfuss, R. Abela and G. Schertler, *Struct. Dyn.*, 2015, **2**, 8.

68 M. Schmidt, *Adv. Condens. Matter Phys.*, 2013, **10**, DOI: [10.1155/2013/167276](https://doi.org/10.1155/2013/167276).



69 G. D. Calvey, A. M. Katz and L. Pollack, *Anal. Chem.*, 2019, **91**, 7139–7144.

70 J. R. Stagno, Y. Liu, Y. R. Bhandari, C. E. Conrad, S. Panja, M. Swain, L. Fan, G. Nelson, C. Li, D. R. Wendel, T. A. White, J. D. Coe, M. O. Wiedorn, J. Knoska, D. Oberthuer, R. A. Tuckey, P. Yu, M. Dyba, S. G. Tarasov, U. Weierstall, T. D. Grant, C. D. Schwieters, J. Zhang, A. R. Ferre-D'Amare, P. Fromme, D. E. Draper, M. Liang, M. S. Hunter, S. Boutet, K. Tan, X. Zuo, X. Ji, A. Barty, N. A. Zatsepин, H. N. Chapman, J. C. H. Spence, S. A. Woodson and Y. X. Wang, *Nature*, 2017, **541**, 242–246.

71 J. L. Olmos, S. Pandey, J. M. Martin-Garcia, G. Calvey, A. Katz, J. Knoska, C. Kupitz, M. S. Hunter, M. Liang, D. Oberthuer, O. Yefanov, M. Wiedorn, M. Heyman, M. Holl, K. Pande, A. Barty, M. D. Miller, S. Stern, S. Roy-Chowdhury, J. Coe, N. Nagaratnam, J. Zook, J. Verburgt, T. Norwood, I. Poudyal, D. Xu, J. Koglin, M. H. Seaberg, Y. Zhao, S. Bajt, T. Grant, V. Mariani, G. Nelson, G. Subramanian, E. Bae, R. Fromme, R. Fung, P. Schwander, M. Frank, T. A. White, U. Weierstall, N. Zatsepин, J. Spence, P. Fromme, H. N. Chapman, L. Pollack, L. Tremblay, A. Ourmazd, G. N. Phillips and M. Schmidt, *BMC Biol.*, 2018, **16**, 59.

72 M. Dasgupta, D. Budday, S. H. P. de Oliveira, P. Madzelan, D. Marchany-Rivera, J. Seravalli, B. Hayes, R. G. Sierra, S. Boutet, M. S. Hunter, R. Alonso-Mori, A. Batyuk, J. Wierman, A. Lyubimov, A. S. Brewster, N. K. Sauter, G. A. Applegate, V. K. Tiwari, D. B. Berkowitz, M. C. Thompson, A. E. Cohen, J. S. Fraser, M. E. Wall, H. van den Bedem and M. A. Wilson, *Proc. Natl. Acad. Sci. U. S. A.*, 2019, **116**, 25634.

73 K. R. Beyerlein, D. Dierksmeyer, V. Mariani, M. Kuhn, I. Sarrou, A. Ottaviano, S. Awel, J. Knoska, S. Fuglerud, O. Jonsson, S. Stern, M. O. Wiedorn, O. Yefanov, L. Adriano, R. Bean, A. Burkhardt, P. Fischer, M. Heymann, D. A. Horke, K. E. J. Jungnickel, E. Kovaleva, O. Lorbeer, M. Metz, J. Meyer, A. Morgan, K. Pande, S. Panneerselvam, C. Seuring, A. Tolstikova, J. Lieske, S. Aplin, M. Roessle, T. A. White, H. N. Chapman, A. Meents and D. Oberthuer, *IUCrJ*, 2017, **4**, 769–777.

74 R. Dimpfer, H. Reichert, P. Raimondi, L. Sánchez Ortiz, F. Sette and J. Susini, *ESRF Upgrade Programme Phase II (2015–2022) - Technical Design Study (“The Orange Book”)*, The European Synchrotron Radiation Facility.

75 A. Meents, M. O. Wiedorn, V. Srajer, R. Henning, I. Sarrou, J. Bergtholdt, M. Barthelmess, P. Y. A. Reinke, D. Dierksmeyer, A. Tolstikova, S. Schaible, M. Messerschmidt, C. M. Ogata, D. J. Kissick, M. H. Taft, D. J. Manstein, J. Lieske, D. Oberthuer, R. F. Fischetti and H. N. Chapman, *Nat. Commun.*, 2017, **8**, 12.

76 P. Nogly, D. James, D. J. Wang, T. A. White, N. Zatsepин, A. Shilova, G. Nelson, H. G. Liu, L. Johansson, M. Heymann, K. Jaeger, M. Metz, C. Wickstrand, W. T. Wu, P. Bath, P. Berntsen, D. Oberthuer, V. Panneels, V. Cherezov, H. Chapman, G. Schertler, R. Neutze, J. Spence, I. Moraes, M. Burghammer, J. Standfuss and U. Weierstall, *IUCrJ*, 2015, **2**, 168–176.

77 O. Saldanha, M. E. Brennich, M. Burghammer, H. Herrmann and S. Köster, *Biomicrofluidics*, 2016, **10**, 024108.

78 S. E. Wolf, J. Leiterer, M. Kappl, F. Emmerling and W. Tremel, *J. Am. Chem. Soc.*, 2008, **130**, 12342–12347.

79 P. Sonderby, C. Soderberg, C. G. Frankaer, G. Peters, J. T. Bukrinski, A. Labrador, T. S. Plivelic and P. Harris, *J. Synchrotron Radiat.*, 2020, **27**, 396–404.

80 A. M. Seddon, S. J. Richardson, K. Rastogi, T. S. Plivelic, A. M. Squires and C. Pfrang, *J. Phys. Chem. Lett.*, 2016, **7**, 1341–1345.

81 A. Milsom, A. M. Squires, J. A. Boswell, N. J. Terrill, A. D. Ward and C. Pfrang, *Atmos. Chem. Phys.*, 2021, **21**, 15003–15021.

82 A. J. deMello, *Nature*, 2006, **442**, 394–402.

83 Y. Liu and X. Jiang, *Lab Chip*, 2017, **17**, 3960–3978.

84 A. B. Theberge, F. Courtois, Y. Schaerli, M. Fischlechner, C. Abell, F. Hollfelder and W. T. S. Huck, *Angew. Chem., Int. Ed.*, 2010, **49**, 5846–5868.

85 S. Köster and T. Pfohl, *Mod. Phys. Lett. B*, 2012, **26**, 1230018.

86 H. Song, J. D. Tice and R. F. Ismagilov, *Angew. Chem., Int. Ed.*, 2003, **42**, 768–772.

87 B. M. Zwickl, W. E. Shanks, A. M. Jayich, C. Yang, A. C. Bleszynski Jayich, J. D. Thompson and J. G. E. Harris, *Appl. Phys. Lett.*, 2008, **92**, 103125.

88 B. Weinhausen and S. Köster, *Lab Chip*, 2013, **13**, 212–215.

89 C. Gosse, S. Stanescu, J. Frederick, S. Lefrançois, A. Vecchiola, M. Moskura, S. Swaraj, R. Belkhou, B. Watts, P. Haltebourg, C. Blot, J. Daillant, P. Guenoun and C. Chevallard, *Lab Chip*, 2020, **20**, 3213–3229.

90 K. Dhouib, C. K. Malek, W. Pfleging, B. Gauthier-Manuel, R. Duffait, G. Thuillier, R. Ferrigno, L. Jacquemet, J. Ohana, J. L. Ferrer, A. Theobald-Dietrich, R. Giege, B. Lorber and C. Sauter, *Lab Chip*, 2009, **9**, 1412–1421.

91 M. E. Brennich, J. F. Nolting, C. Dammann, B. Noding, S. Bauch, H. Herrmann, T. Pfohl and S. Köster, *Lab Chip*, 2011, **11**, 708–716.

92 T. Lange, S. Charton, T. Bizien, F. Testard and F. Malloggi, *Lab Chip*, 2020, **20**, 2990–3000.

93 R. Barrett, M. Faucon, J. Lopez, G. Cristobal, F. Destremaut, A. Dodge, P. Guillot, P. Laval, C. Masselon and J. B. Salmon, *Lab Chip*, 2006, **6**, 494–499.

94 S. Sui, Y. X. Wang, K. W. Kolewe, V. Srajer, R. Henning, J. D. Schiffman, C. Dimitrakopoulos and S. L. Perry, *Lab Chip*, 2016, **16**, 3082–3096.

95 Z. Ren, M. Ayhan, S. Bandara, K. Bowatte, I. Kumarapperuma, S. Gunawardana, H. Shin, C. Wang, X. T. Zeng and X. J. Yang, *Lab Chip*, 2018, **18**, 2246–2256.

96 T. M. Squires and S. R. Quake, *Rev. Mod. Phys.*, 2005, **77**, 977–1026.

97 H. A. Stone, A. D. Stroock and A. Ajdari, *Annu. Rev. Fluid Mech.*, 2004, **36**, 381–411.

98 Z. Lu, J. McMahon, H. Mohamed, D. Barnard, T. R. Shaikh, C. A. Mannella, T. Wagenknecht and T.-M. Lu, *Sens. Actuators, B*, 2010, **144**, 301–309.



99 A. D. Stroock, S. K. W. Dertinger, A. Ajdari, I. Mezić, H. A. Stone and G. M. Whitesides, *Science*, 2002, **295**, 647–651.

100 X. Casadevall i Solvas and A. deMello, *Chem. Commun.*, 2011, **47**, 1936–1942.

101 O. Saldanha, R. Graceffa, C. Hemonnot, C. Ranke, G. Brehm, M. Liebi, B. Marmiroli, B. Weinhausen, M. Burghammer and S. Köster, *ChemPhysChem*, 2017, **18**, 1220.

102 M. A. Levenstein, Y.-Y. Kim, L. Hunter, C. Anduix-Canto, C. González Niño, S. J. Day, S. Li, W. J. Marchant, P. A. Lee, C. C. Tang, M. Burghammer, F. C. Meldrum and N. Kapur, *Lab Chip*, 2020, **20**, 2954–2964.

103 B. Wunderlich, D. Nettels and B. Schuler, *Lab Chip*, 2014, **14**, 219–228.

104 B. D. Cullity and S. R. Stock, *Elements of X-Ray Diffraction*, Prentice Hall, New Jersey, 3rd edn, 2001.

105 P. Lindner and T. Zemb, *Neutrons, X-rays and Light: Scattering Methods Applied to Soft Condensed Matter*, North Holland, 2002.

106 A. Merlin, J. Angly, L. Daubersies, C. Madeira, S. Schoder, J. Leng and J. B. Salmon, *Eur. Phys. J. E: Soft Matter Biol. Phys.*, 2011, **34**, 1–7.

107 L. C. McKenzie, P. M. Haben, S. D. Kevan and J. E. Hutchison, *J. Phys. Chem. C*, 2010, **114**, 22055–22063.

108 M. Takesue, T. Tomura, M. Yamada, K. Hata, S. Kuwamoto and T. Yonezawa, *J. Am. Chem. Soc.*, 2011, **133**, 14164–14167.

109 R. Stehle, G. Goerigk, D. Wallacher, M. Ballauff and S. Seiffert, *Lab Chip*, 2013, **13**, 1529–1537.

110 I. Rodríguez-Ruiz, S. Charton, D. Radajewski, T. Bizien and S. Teychené, *CrystEngComm*, 2018, **20**, 3302–3307.

111 A. Y. Fong, L. Pellouchoud, M. Davidson, R. C. Walroth, C. Church, E. Teareva, L. Wu, K. Peterson, B. Meredig and C. J. Tassone, *J. Chem. Phys.*, 2021, **154**, 224201.

112 K. Younes, M. Poli, P. Muhunthan, I. Rajkovic, S. Ermon, T. M. Weiss and M. Ihme, *Nucl. Instrum. Methods Phys. Res., Sect. A*, 2023, **1057**, 168719.

113 J. F. Moulin, S. V. Roth and P. Müller-Buschbaum, *Rev. Sci. Instrum.*, 2008, **79**, 015109.

114 E. Metwalli, J. F. Moulin, J. Perlich, W. Wang, A. Diethert, S. V. Roth and P. Müller-Buschbaum, *Langmuir*, 2009, **25**, 11815–11821.

115 J. Kehres, T. Pedersen, F. Masini, J. W. Andreasen, M. M. Nielsen, A. Diaz, J. H. Nielsen, O. Hansen and I. Chorkendorff, *J. Synchrotron Radiat.*, 2016, **23**, 455–463.

116 H. G. Alison, R. J. Davey, J. Garside, M. J. Quayle, G. J. T. Tiddy, D. T. Clarke and G. R. Jones, *Phys. Chem. Chem. Phys.*, 2003, **5**, 4998–5000.

117 T. Chen, A. Neville, K. Sorbie and Z. Zhong, *Faraday Discuss.*, 2007, **136**, 355–365.

118 T. Chen, A. Neville, K. Sorbie and Z. Zhong, *Chem. Eng. Sci.*, 2009, **64**, 912–918.

119 E. Mavredaki, A. Neville and K. Sorbie, *Appl. Surf. Sci.*, 2011, **257**, 4264–4271.

120 D. Burkle, R. De Motte, W. Taleb, A. Kleppe, T. Comyn, S. M. Vargas, A. Neville and R. Barker, *Rev. Sci. Instrum.*, 2016, **87**, 7.

121 T. Beuvier, E. A. C. Panduro, P. Kwasniewski, S. Marre, C. Lecoutre, Y. Garrabos, C. Aymonier, B. Calvignac and A. Gibaud, *Lab Chip*, 2015, **15**, 2002–2008.

122 M. A. Levenstein, C. Anduix-Canto, Y.-Y. Kim, M. A. Holden, C. González Niño, D. C. Green, S. E. Foster, A. N. Kulak, L. Govada, N. E. Chayen, S. J. Day, C. C. Tang, B. Weinhausen, M. Burghammer, N. Kapur and F. C. Meldrum, *Adv. Funct. Mater.*, 2019, **29**, 1808172.

123 M. A. Levenstein, L. E. Wayment, C. D. Scott, R. A. Lunt, P.-B. Flandrin, S. Day, C. Tang, C. C. Wilson, F. C. Meldrum, N. Kapur and K. Robertson, *Anal. Chem.*, 2020, **92**, 7754–7761.

124 D. Radajewski, L. Hunter, X. He, O. Nahi, J. M. Galloway and F. C. Meldrum, *Lab Chip*, 2021, **21**, 4498–4506.

125 P. J. E. M. van der Linden, A. M. Popov and D. Pontoni, *Lab Chip*, 2020, **20**, 4128–4140.

126 B. Fleury, M.-A. Neouze, J.-M. Guigner, N. Menguy, O. Spalla, T. Gacoin and D. Carriere, *ACS Nano*, 2014, **8**, 2602–2608.

127 M. O. Besenhard, A. P. LaGrow, A. Hodzic, M. Kriechbaum, L. Panariello, G. Bais, K. Loizou, S. Damilos, M. Margarida Cruz, N. T. K. Thanh and A. Gavrilidis, *Chem. Eng. J.*, 2020, **399**, 125740.

128 M. Durelle, F. Gobeaux, T. K. Truong, S. Charton and D. Carriere, *Cryst. Growth Des.*, 2023, **23**, 5631–5640.

129 M. W. Terban, D. Banerjee, S. Ghose, B. Medasani, A. Shukla, B. A. Legg, Y. Zhou, Z. Zhu, M. L. Sushko, J. J. De Yoreo, J. Liu, P. K. Thallapally and S. J. L. Billinge, *Nanoscale*, 2018, **10**, 4291–4300.

130 M. L. Beauvais, P. J. Chupas, D. O’Nolan, J. B. Parise and K. W. Chapman, *ACS Mater. Lett.*, 2021, **3**, 698–703.

131 M. L. Beauvais, B. A. Sanchez Monserrate, T. Feng, R. Chen, P. Liu, P. J. Chupas and K. W. Chapman, *J. Appl. Crystallogr.*, 2022, **55**, 258–264.

132 M. J. Young, N. M. Bedford, N. Jiang, D. Lin and L. Dai, *J. Synchrotron Radiat.*, 2017, **24**, 787–795.

133 G. Kwon, Y.-H. Cho, K.-B. Kim, J. D. Emery, I. S. Kim, X. Zhang, A. B. F. Martinson and D. M. Tiede, *J. Synchrotron Radiat.*, 2019, **26**, 1600–1611.

134 L. Pollack, M. W. Tate, N. C. Darnton, J. B. Knight, S. M. Gruner, W. A. Eaton and R. H. Austin, *Proc. Natl. Acad. Sci. U. S. A.*, 1999, **96**, 10115–10117.

135 L. Pollack, M. W. Tate, A. C. Finnefrock, C. Kalidas, S. Trotter, N. C. Darnton, L. Lurio, R. H. Austin, C. A. Batt, S. M. Gruner and S. G. J. Mochrie, *Phys. Rev. Lett.*, 2001, **86**, 4962–4965.

136 M. Jiang and R. D. Braatz, *CrystEngComm*, 2019, **21**, 3534–3551.

137 M. O. Besenhard, S. Pal, G. Gkogkos and A. Gavrilidis, *React. Chem. Eng.*, 2023, **8**, 955–977.

138 K. Robertson, P. B. Flandrin, A. R. Klapwijk and C. C. Wilson, *Cryst. Growth Des.*, 2016, **16**, 4759–4764.

139 V. Körstgens, M. Philipp, D. Magerl, M. A. Niedermeier, G. Santoro, S. V. Roth and P. Müller-Buschbaum, *RSC Adv.*, 2014, **4**, 1476–1479.

140 J. Han, F. Testard, F. Malloggi, C. Pierre-Eugene, N. Menguy and O. Spalla, *Langmuir*, 2012, **28**, 15966–15974.



141 R. K. Ramamoorthy, E. Yildirim, E. Barba, P. Roblin, J. A. Vargas, L.-M. Lacroix, I. Rodriguez-Ruiz, P. Decorse, V. Petkov, S. Teychené and G. Viau, *Nanoscale*, 2020, **12**, 16173–16188.

142 B. He, L. K. Macreadie, J. Gardiner, S. G. Telfer and M. R. Hill, *ACS Appl. Mater. Interfaces*, 2021, **13**, 54284–54293.

143 X. Chen, J. Wang, R. Pan, S. Roth and S. Förster, *J. Phys. Chem. C*, 2021, **125**, 1087–1095.

144 S. J. L. Billinge and M. G. Kanatzidis, *Chem. Commun.*, 2004, 749–760, DOI: [10.1039/b309577k](https://doi.org/10.1039/b309577k).

145 B. Winter, *Nucl. Instrum. Methods Phys. Res., Sect. A*, 2009, **601**, 139–150.

146 A. Iglesias-Juez, G. L. Chiarello, G. S. Patience and M. O. Guerrero-Pérez, *Can. J. Chem. Eng.*, 2022, **100**, 3–22.

147 O. Proux, E. Lahera, W. Del Net, I. Kieffer, M. Rovezzi, D. Testemale, M. Irar, S. Thomas, A. Aguilar-Tapia, E. F. Bazarkina, A. Prat, M. Tella, M. Auffan, J. Rose and J.-L. Hazemann, *J. Environ. Qual.*, 2017, **46**, 1146–1157.

148 M. A. Newton, A. J. Dent and J. Evans, *Chem. Soc. Rev.*, 2002, **31**, 83–95.

149 K. Amemiya, K. Sakata and M. Suzuki-Sakamaki, *Rev. Sci. Instrum.*, 2020, **91**, 093104.

150 B. Detlefs, S. Graziano and P. Glatzel, *Anal. Chem.*, 2023, **95**, 8758–8762.

151 M. C. Ringo, M. S. Huhta, G. Shea-McCarthy, J. E. Penner-Hahn and C. E. Evans, *Nucl. Instrum. Methods Phys. Res., Sect. B*, 1999, **149**, 177–181.

152 S. E. Mann, M. C. Ringo, G. Shea-McCarthy, J. Penner-Hahn and C. E. Evans, *Anal. Chem.*, 2000, **72**, 1754–1758.

153 M. M. Hoffmann, J. G. Darab, S. M. Heald, C. R. Yonker and J. L. Fulton, *Chem. Geol.*, 2000, **167**, 89–103.

154 M. M. Hoffmann, J. G. Darab and J. L. Fulton, *Rev. Sci. Instrum.*, 2001, **105**, 6876–6885.

155 G. Sankar, E. Cao and A. Gavriilidis, *Catal. Today*, 2007, **125**, 24–28.

156 E. M. Chan, M. A. Marcus, S. Fakra, M. ElNaggar, R. A. Mathies and A. P. Alivisatos, *J. Phys. Chem. A*, 2007, **111**, 12210–12215.

157 G. Hofmann, G. Tofighi, G. Rinke, S. Baier, A. Ewinger, A. Urban, A. Wenka, S. Heideker, A. Jahn, R. Dittmeyer and J. D. Grunwaldt, *J. Phys.: Conf. Ser.*, 2016, **712**, 012072.

158 G. Tofighi, H. Lichtenberg, J. Pesek, T. L. Sheppard, W. Wang, L. Schöttner, G. Rinke, R. Dittmeyer and J.-D. Grunwaldt, *React. Chem. Eng.*, 2017, **2**, 876–884.

159 P. Micheal Raj, L. Barbe, M. Andersson, M. De Albuquerque Moreira, D. Haase, J. Wootton, S. Nehzati, A. E. Terry, R. J. Friel, M. Tenje and K. G. V. Sigfridsson Clauss, *RSC Adv.*, 2021, **11**, 29859–29869.

160 S. Britto, C. M. A. Parlett, S. Bartlett, J. D. Elliott, K. Ignat'yev and S. L. M. Schroeder, *J. Phys. Chem. C*, 2023, **127**, 8631–8639.

161 S. Zinoveva, R. De Silva, R. D. Louis, P. Datta, C. S. S. R. Kumar, J. Goettert and J. Hormes, *Nucl. Instrum. Methods Phys. Res., Sect. A*, 2007, **582**, 239–241.

162 H. Oyanagi, Z. H. Sun, Y. Jiang, M. Uehara, H. Nakamura, K. Yamashita, L. Zhang, C. Lee, A. Fukano and H. Maeda, *J. Synchrotron Radiat.*, 2011, **18**, 272–279.

163 J. Monnier, L. Legrand, L. Bellot-Gurlet, E. Foy, S. Réguer, E. Rocca, P. Dillmann, D. Neff, F. Mirambet, S. Perrin and I. Guillot, *J. Nucl. Mater.*, 2008, **379**, 105–111.

164 J. Monnier, S. Réguer, E. Foy, D. Testemale, F. Mirambet, M. Saheb, P. Dillmann and I. Guillot, *Corros. Sci.*, 2014, **78**, 293–303.

165 K. S. Krishna, C. V. Navin, S. Biswas, V. Singh, K. Ham, G. L. Bovenkamp, C. S. Theegala, J. T. Miller, J. J. Spivey and C. S. S. R. Kumar, *J. Am. Chem. Soc.*, 2013, **135**, 5450–5456.

166 A. V. Dobrovolskaya, S. V. Chapek, O. A. Usoltsev, E. Naranov, D. N. Gorbunov, A. L. Trigub, A. L. Maximov, A. V. Soldatov and A. L. Bugaev, *J. Phys. Chem. C*, 2023, **127**, 20727–20733.

167 J. L. Fulton, Y. Chen, S. M. Heald and M. Balasubramanian, *Rev. Sci. Instrum.*, 2004, **75**, 5228–5231.

168 O. Fuchs, F. Maier, L. Weinhardt, M. Weigand, M. Blum, M. Zharnikov, J. Denlinger, M. Grunze, C. Heske and E. Umbach, *Nucl. Instrum. Methods Phys. Res., Sect. A*, 2008, **585**, 172–177.

169 M. Nagasaka, T. Hatsui, T. Horigome, Y. Hamamura and N. Kosugi, *J. Electron Spectrosc. Relat. Phenom.*, 2010, **177**, 130–134.

170 S. Schreck, G. Gavrila, C. Weniger and P. Wernet, *Rev. Sci. Instrum.*, 2011, **82**, 103101.

171 J. Probst, C. N. Borca, M. A. Newton, J. van Bokhoven, T. Huthwelker, S. Stavrakis and A. deMello, *ACS Meas. Sci. Au*, 2021, **1**, 27–34.

172 J. Brenker, K. Henzler, C. N. Borca, T. Huthwelker and T. Alan, *Lab Chip*, 2022, **22**, 1214–1230.

173 G. L. Chiarello, M. Nachtegaal, V. Marchionni, L. Quaroni and D. Ferri, *Rev. Sci. Instrum.*, 2014, **85**, 074102.

174 E. K. Dann, E. K. Gibson, C. R. A. Catlow, V. Celorrio, P. Collier, T. Eralp, M. Amboage, C. Hardacre, C. Stere, A. Kroner, A. Raj, S. Rogers, A. Goguet and P. P. Wells, *J. Catal.*, 2019, **373**, 201–208.

175 B. Venezia, E. Cao, S. K. Matam, C. Waldron, G. Cibin, E. K. Gibson, S. Golunski, P. P. Wells, I. Silverwood, C. R. A. Catlow, G. Sankar and A. Gavriilidis, *Catal. Sci. Technol.*, 2020, **10**, 7842–7856.

176 D. A. Huyke, A. Ramachandran, O. Ramirez-Neri, J. A. Guerrero-Cruz, L. B. Gee, A. Braun, D. Sokaras, B. Garcia-Estrada, E. I. Solomon, B. Hedman, M. U. Delgado-Jaime, D. P. DePonte, T. Kroll and J. G. Santiago, *J. Synchrotron Radiat.*, 2021, **28**, 1100–1113.

177 A. M. Karim, N. Al Hasan, S. Ivanov, S. Siefert, R. T. Kelly, N. G. Hallfors, A. Benavidez, L. Kovarik, A. Jenkins, R. E. Winans and A. K. Datye, *J. Phys. Chem. C*, 2015, **119**, 13257–13267.

178 T. Binninger, E. Fabbri, A. Patru, M. Garganourakis, J. Han, D. F. Abbott, O. Sereda, R. Kötz, A. Menzel, M. Nachtegaal and T. J. Schmidt, *J. Electrochem. Soc.*, 2016, **163**, H906.

179 R. K. Ramamoorthy, E. Yildirim, I. Rodriguez-Ruiz, P. Roblin, L.-M. Lacroix, A. Diaz, R. Parmar, S. Teychené and G. Viau, *Lab Chip*, 2024, **24**, 327–338.



180 S. Busch, T. H. Jensen, Y. Chushkin and A. Fluerasu, *Eur. Phys. J. E: Soft Matter Biol. Phys.*, 2008, **26**, 55–62.

181 A. Fluerasu, A. Moussaid, P. Falus, H. Gleyzolle and A. Madsen, *J. Synchrotron Radiat.*, 2008, **15**, 378–384.

182 A. Fluerasu, P. Kwasniewski, C. Caronna, F. Destremaut, J.-B. Salmon and A. Madsen, *New J. Phys.*, 2010, **12**, 035023.

183 R. Urbani, F. Westermeier, B. Banusch, M. Sprung and T. Pfohl, *J. Synchrotron Radiat.*, 2016, **23**, 1401–1408.

184 J. R. M. Lhermitte, M. C. Rogers, S. Manet and M. Sutton, *Rev. Sci. Instrum.*, 2017, **88**, 015112.

185 H.-G. Steinrück, C. J. Takacs, H.-K. Kim, D. G. Mackanic, B. Holladay, C. Cao, S. Narayanan, E. M. Dufresne, Y. Chushkin, B. Ruta, F. Zontone, J. Will, O. Borodin, S. K. Sinha, V. Srinivasan and M. F. Toney, *Energy Environ. Sci.*, 2020, **13**, 4312–4321.

186 P. Muhunthan, H. Li, G. Vignat, E. R. Toro, K. Younes, Y. Sun, D. Sokaras, T. Weiss, I. Rajkovic, T. Osaka, I. Inoue, S. Song, T. Sato, D. Zhu, J. L. Fulton and M. Ihme, *Rev. Sci. Instrum.*, 2024, **95**, 013901.

187 R. L. Leheny, *Curr. Opin. Colloid Interface Sci.*, 2012, **17**, 3–12.

188 O. Shpyrko, *J. Synchrotron Radiat.*, 2014, **21**, 1057–1064.

189 A. Sakdinawat and D. Attwood, *Nat. Photonics*, 2010, **4**, 840–848.

190 F. Pfeiffer, *Nat. Photonics*, 2018, **12**, 9–17.

191 M. Endrizzi, *Nucl. Instrum. Methods Phys. Res., Sect. A*, 2018, **878**, 88–98.

192 P. J. Withers, C. Bouman, S. Carmignato, V. Cnudde, D. Grimaldi, C. K. Hagen, E. Maire, M. Manley, A. Du Plessis and S. R. Stock, *Nat. Rev. Methods Primers*, 2021, **1**, 18.

193 U. Neuhausler, C. Jacobsen, D. Schulze, D. Stott and S. Abend, *J. Synchrotron Radiat.*, 2000, **7**, 110–112.

194 J. Rieger, J. Thieme and C. Schmidt, *Langmuir*, 2000, **16**, 8300–8305.

195 D. Guay, J. Stewart-Ornstein, X. Zhang and A. P. Hitchcock, *Anal. Chem.*, 2005, **77**, 3479–3487.

196 I. J. Drake, T. C. N. Liu, M. Gilles, T. Tyliszczak, A. L. D. Kilcoyne, D. K. Shuh, R. A. Mathies and A. T. Bell, *Rev. Sci. Instrum.*, 2004, **75**, 3242–3247.

197 T. Huthwelker, V. Zelenay, M. Birrer, A. Krepelova, J. Raabe, G. Tzvetkov, M. G. C. Vernooij and M. Ammann, *Rev. Sci. Instrum.*, 2010, **81**, 113706.

198 V. Zelenay, M. Ammann, A. Křepelová, M. Birrer, G. Tzvetkov, M. G. C. Vernooij, J. Raabe and T. Huthwelker, *J. Aerosol Sci.*, 2011, **42**, 38–51.

199 S. T. Kelly, P. Nigge, S. Prakash, A. Laskin, B. Wang, T. Tyliszczak, S. R. Leone and M. K. Gilles, *Rev. Sci. Instrum.*, 2013, **84**, 073708.

200 E. de Smit, I. Swart, J. F. Creemer, G. H. Hoveling, M. K. Gilles, T. Tyliszczak, P. J. Kooyman, H. W. Zandbergen, C. Morin, B. M. Weckhuysen and F. M. F. de Groot, *Nature*, 2008, **456**, 222–225.

201 E. de Smit, I. Swart, J. F. Creemer, C. Karunakaran, D. Bertwistle, H. W. Zandbergen, F. M. F. de Groot and B. M. Weckhuysen, *Angew. Chem., Int. Ed.*, 2009, **48**, 3632–3636.

202 M. Yoo, Y.-S. Yu, H. Ha, S. Lee, J.-S. Choi, S. Oh, E. Kang, H. Choi, H. An, K.-S. Lee, J. Y. Park, R. Celestre, M. A. Marcus, K. Nowrouzi, D. Taube, D. A. Shapiro, W. Jung, C. Kim and H. Y. Kim, *Energy Environ. Sci.*, 2020, **13**, 1231–1239.

203 Y. Sun and Y. Wang, *Nano Lett.*, 2011, **11**, 4386–4392.

204 J. Lim, Y. Li, D. H. Alsem, H. So, S. C. Lee, P. Bai, D. A. Cogswell, X. Liu, N. Jin, Y.-s. Yu, N. J. Salmon, D. A. Shapiro, M. Z. Bazant, T. Tyliszczak and W. C. Chueh, *Science*, 2016, **353**, 566–571.

205 T. Mefford, K. Karki, D. H. Alsem, D. Shapiro, N. Salmon and W. C. Chueh, *Microsc. Microanal.*, 2019, **25**, 2094–2095.

206 J. T. Mefford, A. R. Akbashev, M. Kang, C. L. Bentley, W. E. Gent, H. D. Deng, D. H. Alsem, Y.-S. Yu, N. J. Salmon, D. A. Shapiro, P. R. Unwin and W. C. Chueh, *Nature*, 2021, **593**, 67–73.

207 T. Ohigashi, M. Nagasaka, T. Horigome, N. Kosugi, S. M. Rosendahl and A. P. Hitchcock, *AIP Conf. Proc.*, 2016, **1741**, 050002.

208 V. Prabu, M. Obst, H. Hosseinkhannazer, M. Reynolds, S. Rosendahl, J. Wang and A. P. Hitchcock, *Rev. Sci. Instrum.*, 2018, **89**, 063702.

209 S.-J. Lee and G.-B. Kim, *J. Appl. Phys.*, 2003, **94**, 3620–3623.

210 W.-K. Lee, K. Fezzaa and T. Uemura, *J. Synchrotron Radiat.*, 2011, **18**, 302–304.

211 M. Prodanović, W. B. Lindquist and R. S. Seright, *J. Colloid Interface Sci.*, 2006, **298**, 282–297.

212 C. Noiri, B. Madé and P. Gouze, *Water Resour. Res.*, 2007, **43**, DOI: [10.1029/2006WR005379](https://doi.org/10.1029/2006WR005379).

213 S. Berg, H. Ott, S. A. Klapp, A. Schwing, R. Neiteler, N. Brussee, A. Makurat, L. Leu, F. Enzmann, J.-O. Schwarz, M. Kersten, S. Irvine and M. Stampanoni, *Proc. Natl. Acad. Sci. U. S. A.*, 2013, **110**, 3755–3759.

214 R. T. Armstrong, H. Ott, A. Georgiadis, M. Rücker, A. Schwing and S. Berg, *Water Resour. Res.*, 2014, **50**, 9162–9176.

215 S. Hasan, V. Niasar, N. K. Karadimitriou, J. R. A. Godinho, N. T. Vo, S. An, A. Rabbani and H. Steeb, *Proc. Natl. Acad. Sci. U. S. A.*, 2020, **117**, 23443–23449.

216 A. Piovesan, T. Van De Looverbosch, P. Verboven, C. Achille, C. Parra Cabrera, E. Boller, Y. Cheng, R. Ameloot and B. Nicolai, *Lab Chip*, 2020, **20**, 2403–2411.

217 K. J. Dobson, S. B. Coban, S. A. McDonald, J. N. Walsh, R. C. Atwood and P. J. Withers, *Solid Earth*, 2016, **7**, 1059–1073.

218 T. Bultreys, S. Ellman, C. M. Schlepütz, M. N. Boone, G. K. Pakkaner, S. Wang, M. Borji, S. Van Offenwert, N. Moazami Goudarzi, W. Goethals, C. W. Winardhi and V. Cnudde, *Proc. Natl. Acad. Sci. U. S. A.*, 2024, **121**, e2316723121.

219 J. Knoška, L. Adriano, S. Awel, K. R. Beyerlein, O. Yefanov, D. Oberthuer, G. E. Peña Murillo, N. Roth, I. Sarrou, P. Villanueva-Perez, M. O. Wiedorn, F. Wilde, S. Bajt, H. N. Chapman and M. Heymann, *Nat. Commun.*, 2020, **11**, 657.

220 C. Noiri, P. Gouze and B. Madé, *J. Hydrol.*, 2013, **486**, 211–223.



221 J. R. A. Godinho, K. M. Gerke, A. G. Stack and P. D. Lee, *Sci. Rep.*, 2016, **6**, 33086.

222 F. Fusseis, H. Steeb, X. Xiao, W.-l. Zhu, I. B. Butler, S. Elphick and U. Mader, *J. Synchrotron Radiat.*, 2014, **21**, 251–253.

223 S. Morais, C. Lecoutre, G. Philippot, G. Aubert, O. Nguyen, A. Cario, E. Vidal, Z. S. Campbell, Y. Garrabos, M. Azaroual, L. Helfen, D. Bernard and S. Marre, *Processes*, 2023, **11**, 1981.

224 J. R. A. Godinho, L. Ma, Y. Chai, M. Storm and T. L. Burnett, *Minerals*, 2019, **9**, 480.

225 C. Anduix-Canto, M. A. Levenstein, Y.-Y. Kim, J. R. A. Godinho, A. N. Kulak, C. G. Niño, P. J. Withers, J. P. Wright, N. Kapur, H. K. Christenson and F. C. Meldrum, *Adv. Funct. Mater.*, 2021, **31**, 2107312.

226 M. Nagasaka, H. Yuzawa, N. Takada, M. Aoyama, E. Rühl and N. Kosugi, *J. Chem. Phys.*, 2019, **151**, 114201.

227 I. Chaussavoine, A. Beauvois, T. Mateo, R. Vasireddi, N. Douri, J. Priam, Y. Liatimi, S. Lefrancois, H. Tabuteau, M. Davranche, D. Vantelon, T. Bizien, L. M. G. Chavas and B. Lassalle-Kaiser, *J. Synchrotron Radiat.*, 2020, **27**, 230–237.

228 M. A. Chen and B. D. Kocar, *J. Synchrotron Radiat.*, 2021, **28**, 461–471.

229 I. T. Neckel, L. F. de Castro, F. Callefo, V. C. Teixeira, A. L. Gobbi, M. H. Piazzetta, R. A. G. de Oliveira, R. S. Lima, R. A. Vicente, D. Galante and H. C. N. Tolentino, *Sci. Rep.*, 2021, **11**, 23671.

230 Y. Matsumoto, Y. Takeo, S. Egawa, G. Yamaguchi, S. Yokomae, M. Takei, H. Yumoto, T. Koyama, H. Ohashi, K. Tono, M. Yabashi, H. Mimura and T. Kimura, *Opt. Rev.*, 2022, **29**, 7–12.

231 K. K. Goncz, P. Batson, D. Ciarlo, B. W. Loo Jr and S. S. Rothman, *J. Microsc.*, 1992, **168**, 101–110.

232 J. Pine and J. R. Gilbert, Live Cell Specimens for X-Ray Microscopy, *X-Ray Microscopy III: Proceedings of the Third International Conference*, Berlin, Heidelberg, 1992.

233 F. M. F. de Groot, E. de Smit, M. M. van Schooneveld, L. R. Aramburo and B. M. Weckhuysen, *ChemPhysChem*, 2010, **11**, 951–962.

234 B. Bozzini, M. K. Abyaneh, M. Amati, A. Gianoncelli, L. Gregoratti, B. Kaulich and M. Kiskinova, *Chem. – Eur. J.*, 2012, **18**, 10196–10210.

235 J. F. Creemer, S. Helveg, G. H. Hoveling, S. Ullmann, A. M. Molenbroek, P. M. Sarro and H. W. Zandbergen, *Ultramicroscopy*, 2008, **108**, 993–998.

236 B. Bozzini, A. Gianoncelli, P. Bocchetta, S. Dal Zilio and G. Kourousias, *Anal. Chem.*, 2014, **86**, 664–670.

237 T. J. Heindel, *J. Fluids Eng.*, 2011, **133**, 074001.

238 A. Snigirev, I. Snigireva, V. Kohn, S. Kuznetsov and I. Schelokov, *Rev. Sci. Instrum.*, 1995, **66**, 5486–5492.

239 C. Noiriel, P. Gouze and D. Bernard, *Geophys. Res. Lett.*, 2004, **31**, L24603.

240 M. Di Michiel, J. M. Merino, D. Fernandez-Carreiras, T. Buslaps, V. Honkimäki, P. Falus, T. Martins and O. Svensson, *Rev. Sci. Instrum.*, 2005, **76**, 043702.

241 R. Mokso, F. Marone, D. Haberthür, J. C. Schittny, G. Mikuljan, A. Isenegger and M. Stampanoni, *AIP Conf. Proc.*, 2011, **1365**, 38–41.

242 A. Georgiadis, S. Berg, A. Makurat, G. Maitland and H. Ott, *Phys. Rev. E: Stat., Nonlinear, Soft Matter Phys.*, 2013, **88**, 033002.

243 S. Youssef, H. Deschamps, J. Dautriat, E. Rosenberg, R. Oughanem, E. Maire and R. Mokso, presented in part at the *International Symposium of the Society of Core Analysts, SCA2013-012*, Napa Valley, California, USA, 16–19 September, 2013.

244 S. Schlüter, S. Berg, M. Rücker, R. T. Armstrong, H. J. Vogel, R. Hilfer and D. Wildenschild, *Water Resour. Res.*, 2016, **52**, 2194–2205.

245 K. Singh, H. Menke, M. Andrew, Q. Lin, C. Rau, M. J. Blunt and B. Bijeljic, *Sci. Rep.*, 2017, **7**, 5192.

246 A. Jahanbakhsh, K. L. Włodarczyk, D. P. Hand, R. R. J. Maier and M. M. Maroto-Valer, *Sensors*, 2020, **20**, 4030.

247 A. Aliseda and T. J. Heindel, *Annu. Rev. Fluid Mech.*, 2021, **53**, 543–567.

248 L. Helfen, T. Baumbach, P. Mikulík, D. Kiel, P. Pernot, P. Cloetens and J. Baruchel, *Appl. Phys. Lett.*, 2005, **86**, 071915.

249 C. Noiriel and F. Renard, *C. R. Geosci.*, 2022, **354**, 255–280.

250 K. H. Cats and B. M. Weckhuysen, *ChemCatChem*, 2016, **8**, 1531–1542.

251 H. Gesswein, P. Stuble, D. Weber, J. R. Binder and R. Monig, *J. Appl. Crystallogr.*, 2022, **55**, 503–514.

252 J. Lyngso and J. S. Pedersen, *J. Appl. Crystallogr.*, 2021, **54**, 295–305.

253 P. Yuriy, V. Boris, J. Licai and K. Bonglea, Beam conditioning multilayer optics for laboratory x-ray sources, *Advances in Laboratory-based X-Ray Sources, Optics, and Applications IV*, 9590, San Diego, CA, 2015.

254 O. Taché, S. Rouziere, P. Joly, M. Amara, B. Fleury, A. Thill, P. Launois, O. Spalla and B. Abecassis, *J. Appl. Crystallogr.*, 2016, **49**, 1624–1631.

255 P. Le Magueres, M. DelCampo, K. Saito, J. D. Ferrara, J. Wojciechowski, A. Jones, D. Kucharczyk and M. Meyer, *Acta Crystallogr. Sect. A: Found. Adv.*, 2019, **75**, a163.

256 D. J. Batey, F. Van Assche, S. Vanheule, M. N. Boone, A. J. Parnell, O. O. Mykhaylyk, C. Rau and S. Cipiccia, *Phys. Rev. Lett.*, 2021, **126**, 193902.

257 J. Polte, R. Erler, A. F. Thunemann, S. Sokolov, T. T. Ahner, K. Rademann, F. Emmerling and R. Krahnert, *ACS Nano*, 2010, **4**, 1076–1082.

258 J. Polte, X. Tuaev, M. Wuithschick, A. Fischer, A. F. Thunemann, K. Rademann, R. Krahnert and F. Emmerling, *ACS Nano*, 2012, **6**, 5791–5802.

259 F. Kettemann, M. Wuithschick, G. Caputo, R. Krahnert, N. Pinna, K. Rademann and J. Polte, *CrystEngComm*, 2015, **17**, 1865–1870.

260 X. Chen, J. Schröder, S. Hauschild, S. Rosenfeldt, M. Dulle and S. Förster, *Langmuir*, 2015, **31**, 11678–11691.

261 M. Herbst, E. Hofmann and S. Förster, *Langmuir*, 2019, **35**, 11702–11709.



262 J. Tillier, T. Binninger, M. Garganourakis, A. Patru, E. Fabbri, T. J. Schmidt and O. Sereda, *J. Electrochem. Soc.*, 2016, **163**, H913.

263 S. Bucciarelli, S. R. Midtgård, M. Nors Pedersen, S. Skou, L. Arleth and B. Vestergaard, *J. Appl. Crystallogr.*, 2018, **51**, 1623–1632.

264 N. I. Anaraki, A. Sadeghpour, K. Iranshahi, C. Toncelli, U. Cendrowska, F. Stellacci, A. Dommann, P. Wick and A. Neels, *Nano Res.*, 2020, **13**, 2847–2856.

265 D. García-Lojo, E. Modin, S. Gómez-Graña, M. Impérator-Clerc, A. Chuvinilin, I. Pastoriza-Santos, J. Pérez-Juste, D. Constantin and C. Hamon, *Adv. Funct. Mater.*, 2021, **31**, 2101869.

266 T. Ehm, J. Philipp, M. Barkey, M. Ober, A. T. Brinkop, D. Simml, M. von Westphalen, B. Nickel, R. Beck and J. O. Radler, *J. Synchrotron Radiat.*, 2022, **29**, 1014–1019.

267 D. Radajewski, P. Roblin, P. Bacchin, M. Meireles and Y. Hallez, *Lab Chip*, 2023, **23**, 3280–3288.

268 J. D. Guild, S. T. Knox, S. B. Burholt, E. M. Hilton, N. J. Terrill, S. L. M. Schroeder and N. J. Warren, *Macromolecules*, 2023, **56**, 6426–6435.

269 T. D. Turner, C. O'Shaughnessy, X. He, M. A. Levenstein, L. Hunter, J. Wojciechowski, H. Bristowe, R. Stone, C. C. Wilson, A. Florence, K. Robertson, N. Kapur and F. C. Meldrum, *J. Appl. Crystallogr.*, 2024, **57**, 1299–1310.

270 E. G. Kozyr, P. N. Njoroge, S. V. Chapek, V. V. Shapovalov, A. A. Skorynina, A. Y. Pnevskaya, A. N. Bulgakov, A. V. Soldatov, F. Pellegrino, E. Groppo, S. Bordiga, L. Mino and A. L. Bugaev, *Catalysts*, 2023, **13**, 414.

271 T. C. Miller, M. R. Joseph, G. J. Havrilla, C. Lewis and V. Majidi, *Anal. Chem.*, 2003, **75**, 2048–2053.

272 A. A. Maurice, J. Theisen, V. Rai, F. Olivier, A. El Maangar, J. Duhamet, T. Zemb and J.-C. P. Gabriel, *Nano Sel.*, 2022, **3**, 425–436.

273 F. L. Olivier, S. M. Chevrier, B. Keller and J.-C. P. Gabriel, *Chem. Eng. J.*, 2023, **454**, 140306.

274 S. Youssef, D. Bauer, S. Békri, E. Rosenberg and O. Vizika, presented in part at the *International Symposium of the Society of Core Analysts, SCA2009-17*, Noordwijk aan Zee, The Netherlands, 27–30 September, 2009.

275 M. Andrew, B. Bijeljic and M. J. Blunt, *Geophys. Res. Lett.*, 2013, **40**, 3915–3918.

276 M. Andrew, B. Bijeljic and M. J. Blunt, *Int. J. Greenhouse Gas Control*, 2014, **22**, 1–14.

277 M. Andrew, B. Bijeljic and M. J. Blunt, *Adv. Water Resour.*, 2014, **68**, 24–31.

278 T. Bultreys, M. A. Boone, M. N. Boone, T. De Schryver, B. Masschaele, L. Van Hoorebeke and V. Cnudde, *Adv. Water Resour.*, 2016, **95**, 341–351.

279 H. P. Menke, B. Bijeljic, M. G. Andrew and M. J. Blunt, *Environ. Sci. Technol.*, 2015, **49**, 4407–4414.

280 P. Gajjar, J. S. Jørgensen, J. R. A. Godinho, C. G. Johnson, A. Ramsey and P. J. Withers, *Sci. Rep.*, 2018, **89**, 093702.

281 J. R. A. Godinho and P. J. Withers, *Geochim. Cosmochim. Acta*, 2018, **222**, 156–170.

282 K. Singh, A. T. M. S. Huqe Muzemder, D. Edey, M. Colbert, J. Maisano and B. Shafei, *Appl. Geochem.*, 2024, **167**, 105980.

283 S. A. Mäkiharju, J. Dewanckele, M. Boone, C. Wagner and A. Griesser, *Exp. Fluids*, 2021, **63**, 16.

284 T. Bultreys, S. Van Offenwert, W. Goethals, M. N. Boone, J. Aelterman and V. Cnudde, *Phys. Fluids*, 2022, **34**, 042008.

285 K. Tsuji, T. Emoto, Y. Nishida, E. Tamaki, Y. Kikutani, A. Hibara and T. Kitamori, *Anal. Sci.*, 2005, **21**, 799–803.

286 K. Nakano and K. Tsuji, *J. Anal. At. Spectrom.*, 2010, **25**, 562–569.

287 K. G. McIntosh, J. A. Neal, P. Nath and G. J. Havrilla, *X-Ray Spectrom.*, 2014, **43**, 332–337.

288 R. B. Hammond, X. Lai, K. J. Roberts, A. Thomas and G. White, *Cryst. Growth Des.*, 2004, **4**, 943–948.

289 S. Dharmayat, R. B. Hammond, X. Lai, C. Ma, E. Purba, K. J. Roberts, Z.-P. Chen, E. Martin, J. Morris and R. Bytheway, *Cryst. Growth Des.*, 2008, **8**, 2205–2216.

290 S. Fouilloux, A. Désert, O. Taché, O. Spalla, J. Daillant and A. Thill, *J. Colloid Interface Sci.*, 2010, **346**, 79–86.

291 J. Huang, F. Deng, B. Günther, K. Achterhold, Y. Liu, A. Jentys, J. A. Lercher, M. Dierolf and F. Pfeiffer, *J. Anal. At. Spectrom.*, 2021, **36**, 2649–2659.

292 P. Zimmermann, S. Peredkov, P. M. Abdala, S. DeBeer, M. Tromp, C. Müller and J. A. van Bokhoven, *Coord. Chem. Rev.*, 2020, **423**, 213466.

293 N. S. Genz, A.-J. Kallio, F. Meirer, S. Huotari and B. M. Weckhuysen, *Chem.: Methods*, 2024, **4**, e202300027.

294 V. C. Tidwell, L. C. Meigs, T. Christian-Frear and C. M. Boney, *J. Contam. Hydrol.*, 2000, **42**, 285–302.

295 A. Polak, A. S. Grader, R. Wallach and R. Nativ, *Water Resour. Res.*, 2003, **39**, 1106.

296 T. J. Heindel, J. N. Gray and T. C. Jensen, *Flow Meas. Instrum.*, 2008, **19**, 67–78.

297 A. Sheppard, S. Latham, J. Middleton, A. Kingston, G. Myers, T. Varslot, A. Fogden, T. Sawkins, R. Cruikshank, M. Saadatfar, N. Francois, C. Arns and T. Senden, *Nucl. Instrum. Methods Phys. Res., Sect. B*, 2014, **324**, 49–56.

298 M. Dierick, D. Van Loo, B. Masschaele, J. Van den Bulcke, J. Van Acker, V. Cnudde and L. Van Hoorebeke, *Nucl. Instrum. Methods Phys. Res., Sect. B*, 2014, **324**, 35–40.

299 G. R. Myers, A. M. Kingston, T. K. Varslot, M. L. Turner and A. P. Sheppard, *Appl. Opt.*, 2011, **50**, 3685–3690.

300 H. H. Shi, Y. Xiao, S. Ferguson, X. Huang, N. Wang and H. X. Hao, *Lab Chip*, 2017, **17**, 2167–2185.

301 M. L. Kovarik, P. C. Gach, D. M. Ornoff, Y. L. Wang, J. Balowski, L. Farrag and N. L. Allbritton, *Anal. Chem.*, 2012, **84**, 516–540.

302 R. Courson, S. Cargou, V. Conedera, M. Fouet, M. C. Blatche, C. L. Serpentini and A. M. Gue, *RSC Adv.*, 2014, **4**, 54847–54853.

303 S. Guha, S. L. Perry, A. S. Pawate and P. J. A. Kenis, *Sens. Actuators, B*, 2012, **174**, 1–9.

304 Y. Qin, J. E. Kreutz, T. Schneider, G. S. Yen, E. S. Shah, L. Wu and D. T. Chiu, *Lab Chip*, 2022, **22**, 4729–4734.



305 K. Sugioka, J. Xu, D. Wu, Y. Hanada, Z. Wang, Y. Cheng and K. Midorikawa, *Lab Chip*, 2014, **14**, 3447–3458.

306 A. Liga, J. A. S. Morton and M. Kersaudy-Kerhoas, *Microfluid. Nanofluid.*, 2016, **20**, 1–12.

307 R. Su, F. Wang and M. C. McAlpine, *Lab Chip*, 2023, **23**, 1279–1299.

308 N. J. Szymanski, B. Rendy, Y. Fei, R. E. Kumar, T. He, D. Milsted, M. J. McDermott, M. Gallant, E. D. Cubuk, A. Merchant, H. Kim, A. Jain, C. J. Bartel, K. Persson, Y. Zeng and G. Ceder, *Nature*, 2023, **624**, 86–91.

309 C. W. Coley, D. A. Thomas, J. A. M. Lummiss, J. N. Jaworski, C. P. Breen, V. Schultz, T. Hart, J. S. Fishman, L. Rogers, H. Gao, R. W. Hicklin, P. P. Plehiers, J. Byington, J. S. Piotti, W. H. Green, A. J. Hart, T. F. Jamison and K. F. Jensen, *Science*, 2019, **365**, eaax1566.